THE UNIVERSITY *of* EDINBURGH

UNSTEADY HYDRODYNAMICS OF TIDAL TURBINE BLADES

By

Gabriel Thomas Scarlett

THE UNIVERSITY
of EDINBURGH

A dissertation submitted to the University of Edinburgh in accordance with the requirements of the degree of Doctor of Philosophy in the School of Engineering.

August 2019

In memory of my beloved father
Peter John Scarlett
1946 - 1997

Lay summary

A growing global demand for electricity coupled with a divestment from fossil fuels are presenting new challenges for power generation. A promising renewable energy resource is that of the tides. A tidal stream turbine converts energy in the tidal current into electricity. A horizontal axis turbine does this by the rotation of two to three rotor blades which drive a generator. Devices are typically located in water depths of 20 m to 50 m.

The tidal energy sector is still in development. Presently devices have low reliability which contributes to the large cost of energy, making tidal energy uncompetitive with other energy sectors, such as wind energy. To improve reliability we need to better understand the unsteady loadings acting on a tidal turbine, which is the aim of this thesis.

A model for the unsteady hydrodynamics of the rotor has been developed to compute the loadings under different current and wave conditions. The code is readily available from the author's GitHub repository (www.github.com/gabscarlett). The model has led to the discovery that some of the common believes are incorrect (e.g. that the main source of unsteadiness are waves and not the shear), and that in some conditions the engineering tools that are commonly used (i.e. quasi-steady approach) can largely underestimate the loadings. Therefore, the knowledge and the tools that have been developed will contribute to the design of more reliable blades. Which will, in turn, reduce the cost of tidal energy, making the sector more commercially viable.

Abstract

Tidal turbines encounter a range of unsteady flow conditions, some of which may induce severe load fluctuations. A rotor blade can experience stall delay, load hysteresis and dynamic stall. This thesis addresses the need for the quantification of the unsteady flow around and loads on a full-sale tidal turbine rotor to improve fatigue analysis and enable the development of mitigating technologies.

A model for the unsteady hydrodynamics of the rotor has been developed which comprises of blade-element momentum, attached flow, separated flow and rotational augmentation implementations. The model can take as an input synthetic flow velocities or measured flow velocities. The code is readily available from the author's GitHub repository (www.github.com/gabscarlett).

A parameter study across a range of flow conditions is carried out by modelling the flow and predicting the root bending moment responses. The results show that waves and turbulence are the main sources of unsteadiness, and that extreme waves dominate over extreme turbulence. Severe yaw misalignment increases the load fluctuations but reduces the maximum peak. Large yaw angles, low tip-speed ratios, and very large waves lead to dynamic stall increasing the mean loads. Conversely, added mass effects mostly attenuate the load peaks.

An assessment of the rotor's performance during large, yet realistic wave conditions is carried out by considering field measurements of the onset flow. The load cycle is found to be governed by the waves, and the power and blade bending moments oscillate by half of their mean values. While the flow remains attached near the blade tip, dynamic stall occurs near the blade root, resulting in a twofold overshoot of the local lift coefficient compared to the static value. At the optimal tip-speed ratio, the difference between the unsteady loads computed with the proposed model and a simple quasi-

steady approximation is small. However, below the optimal tip-speed ratio, dynamic stall may occur over most of the blade, and the maximum peak loads can be twice those predicted with a quasi-steady approximation.

These results inform designers of the governing loads which are important for fatigue analysis. This will enhance the durability of tidal turbine blades without over-engineering them. In addition, the results reveal under which conditions simple, low-cost modelling approaches can be applied. These will, in turn, reduce the levelised cost of tidal energy, making the sector more commercially viable.

Declaration

I declare that this thesis was composed by myself, that the work contained herein is my own except where explicitly stated otherwise in the text, and that this work has not been submitted for any other degree or professional qualification except as specified.

Gabriel Thomas Scarlett
August 2019

Acknowledgements

Firstly, I must acknowledge my supervisors; Dr Ignazio Maria Viola and Professor Ton van den Bremer. To Ignazio, I am forever grateful for providing me with the opportunity to take up this Ph.D. His unorthodox style facilitated my curiosity whilst steering me towards an end goal. I could not have asked for a better supervisor. I am extremely grateful to have had the opportunity to work with Ton who provided excellent mentorship, instilled rigour in my analytical work and enhanced both my prose and grammar.

I express my sincere gratitude to my examiners; Professor David Ingram and Dr Tim Stallard. They administered a thorough and balanced review of my work and provided recommendations and corrections, which have enhanced this thesis.

I would like to extend my gratitude to Dr Brian Sellar who helped me navigate and understand the ReDAPT database, without which Chapter 9 would not have been possible. I wish to also thank, Dr Sam Draycott for providing model validation data and for his insightful correspondence. I am also very grateful to Simon Robertson for taking the time to proofread sections of my thesis.

This research was funded by the UK's Engineering and Physical Sciences Research Council, to whom I am very much obliged.

I truly appreciate all my family for the love, support and encouragement they provided me with over the years. Thanks to my mum for babysitting and to my sons for providing happiness on tap.

Last but certainly not least, a huge thank you to my wife Keiko whom I could not have done this without. Words cannot express how much her support has meant throughout this research and I appreciate the sacrifices she has had to make during this Ph.D.

Contents

Nomenclature

Latin Symbols

A	Rotor swept area (m^2)
A_R	Aspect ratio (-)
a	Axial induction factor (-)
a'	Tangential induction factor (-)
a_0	Wave amplitude (m)
a_γ	Axial induction factor for a yawed rotor (-)
a_c	Coordinate along normalised half chord (-)
b	half chord length (m)
$C'(k, W)$	Loewy's transfer deficit function (-)
$C(k)$	Theodorsen's transfer deficit function (-)
C_C^u	Unsteady chordwise force coefficient (-)
C_C	Chord wise force coefficient (-)
C_D^u	Unsteady drag coefficient (-)
C_D^{ind}	Induced drag coefficient (-)
C_D^{st}	Static drag coefficient (-)

C_D^{vis}	Viscous drag coefficient (-)
C_D	Drag coefficient (-)
C_{D_0}	Zero lift drag coefficient (-)
C_D^{rot}	Rotational drag coefficient (-)
$C_{F_{Tan}}$	Tangential force coefficient (-)
C_{F_T}	Thrust force coefficient (-)
C_L^p	Lift coefficient in attached flow (-)
C_L	Lift coefficient (-)
C_{L_0}	Unsteady lift coefficient for two degrees of freedom (-)
C_L^u	Unsteady lift coefficient (-)
C_L^c	Circulatory lift coefficient (-)
C_L^{nc}	Non-circulatory lift coefficient (-)
C_L^{rot}	Rotational lift coefficient (-)
C_M	Pitching moment coefficient (-)
C_{M_x}	Edgewise bending moment coefficient (-)
$C_{M_{y(q.s)}}$	Quasi-steady root bending moment coefficient (-)
C_{M_y}	Root bending moment coefficient (-)
C_N^p	Normal force coefficient in attached flow (-)
C_N^u	Unsteady normal force coefficient (-)
C_N^v	Vortex normal force coefficient (-)
C_N	Normal force coefficient (-)
C_{N_1}	Critical normal force coefficient for leading edge separation (-)
C_{N_α}	Linear normal force (lift) curve (-)

$C_N^{'}$	Lagged normal force coefficient (-)
C_N^c	Circulatory normal force coefficient (-)
C_N^f	Unsteady trailing edge separation normal force coefficient (-)
C_N^{nc}	Non-circulatory normal force coefficient (-)
C_N^{rot}	Rotational normal force coefficient (-)
C_P	Power coefficient (-)
C_Q	Torque coefficient (-)
C_T	Thrust coefficient (-)
C_v	Vortex circulation build up coefficient (-)
c	Chord length (m)
D	Tower diameter (m)
D_α	Deficit function for lagged angle deficit (-)
D_{ff}	Deficit function for lagged separation point (-)
d	Water depth (m)
F	Frequency (Hz)
F_r	Rotational frequency (Hz)
F_D	Drag force per unit length (Nm^{-1})
F_L	Lift force per unit length (Nm^{-1})
F_T	Thrust force per unit length (Nm^{-1})
F_{Tan}	Tangential force per unit length (Nm^{-1})
f	Trailing edge separation point (-)
f'	Lagged trailing edge separation point (-)
f''	Lagged trailing edge separation point (-)

f^{rot}	Trailing edge separation point corrected for rotation (-)
f_a	Apparent wave frequency (Hz)
f_t	Turbulent frequency component (Hz)
g	Gravitational acceleration (ms^{-2})
H	Wave height (m)
H_s	Significant wave height (m)
$\ddot{h}$	Heave acceleration of blade (ms^{-2})
$\dot{h}$	Heave velocity of blade (ms^{-1})
h_w	Wake spacing parameter (-)
I	Total turbulent intensity (-)
I_i	Turbulent intensity $[i = x, y, z]$ (-)
K	Wave number (m^{-1})
k	Reduced frequency (-)
L	Total aerodynamic loss factor (-)
L_2	L_2-norm least squares error (-)
L_H	Hub loss factor (-)
L_i	Turbulent length scale $[i = x, y, z]$ (m)
L_T	Tip loss factor (-)
M	Mach number (-)
M_x	Edgewise bending moment (Nm)
M_y	Root bending moment (Nm)
m	frequency ratio (-)
N	number of turbulent frequency constituents (-)

N_b	number of blades (-)
P	Power (W)
Q	Torque (Nm)
R	Blade tip radius (m)
$R(\hat{t})$	Correlation coefficient (-)
$R(\phi)$	Blade-element momentum residual equation (-)
R_t	Turbulent anisotropy ratio(-)
R_h	Blade hub radius (m)
$\dot{r}$	Reduced pitch rate (-)
r	Blade radial coordinate (m)
S	Power spectral density (m^2s^{-1})
S_i	Turbulent velocity spectrum, $[i = x, y, z]$ (m^2s^{-1})
St	Strouhal number (-)
s	Reduced time (incompressible) (-)
s'	Reduced time (compressible) (-)
T	Thrust force acting on actuator disc (N)
T_a	Apparent wave period (s)
T_f	Trailing edge separation time lag constant (-)
T_p	Leading edge pressure time lag constant (-)
T_r	Period of revolution (s)
T_v	Vortex time lag constant (-)
T_z	Zero-crossing wave period (s)
T_α	Angle time lag constant (-)

T_{St}	Effective Strouhal number (-)
T_{vL}	Vortex transit time (-)
$\hat{t}$	Time lag (turbulence) (s)
t	Time (s)
t_γ	Time lag (yaw) (s)
U_0	Reference velocity at hub height (ms^{-1})
U_ψ	Accumulated tangential velocity (ms^{-1})
U_i	Current velocity $[i = x, y, z]$ (ms^{-1})
$\bar{U}_i$	Mean velocity component $[i = x, y, z]$ (ms^{-1})
U_r	Relative inflow velocity (ms^{-1})
U_X	Accumulated axial velocity (ms^{-1})
U_∞	Freestream reference velocity (ms^{-1})
u_i'	Fluctuating velocity component $[i = x, y, z]$ (ms^{-1})
u_0	Axial induced velocity component (ms^{-1})
u_1	Azimuthally varying axial induced velocity component (ms^{-1})
V_x	Velocity in x corrected for tower shadow (ms^{-1})
V_y	Velocity in y induced by tower shadow (ms^{-1})
v_i	Average wake convection velocity (ms^{-1})
v_x	Vortex shape function (-)
W	Loewy's function (-)
W_k	Wave induced velocity $[k = x, z]$ (ms^{-1})
x	Horizontal Cartesian coordinate (m)
$\hat{x}$	Non-dimensional x-coordinate from tower (-)

x_c	Coordinate along chord (m)
y	Horizontal Cartesian coordinate (m)
z	Vertical Cartesian coordinate (m)
z_0	Depth of rotor hub (m)

Greek Symbols

α	Angle of attack (rad)
α'	Lagged angle of attack (rad)
α^{rot}	Rotational angle of attack (rad)
α_{ds0}^{rot}	Critical dynamic stall onset angle (rad)
α_{ss}^{rot}	Angle of static stall (rad)
α_{cr}	Critical angle (rad)
α_{ds0}	Critical dynamic stall onset angle (rad)
α_{ds}	Angle of dynamic stall onset (rad)
α_{ss}	Angle of static stall (rad)
$\bar{\alpha}$	Mean angle of attack (rad)
$\ddot{\alpha}$	Pitch acceleration of blade (rads^{-2})
$\dot{\alpha}$	Pitch rate (rads^{-1})
α_0	Zero lift angle (rad)
α_E	Equivalent angle of attack (rad)
β	Pitch angle (rad)
β_g	Geometrical pitch angle (rad)
β_p	Operational pitch angle (rad)

χ	Wake skew angle (rad)
$\Delta\alpha$	Pitch amplitude (rad)
δa	Axial induction factor iteration error (-)
δs	Non-dimensional time increment (-)
δt	Time increment (s)
$\delta\alpha^{rot}$	Rotational angle shift (rad)
$\delta\alpha_1$	Shift delay from static stall angle (rad)
η	Free surface elevation (m)
γ	Yaw angle (rad)
λ	Tip speed ratio (-)
λ'_r	Local instantaneous tip-speed ratio (-)
λ_r	Local tip-speed ratio (-)
μ	Normalised blade coordinate (-)
ν	Shear exponent (-)
Ω	Rotor rotational speed (rads^{-1})
ω	Forcing frequency (rads^{-1})
ω_a	Apparent wave frequency (rads^{-1})
$\Phi(s)$	Wagner function (-)
Φ_j	Phase angle of j^{th} turbulent frequency (rad)
ϕ	Flow angle (rad)
Ψ	Stream function (m^2s)
ψ	Azimuthal position of blade (rad)
ρ	Density of working fluid (kgm^{-3})

σ	Dummy non-dimensional time variable (-)
σ_i	Standard deviation of flow velocity component $[i = x, y, z]$ (-)
σ_r	Local solidity (-)
$\sigma_{C_{M_y}}$	Standard deviation of root bending moment coefficient (-)
τ	Vortex transit time scale (-)
τ_i	Integral time scale of flow velocity component $[i = x, y, z]$ (s)
θ	Oblique wave angle (rad)
θ_b	Phase angle of blade (rad)
ζ	Chordwise force recovery factor (-)

Acronyms

BEM	Blade element momentum
BL	Beddoes-Leishman
D-ADP	Divergent beam Acoustic Doppler Profiler
EMEC	European Marine Energy Centre
LCOE	Levelised cost of energy
LEV	Leading edge vortex
NACA	National Advisory Committee for Aeronautics
NREL	National Renewable Energy Laboratories
OSU	Ohio State University
ReDAPT	Reliable Data Acquisition Platform for Tidal
SB-ADP	Single-beam Acoustic Doppler Profiler
SWL	Still water level

List of Figures

List of Tables

Chapter 1

Introduction

"There is a tide in the affairs of men,
Which taken at the flood, leads on
to fortune."

— William Shakespeare

1.1 Tidal stream power

The growing global demand for electricity coupled with a divestment from fossil fuels are presenting new challenges for power generation. A promising renewable energy resource is that of the tides. The gravitational pull of the moon, sun and other celestial bodies on the Earth causes the oceans to bulge twice daily giving rise to tidal flows. In the open ocean these flows are not fast enough to harness, however, near coastal basins such as channels, inlets, headlands and islands the flow interacts with the land to produce flow velocities in excess of 7 ms^{-1} (Draper et al., 2010). Such sites are well suited for the deployment of tidal stream energy devices which convert the kinetic energy of the tide into electrical energy. Unlike the wind, the mean flow of tides is well known, making the amount of extractable energy very predictable. One of the most promising sites in the UK is the Pentland Firth, which, according to one assessment has an estimated maximum power output of 1.9 GW (Adcock et al., 2013). Studies commissioned by The Carbon Trust estimate that the UK has an extractable energy resource of 18 TWh per year (Black and Veatch, 2005a,b), which is 5% of the total energy demand. Harnessing this resource would make tidal stream energy a key player in the UK electricity market.

A variety of tidal stream devices exist; horizontal axis turbines, vertical axis turbines, oscillating foils, to name but a few. To date the horizontal axis turbine is the leading technology, primarily because it has already been proven for the wind industry. A horizontal axis tidal turbine generates power by the rotation of two to three lift driven blades which drive a generator. Devices are typically located in water depths between 20 m and 50 m and are either bottom mounted, pile mounted or floating. The increased density of water compared to air means that for similarly rated devices a tidal turbine typically has a rotor diameter four times smaller than that of a wind turbine. The higher distributed forces acting on tidal turbine blades means that they have thicker sections than wind turbine blades, making them very stiff. In addition, wind turbines may operate at compressible speeds, whereas tidal turbines operate well below this threshold due to the threat of cavitation, where the high rotational velocity of the blade elicits a local pressure causing vapour bubbles to implode against the blade, damaging the surface. Another difference is the free surface, this is beneficial in that the theoretical maximum extractable power for a wind turbine, known as the Betz limit can be exceeded due to the free surface restricting the flow. However, gravity waves generated at the free surface present a real challenge to blade designers.

A number of sea tests have been carried out in recent years, and the technology is approaching pre-commercial readiness. Six full scale tests have been completed at the European Marine Energy Centre (EMEC) at the Fall of Warness in Orkney, as well as several others elsewhere (Neill et al., 2017). To date, the Crown Estate have issued 17 leases for tidal current energy extraction in Scottish waters, 9 of which are in the Pentland Firth (Neill et al., 2017). The MeyGen project which is currently the world's largest array has now been installed by SIMEC Atlantis Energy in the Pentland Firth (Meygen LTD, 2012). Currently the array is about 6 MW with a plan to increase up to 86 MW by 2021 and then up to 400 MW in the second phase.

1.2 Challenges

Marine renewables have a very high capital expenditure compared with wind energy and thermal power generation, which is estimated to be between 60 - 80% of the final energy cost (Ocean Energy Forum, 2016). Therefore, the industry heavily relies on investment, loans and grants. As an example, the first phase of MeyGen required over £50 million, of which 34% was taken as debt and 26% from grants (Ocean Energy

Forum, 2016). The next stage of the project which will take the installed capacity up to 86 MW is estimated to cost £420 million (Meygen LTD, 2012). Thus the future of this and similar project relies heavily on revenue support through mechanisms such as CFD (contracts for difference) and FITs (feed-in tariffs).

Questions remain regarding the performance and long-term survivability of a horizontal axis tidal turbine rotor operating in a harsh marine environment (Chen and Lam, 2015). To be commercially viable devices must endure up to 25 years in the water with infrequent overhaul or repair. An area identified as high priority for technical progress by the Ocean Energy Forum (2016), is an increase in both reliability and survivability to protect investment and reduce costs.

The marine environment is inherently unsteady due to waves and turbulence. The rotation of the rotor blades through the shear layer of the tidal current and the unsteady flow causes a time-dependent flow field which can lead to unsteady flow phenomena such as load hysteresis, stall delay and dynamic stall. Stall delay is a process whereby the angle of attack increases sufficiently rapidly so that separation is prevented beyond the static stall angle, which causes lift increases above the maximum static value. Dynamic stall is when unsteady separation and stall occurs, resulting in a hysteresis loop of the lift with the angle of attack. If the angle of attack becomes large enough, dynamic stall may induce vortex shedding from the leading-edge of the blade. The convection of the leading-edge vortex over the blade surface can produce load overshoots of 100% or more above the quasi-steady value (McCroskey, 1995). These effects compounded with rotational forces and velocities induced by the dynamic wake behind the rotor make for a highly unsteady operational environment.

A probability analysis from 2012 investigated the survivability of four horizontal axis tidal turbines with powers ratings between 1 MW and 1.2 MW, and for a range of different fixings (Delorm et al., 2012). Using data from similarly rated wind turbines, the study estimated the reliability of tidal turbine blades would result in one failure every two years per turbine. Technology developers continue to improve devices. However, it is difficult to know the current state of the technology since failure rate data for full-scale devices is commercially sensitive. Certification standards for tidal turbine blades state that the nominal probability of failure per year should be under 10^{-4} (DNV-GL, 2015). A lack of quantifiable data relating to fatigue and extreme loading could lead to over conservative designs being produced in order to meet these standards, which will impact the levelised cost of energy (LCOE) and the roll-out-rate of technology.

1.3 Experimental work on the unsteady hydrodynamics of tidal turbines

In this section previous experimental work on the unsteady hydrodynamics of tidal turbines are reviewed.

It is necessary to first introduce the non-dimensional parameter used to determine the extent of the unsteadiness in the flow: the reduced frequency (k), which is defined as

$$k = \frac{\omega c}{2U_r}, \tag{1.1}$$

where U_r and ω are the relative velocity and the angular frequency of the unsteady fluctuations, respectively. In general the flow is said to be unsteady for $k > 0.05$ and highly unsteady for $k > 0.2$ (Leishman, 2006).

1.3.1 Towing tank experiments

Towing tank experiments move the turbine on a carriage rather than generating a flow. This produces oscillations in the rotor plane that are uniform with depth, which is an idealised method of representing waves and turbulence.

Whelan et al. (2009) carried out experiments on a scaled turbine in a towing tank. The turbine with a rotor diameter of 0.3 m was towed at a uniform speed whilst oscillating the external carriage on which it was mounted. In an attempt to quantify the circulatory and added mass contributions to the forces, the authors compared measured thrust data with the Morison equation, which conveniently separates the added mass and drag forces (Morison et al., 1950). This study was performed for a range of individual sinusoidal flow fluctuations. The tested reduced frequency for each were relatively low (ca. 0.02). The study showed for the first time that the complex, 3D geometry of a tidal turbine, for a low reduced frequency, has a positive and small inertia term. However, the Morison equation does not account for the phase shift of the circulatory term due to the wake, and hence the added mass is always contributing to increase the load fluctuation. Conversely, for low reduced frequencies, the added mass could balance the wake effect, leading to a lower load fluctuation.

The relative contribution between the true added mass and the inertia term due to the wake was investigated by Milne et al. (2013a). They too carried out towing tank experiments using a range of oscillating frequencies set to replicate the type of

unsteadiness caused by waves and large scale turbulence. Root bending moment measurements were compared with Theodorsen's theory (Theodorsen, 1935) which separates the circulatory and non-circulatory lift response. The authors anticipated that the wake contribution of the circulatory term is greater than the added mass. This is typical of when the reduced frequency is low, such as those tested here (ca. 0.05). They found this for a range of individual sinusoidal flow fluctuations. It remains to be determined how realistic these sinusoidal flow fluctuations are for a commercial scale turbine.

In a later study Milne et al. (2015) found that in attached flow the root bending moment fluctuations increased with frequency, which could exceed the steady value by 15%. A significant increase of the fluctuation with the reduced frequency is typically due to added mass, unless dynamic stall occurs. This result seems to suggest a significant added mass effect at high frequency. Again, it remains unclear which is the representative frequency experienced by the rotor. Moreover, this study revealed that the effect of multiple frequencies could be predicted from the superposition of single frequencies. Then in a further study, Milne et al. (2016) reported that at lower tip-speed ratios, the flow would be separated over most of the blade span, which for high frequency forcing caused the root bending moment to exceed the quasi-steady value by up to 25%. Hysteresis was found in the root bending moment time history with instantaneous tip-speed ratio, in which the authors were able to qualitatively highlight the key stages of dynamic stall. This indicates that severe unsteady conditions may lead to dynamic stall occurring over much of the blade eliciting overshoots in the global loadings (e.g. the root bending moment).

This work revealed that not only are we uncertain of the governing frequency experienced by the rotor, and of the effect of multiple frequencies, but that the turbine operates on the verge of a flow condition where dynamic stall effects become very significant. Hence we need to understand when and where on the blade this occurs. This is challenging and requires advanced models, as shown by the preliminary attempt of Milne (2014) where these experimental results were compared with theory using a Beddoes-Leishman dynamic stall model. The model included a modification for wind turbine blade load analysis by (Pierce and Hansen, 1995), however, the attached flow component was omitted, which as discussed in section 4.4, is an integral part of the model. A key parameter of the model is the angle of attack on the blade, which could only be approximated from the experimental data. Qualitative agreement was achieved for the lowest frequency case (0.50 Hz), however, the results diverge for higher fre-

quencies cases. It is postulated that this is due to an underestimate in the point of reattachment which leads to an overestimate in the loads. An attempt is made to correct the model by reducing the steady lift coefficient by 10%, however, the delay in reattachment is still under predicted.

1.3.2 Wave-towing tank experiments

In wave-towing tanks current in generated by towing the turbine rotor whilst waves paddles produce scaled representations of real waves reported in the ocean which vary in both space and time.

Barltrop et al. (2007) investigated loading due to waves in a towing tank on a rotor of 0.35 m. The rotor scaling is not reported, however, the wave frequencies are roughly 1/10 full-scale. The authors found that long waves, with a representative full-scale period of 10.7 s and reduced frequency of ca. 0.05, induced fluctuations in the root and edgewise bending moments of 50% and 100% above the mean value, respectively. Results were compared using linear-wave theory and a steady blade-element momentum model. The model predicted the loading due to long waves well, however, for steeper high frequency waves the model under predicted the experimental results. These results indicate that at high frequencies the unsteady effects are significant, however, it is uncertain what these are due to.

Galloway et al. (2014) tested the effects of a yaw misalignment and waves using a wave tank to generate linear waves incident to a 1/20 scale rotor. The experimental results showed that the median value of the root and edgewise bending moments was exceeded by up to 175% and 100%, respectively, during the presence of waves with a representative full-scale height of 2 m and period of 12.8 s, corresponding to a reduced frequency of ca. 0.03. The authors noted that the wave period had more of an effect on the fluctuations than wave height. Yaw misalignment angles ranging from 7.5° to 22.5° were investigated. The resulting load fluctuations were found to be negligible compared to those induced by waves. The experimental results were compared using an in-house blade-element momentum code, which included a dynamic inflow correction and the Boeing-Vertol dynamic stall model. The authors selected this dynamic stall model due to its simplicity, however, it does not contain attached flow and vortex shedding implementations. Comparison between the results and the model were mixed with better prediction achieved for cases without the presence of a yaw misalignment. The authors conclude that without the dynamic inflow model the load amplitudes were

underpredicted and that the effect of dynamic stall was limited and, therefore, can be neglected in some cases, despite not making comparison with quasi-steady values. These results are not in agreement with Milne et al. (2016).

1.3.3 Flume tank experiments on turbulent load fluctuations

Maganga et al. (2009) carried out experiments on a 1/30 scale model in a flume tank. They adjusted the turbulent intensity of the flow using honeycomb flow straighteners. Their results indicate that for a mean flow velocity of 0.8 ms^{-1}, that increasing the freestream turbulent intensity from 8% to 25% causes a reduction in the mean thrust and power. The decrease is moderate at low tip-speed ratios, however, exceeded 9% for tip-speed ratios above 9. The study does not report whether the turbulence is isotropic or the length scales present. Chamorro et al. (2015) investigated how coherent turbulent structures effect the power of a rotor of 0.50 m. Cylinders of varying size were placed upstream of the rotor, which were shown to alter the structure of the streamwise velocity spectra in the low frequency range. Their results found that for larger cylinders the turbine power was modified in the same frequency range, whereas, for decreasing cylinder size the turbine power spectra was largely unchanged. This result indicates that the power of a turbine is sensitive to turbulent length scale. Blackmore et al. (2016) developed a method of using static grids to generate turbulence in a flume of varying turbulent intensity and length scale. They used the set up to investigate the effects of turbulence on the performance of a 1/20 scale turbine. For an increase in turbulence intensity from 7% to 14% they observed a 10% decrease in the mean power and thrust, which concurs with Maganga et al. (2009). Conversely, the authors found that increasing length scale led to an increase in both the mean power and thrust, which concurs with Chamorro et al. (2015). With regard to blade root bending moments, they observed that increasing both turbulent intensity and length scale led to significant fluctuations above the mean value, which could reach up to 45%.

1.3.4 Scaling limitations

The discussed experimental results have given excellent insight into the unsteady loading on tidal turbine blades, however, compared to full-scale models both the Reynolds number and the reduced frequency are small.

The experimental results discussed in this section Barltrop et al. (2007); Whelan

et al. (2009); Milne (2014); Galloway et al. (2014) did not exceeded a reduced frequency of 0.05. Sequeira and Miller (2015) characterised a range of marine unsteadiness for a full-scale tidal turbine and found that at the blade tip, mid-section and hub, the reduced frequency can attain values of 0.4, 0.6 and 1.4, respectively. This indicates that very different unsteady flow regimes occur at full scale compared to model scale. The results only provide global load quantities, such as bending moments, thrust, etc. and it remains to be understood how the unsteady effects change along the blade span as the angle of attack changes. For instance it may be that only in extreme cases does dynamic stall have a global effect on the loadings, such as when operating at a low tip-speed ratio, as reported by Milne et al. (2016). Likewise, it could be that dynamic stall is occurring, but is confined to areas near the blade root where the local forces have little contribution to the root bending moment, so go undetected.

1.4 Modelling the unsteady hydrodynamics of tidal turbine blades

Techniques to model the unsteady loads and incident flow to tidal turbine blades are introduced. Following this previous work using such methods are reviewed.

1.4.1 Onset flow modelling

The onset flow in a tidal channel can be modelled using one of three ways. The most computational expensive is to solve the Navier-Stokes (NS) equations for mass and momentum in 3D with an appropriate turbulence model. Turbulence modelling is achieved through Reynolds-averaged Navier-Stokes (RANS) simulations or Large-Eddy Simulations, where the latter is the most accurate, but also has the greatest computationally overhead. This limits the area and resolution of topography that can be modelled. Further to this the non-linear combination of waves with turbulence is out of reach for engineering purposes. RANS and LES modelling require an onset turbulence condition. This can be provided using a spectral method, such as the von Kármán spectra or the Synthetic Eddy Method (SEM), both of which are discussed further in section 2.3. The second approach to modelling the flow is to depth average the NS equations giving the shallow water equations. These depth averaged 2D equations are more computationally efficient than the 3D equations. They typically give an accurate measure of the

mean flow through the channel, but the turbulence dynamics are inaccurate. The final approach is to physically model individual flow constituents, e.g. waves and turbulence and combine them to form an effective flow velocity at the blade. For example using the von Kármán spectrum or SEM to create a turbulent velocity time series and then a potential flow wave model to create a separate wave induced velocity time series. Then linearly combining each, with the addition of the rotational speed of the rotor, yielding a relative flow velocity. This lower order technique enables many different flow combinations to be considered efficiently, however, it ignores the non-linear physics relating to flow interaction. This final technique is used in this work since it enables one to quickly analyse the unsteady loads to many different flow combinations over a long time period.

1.4.2 Computational fluid dynamics

Computational Fluid Dynamics (CFD) which was briefly introduced in the previous subsection with respect to modelling the onset flow. Here its potential to model the unsteady blade loads are discussed.

To compute the loads acting on the blade the pressures over the blades are integrated. If the flow is mostly attached to the blade a reasonable estimate is achieved using RANS. However, when dynamic stall occurs, and the flow cycles through separation and reattachment then the simulation requires LES to model the boundary layer. This is a formidable and computationally intensive task requiring billions of cells to discretise the flow. To the best of my knowledge, there exists only one such case where a 3D simulation capturing deep dynamic stall with LES is carried out (Visbal, 2011). This case analysed a wing oscillating in heave for a Reynolds number in the order of 10,000. Tidal turbines operate at Reynolds number three orders of magnitudes greater than this. The further addition of blade rotation and surface waves would make for a highly complex simulation.

Afgan et al. (2013) carried out CFD simulations with both LES and RANS, but without onset turbulence. Results were compared to towing tank experiments. The authors reported that for a wide range of tip-speed ratios that the mean thrust and power are largely unaffected by turbulence. However, these results were pertaining to the RANS simulation only. Mean values for thrust and power were not reported for the LES simulation. Simulations by Ahmed et al. (2017) present results from an LES model with onset inflow turbulence generated by SEM. They found that turbulent inflow with

larger length-scales produced higher power and in some cases thrust coefficients than an LES model without SEM onset flow. These results concur with the experimental observations of Chamorro et al. (2015) and Maganga et al. (2009).

1.4.3 Vortex methods

If the flow is assumed to be inviscid then vortex methods such as vortex lattice and vortex panel can be used to determine the loads. These methods use potential flow theory to model circulation by placing vortices along a line or sheet placed on the blade or in the wake. The induced velocity is then computed using the Biot-Savart law. Vortex methods can represent the wake of the turbine well and give good accuracy of the loads when assuming there is minimal separation. However, for large regions of separation potential flow models cannot capture trailing edge separation, stall delay and dynamic stall.

McCombes et al. (2011) developed a vortex lattice method using the vorticity transport equations to model the wake of a tidal turbine. They compared the method with data from the NREL Phase IV experiment. The model agreed well with the data when the flow was perpendicular to the rotor plane, however, for the yawed case, where the flow is skewed, the model could not capture the viscous effects which led to over predictions. Johnson et al. (2013) used a vortex method to quantify the circulatory effect for an impulsive turbine start-up in a fully developed flow. The authors found that the thrust force can be twice the steady state value, which compared well against experimental data. McNae (2013) developed an unsteady vortex lattice method to analyse the circulatory and non-circulatory forces acting on tidal rotors operating in unsteady flows. They showed that dynamic inflow can have a significant influence on the turbine thrust in unsteady flow conditions.

1.4.4 Industry standard engineering models

Two engineering tools exist for industry standard simulations of the loads; Tidal Bladed which is a commercial software and FAST which is open-source. These models are discussed herein.

Tidal Bladed is a multibody dynamics tool capable of modelling all the components of a tidal turbine (Bossanyi, 2012). The product is an offshoot from Bladed, a dedicated wind turbine analyses tool. There is a graphical interface, and visualisation tools

making it easy to use. Waves, turbulence, blade rotation through the shear layer and tower shadow can all be modelled. The turbulence model is based on the turbulence model used in Bladed for wind turbines. The aerodynamic loads are determined using blade element momentum (BEM) theory with the unsteady loads determined using a dynamic wake model and a dynamic stall model. The dynamic wake model determines the dynamic inflow velocity due to the unsteady wake behind the rotor. The dynamic stall model uses the original Beddoes-Leishman model which is for helicopter rotors. The use of this model in tidal bladed is justified by the early use of it to determine the unsteady loads on horizontal axis wind turbine blades by Galbraith et al. (1990). However, more recently the same author has contributed to research which found this model poorly reconstructs the unsteady load coefficients in low Mach number flows Sheng et al. (2008, 2010).

FAST is an open-source software developed by the National Renewable Energy Laboratory (NREL). The software is primarily used for wind turbines. The FAST code framework pulls together a number of subroutines; AeroDyn to model the aerodynamics, TurbSim to model turbulence and a number of other modules for; control, elasticity, etc. As with Tidal Bladed, AeroDyn contains BEM, dynamic wake and dynamic stall implementations (Moriarty and Hansen, 2005). The source code for the NREL software is available and can be manipulated. There is no option to model waves, instead the user must provide a wave velocity field as an input. Galloway et al. (2014) compared their experimental bending moment time histories from their scaled tidal turbine rotor with those predicted by FAST. They implemented changes to the velocity input files in order to model wave conditions, however, the prediction was poor with root bending moments over predicted by around 25% and edgewise bending moments under predicted by approximately 25%. They postulate that the FAST source code requires further modification to make it suitable for tidal turbine analysis. This highlights the problems using models specifically developed for the wind energy industry.

1.5 Research gap

Past results show that, in some realistic unsteady flow conditions, the flow around a tidal turbine blade is dominated by dynamic stall, eliciting large load peaks. However, there has yet to be a comprehensive study of global and local blade loadings for a broad range of flow conditions representative of full-scale unsteadiness. The significance of

the angle of attack parameter on the unsteady loadings along the blade span has yet to be considered. Other than the work of Milne et al. (2016), no documentation of dynamic stall occurring on tidal turbine blades exists. Yet, it is known to occur on all type of horizontal-axis wind turbines where skewed flow, shear, turbulence or tower shadow effects are present (Butterfield et al., 1991). Since tidal turbine blades will also experience these effects with the addition of waves, it is likely that dynamic stall occurs. In addition, the difference between the mean value and the steady state has yet to be quantified. Understanding the unsteady flow around the blade and the resulting unsteady loads is of paramount importance to improve the reliability of tidal turbines without over-engineering components and increasing the LCOE. Moreover, detailed knowledge of the unsteady loads will enable the development of novel technology to mitigate the fatigue loadings and enhance the durability of tidal turbines (Tully and Viola, 2016; Young et al., 2016).

1.6 Research aims and objectives

The aim of this research was to assess the unsteady forces experienced by a tidal turbine blade and identify the conditions where unsteady effects are significant compared to quasi-steady approximations. This is an open research question as experimental work has led to conflicting conclusions.

The first objective of this thesis was to develop an efficient unsteady load model for arbitrary forcing which incorporates state of the art theory. This model was to be able to both synthetically model the onset flow conditions or take as an input flow velocity measurements. With the model developed the next objective was to quantify the unsteady affects by addressing the following research questions, in order of importance:

(a) Which flow conditions (e.g. large waves, yaw, etc.) elicit the most significant load fluctuations, which includes quantifying the velocity fluctuations and angles of attack experienced by the blade in different flow conditions.

(b) For these conditions, how does unsteadiness manifests along the span of the blade? Which blade section incurs the largest load fluctuations? Does added mass amplify or attenuate the loads? Is the effect of shed vorticity significant? and does shed vorticity from returning and neighbouring wakes change the loads signifi-

cantly? Is dynamic stall occurring? and if so does it result in leading-edge vortex shedding?

(c) How important is modelling the unsteady hydrodynamics as opposed to using a simpler less computationally intensive quasi-steady approximation?

1.7 Thesis synopsis

Following on from this introductory chapter, the remainder of the thesis comprises three parts. Part I presents the background on the unsteady flow and load phenomena and modelling techniques. Part II details the formulation of an unsteady flow and load model to analyse loading on tidal turbine blades, and provides some validation cases. Part III contains the results chapters which address the research questions using the developed model.

Part I: Background

Chapter 2: Onset flow experienced by a tidal turbine blade

Chapter 2 presents the unsteady flow conditions encountered by a tidal turbine blade. The parameters which describe the position of a tidal turbine in a tidal channel water column are introduced. Then, spatial variations in the tidal current with depth are described, with a power law representation provided to model the resulting velocity profile. Turbulence measurements at different sites are reviewed and the statistical parameters required to characterise the random nature of the turbulent velocity fluctuations defined. Then methods to introduce synthetic turbulence velocity fluctuations are described, which focuses on the von Kármán atmospheric spectrum. A review of ocean gravity waves and their variability at different tidal sites is given. The chapter concludes by presenting Stokes 2nd order wave theory which defines wave particle velocities in space and time and a simple correction for wave-current interaction.

Chapter 3: Rotor blade hydrodynamics

Chapter 2 introduces the fundamental steady hydrodynamics for a rotor blade. The force and velocity components acting on a blade section are presented. A brief review of the rotational forces and modelling techniques used to correct the load coefficients due

to rotational augmentation are discussed. The effect that the rotor has on the incoming flow is described and the modelling technique, blade-element momentum theory and its various corrections presented. Lastly, the potential velocity field induced by a support structure, such as a tower, is discussed along with a simple potential flow modelling approach.

Chapter 4: Unsteady hydrodynamics

Chapter 4 introduces unsteady flow. A review of the physical flow phenomena which may occur during both attached and separated flow is given. Then low-order modelling techniques to predict the unsteady load coefficients are explained. Which begins with the classical analytical theories valid for attached flow and moves on to dynamic stall modelling techniques for separated flow. The chapter concludes with a short description of the Beddoes-Leishman model which has widely been used in the helicopter industry.

Chapter 5: Unsteady loads on rotor blades

Chapter 6 expands on the theory and modelling techniques introduced in Chapter 5 by investigating how dynamic stall occurs on wind turbine blades so as to better understand how it may occur on tidal turbine blades. Firstly, experimental data from unsteady wind tunnel tests for a range of wind turbine blade-section geometries are examined to reveal how dynamic stall occurs as the load amplitude and geometry thickness increases. After which a number of Beddoes-Leishman type dynamic stall models, developed specifically for wind turbine blades are reviewed. This leads to the identification of a modern low speed model for wind turbine blades, which is described in detail.

Part II: Method

Chapter 6: Formulation of the model

In Chapter 6 a model is formulated comprising the theories and modelling techniques discussed and reviewed in the preceding chapters. Firstly, the parameters of the commercial-scale tidal turbine rotor to be analysed are given. Next, the method to create a synthetic flow field and the formulation of an unsteady load model for tidal turbines are described. The model comprises three components: angle of attack time series, dynamic load coefficients and rotational augmentation, which are coupled to-

gether. The chapter concludes by describing the code implementation and quantifying the computational costs.

Chapter 7: Evaluation of the model

In Chapter 7 the model is validated. Firstly, the blade-element momentum implementation is validated using AeroDyn, an open source software provided by NREL. Next, the dynamic stall model is validated using wind tunnel test data, for a pitching foil. Lastly, a global validation is carried out using tank scale measurements of the root bending moment time history during wave loading.

Part III: Results

Chapter 8: Blade response to unsteady flow

In Chapter 8 a parameter study is carried out to determine which conditions elicit the most significant load fluctuations and to ascertain the importance of the unsteady phenomena occurring. A wide range of flow and operating conditions are synthesised and the responses categorised by the standard deviation of the root bending moment and the ratio between the unsteady and the quasi-steady mean values, this latter quantity reveals when dynamic stall has a global affect on the loads. After identifying the conditions which elicit the most significant load fluctuations. These are used to select combined realistic flows which are further examined to reveal how unsteadiness manifests along the span of the blade. The chapter concludes by investigating how unsteadiness is effected during power control when the current speed exceeds the rated velocity.

The results from this chapter reveal that large waves above all induce the most significant load fluctuations, and that dynamic stall has a global effect when operating at low-tip speed ratios, during very large waves and during a severe yaw misalignment.

Chapter 9: Unsteady loads due to large wave conditions

The findings of Chapter 8 are expanded by using flow velocity measurements taken at the European Marine Energy Centre. A sample containing a large wave train is identified and used as an input to the unsteady load model. As well as investigating the unsteady load fluctuations on the blade, analysis of the rotor performance is undertaken

to determine if these large wave events affect the mean power and thrust of the rotor. The analysis concludes by exploring how the unsteadiness and mean rotor loads are effected when operating below the optimum tip-speed ratio.

The key results from this chapter are that the mean performance of the rotor is not significantly altered by large waves and that modelling dynamic stall has negligible effects on the mean loads provided that the rotor is not operating below the optimum tip-speed ratio.

Chapter 10: Conclusions

Lastly, Chapter 10 summarises the key results and outcomes from the previous chapters. Some recommendations to further develop the model and to expand the results are herein given.

1.8 Research outputs

The following journal papers, conference proceedings and abstracts are outputs from the research outlined in this thesis.

Journal papers

- Scarlett GT and Viola, IM, Unsteady hydrodynamics of tidal turbine blades, Renewable Energy, 2020, 146, 843-855.

- Scarlett, GT, Sellar, B, van den Bremer, T and Viola, IM, Unsteady hydrodynamics of a full-scale tidal turbine operating in large wave conditions, Renewable Energy, 2019, 143, 199-213.

Conference papers

- Scarlett GT and Viola, IM, 2019, Unsteady hydrodynamics of tidal turbine blades, The 13th European Tidal and Wave Energy Conference 2019 (EWTEC2019), Napoli, Italy, 01/09/2019 -06/09/2019.

- Scarlett, GT, van den Bremer, T, Sellar, B and Viola, IM, 2018, 'Unsteady hydrodynamics of full-scale tidal turbines'. In the proceedings of the European

Conference on Computational Mechanics (Solids, Structures and Coupled Problems) (ECCM 6) and the European Conference on Computational Fluid Dynamics (ECFD 7), Glasgow, United Kingdom, 11/06/18 - 15/06/18.

- Scarlett, GT, van den Bremer, T, Sellar, B and Viola, IM, 2018, 'Unsteady hydrodynamics of full-scale tidal turbine blades'. In the proceedings of the 6th Oxford Tidal Energy Workshop (OTE2018), Oxford, United Kingdom, 26/03/18 - 27/03/18 (peer-reviewed 2pp extended abstract).

- Scarlett, GT and Viola, IM, 2016, 'Unsteady tidal turbine blade loading; an analytical approach'. In the proceedings of the 5th Oxford Tidal Energy Workshop (OTE2016), Oxford, United Kingdom, 21/03/16 - 22/03/16 (peer-reviewed 2pp extended abstract).

- Viola, IM, Tully, S and Scarlett, GT, 2016, 'Unsteady hydrodynamics of flexible submerged foils'. In the proceedings of the 5th Oxford Tidal Energy Workshop (OTE2016), Oxford, United Kingdom, 21/03/16 - 22/03/16 (peer-reviewed 2pp extended abstract).

Conference abstracts

- Scarlett, GT, van den Bremer, T, Sellar, B and Viola, IM, 2018, 'Tidal turbine hydrodynamics'. In the proceedings of the UK Fluids Conference 2018, Manchester, United Kingdom, 04/09/2018 - 06/09/2018 (abstract with presentation).

- Scarlett, GT, van den Bremer, T, Sellar, B and Viola, IM, 2018, 'Unsteady hydrodynamics of full-scale tidal turbines'. In the proceedings of the 31st Scottish Fluid Mechanics Meeting 2018, Aberdeen, United Kingdom, 29/05/2018 (abstract with poster).

Part I

Background

Chapter 2

Onset flow experienced by a tidal turbine blade

In this first background chapter the unsteady characteristics of the onset flow are discussed. Firstly, the geometry and parameters which describe the position of a tidal turbine in the water column are introduced. Then, spatial variations in the tidal current with depth are described along with a power law representation to model the resulting velocity profile. Turbulent velocity measurements at different sites are reviewed and the statistical parameters required to characterise the random nature of turbulence defined. Then methods to introduce synthetic turbulence velocity fluctuations are describe, which focuses on the von Kármán atmospheric spectrum. A review of ocean gravity waves and their variability at different tidal sites is given. The chapter concludes by presenting Stokes 2nd order wave theory which defines wave particle velocities in space and time and a simple correction for wave-current interaction.

2.1 Geometrical parameters

To describe the flow incident to a tidal turbine blade it is convenient to first introduce the geometry. Schematic views of the port and front sides of a 3-bladed, bottom mounted tidal turbine are shown in Figure 2.1. A Cartesian coordinate system is placed at the still water level (SWL). The freestream current velocity is in the x direction, y is the port side direction and z is the vertical coordinate positive above the SWL with the hub located at $z = z_0$. A cylindrical coordinate system with origin at the hub describes the radial (r) position along the blade, which extends to tip (R), and the azimuthal

angle of the blade (ψ), which tracks the position of the blade as it rotates anti-clockwise from the z-axis where $\psi = 0$. Also shown are the radius of the hub (R_h) and the water depth (d).

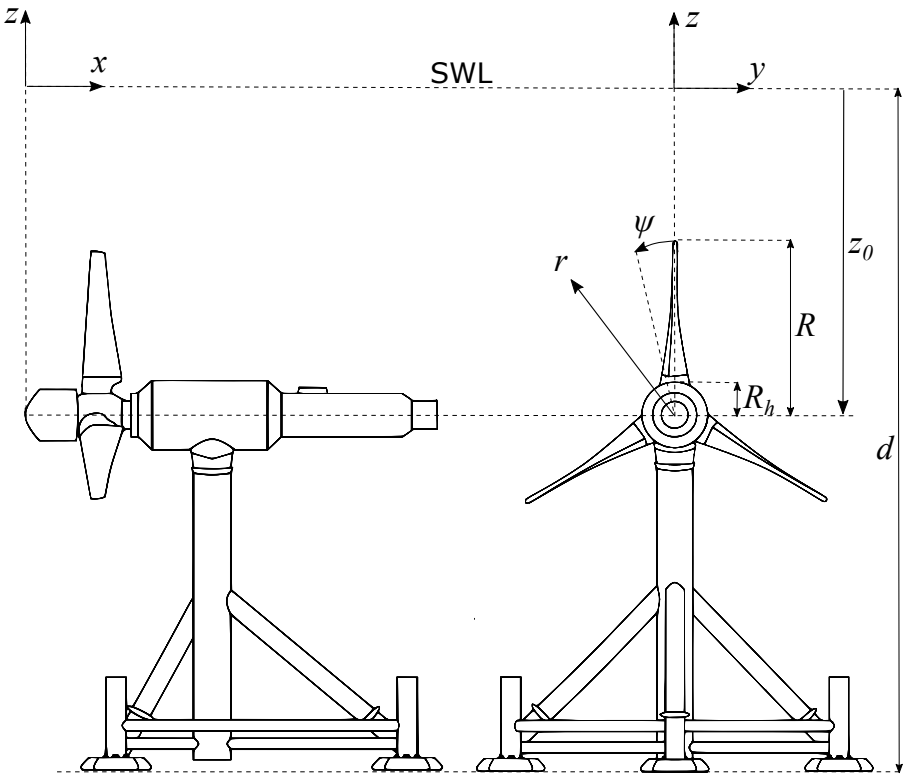

Figure 2.1: Schematic diagram of the tested tidal turbine.

2.2 Sheared current

The magnitude of the mean current velocity measured at EMEC fluctuates between 0 - 4 m^{-1} due to the tidal cycle. The presence of the seabed, coast line and free surface produces a channel boundary layer resulting in spatial variability of the current velocity. The horizontal current velocity (U_x) is non-uniform with depth due to the presence of the bed, which causes a reduction in the velocity profile with depth. Hence, a tidal turbine blade will experience a once per revolution forcing every rotation. At the bed there is no slip ($U_x(-d) = 0$), and at the still water level $U_x(0) = U_\infty$. The U_x profile is then defined using a power law approximation:

$$U_x = U_\infty \Big(\frac{z+d}{d}\Big)^\nu, \tag{2.1}$$

for $-d \leq z \leq 0$. The value of ν can range between 0.1 and 0.25 depending on the bed roughness (Soulsby, 1983). At EMEC McCann et al. (2008) reported that ν varies between 0.1 and 0.19, whereas Sellar et al. (2018) reported that the standard 1/7 power law represents the velocity profiles well during flood tide, but, during an ebb tide the power law approximation breaks down due to the flow retarding back from the mid-depth to the free surface.

2.3 Turbulence

In this section sources of turbulence in a tidal channel and wake are discussed along with the difference modelling techniques. Then the method to create a turbulent velocity time series using the von Kármán spectra is described.

2.3.1 Turbulence characteristics

Turbulence intensity (I) is one of the major measures which quantifies the magnitude of the turbulent fluctuations in the flow. It is defined as

$$I = \frac{\sqrt{\frac{1}{3}(u_x'^2 + u_y'^2 + u_z'^2)}}{\bar{U}_x} \tag{2.2}$$

where $u_i' = U_i - \bar{U}_i$, and i denotes x, y or z. If the turbulence is approximately isotropic, then $I = I_i, \forall i$. The turbulence length scale (L_i) gives the characteristic length in meters of the energy rich eddies in the flow. It is determined by computing the spatial correlation of u_i' between two points, as the separation distance between the points increases the correlation will decay to zero, integrating over this distance then gives L_i (Pope, 2001). Flows with large eddies will remain correlated over longer distances or time period. If only a single point measurement exists or the spacing between measurements is insufficient, then L_i can be computed using the autocorrelation of a point in time (t). The correlation coefficient ($R(\hat{t})$) is defined as

$$R(\hat{t}) = \frac{\langle u'(t)u'(t+\hat{t})\rangle}{\sqrt{u'^2}}, \tag{2.3}$$

where the argument $\hat{t}$ is the time lag. Integrating $R(\hat{t})$ with respect to $\hat{t}$ gives the integral time scale (τ_i):

$$\tau_i = \int_0^\infty R(\hat{t})\mathrm{d}\hat{t}. \tag{2.4}$$

Then by assuming Taylor's frozen turbulence hypothesis such that fluctuations advect with the mean velocity between two points in a frozen state, L_i can be defined as

$$L_i = \bar{U}_i \tau_i. \tag{2.5}$$

2.3.2 Turbulence incident on tidal turbine blades

Tidal energy sites are highly turbulent with Reynolds numbers in the order of 10^8 reported (Milne et al., 2017). The turbulence characteristics vary with channel width, bed roughness and, tidal cycle (Sellar et al., 2018; Thomson et al., 2012). Values of I at hub height are reported to be approximately 10% for both Puget Sound, USA (Thomson et al., 2012) and the Fall of Warness, Orkney, UK (Sellar et al., 2018) and 6-8% at the Sound of Islay (Milne et al., 2016). Turbulence is distorted as it approaches the turbine due to the expansion of the turbulent wake behind the rotor. Rapid distortion theory (RDT) developed by Batcherlor and Proudman (1954) can be used to predict the change in turbulence intensity as it passes through the rotor. Graham (2017) used RDT to predict the amplification of the streamwise turbulent velocity for a rotor perpendicular to the flow. He found the amplification only becomes significant towards the tip of the blade. The model was later extended by Milne and Graham (2019) to include a fluctuating potential flow. They then predicted that for a tidal turbine operating below rated power that the distortion has the effect of attenuating the low frequency fluctuations, whereas when operating above rated power the intensity of the fluctuations were amplified. These predictions were found to agree qualitatively with full-scale data.

2.3.3 Spectral methods of synthesising turbulence

Turbulent velocity fluctuations can be synthesised using a spectral method such as the von Kármán atmospheric turbulence spectrum (Diederich et al., 1957), or the Kaimal spectra, both of which have widely been used in the wind industry (Burton et al., 2011). At present there is only one spectral model reported for a tidal site (Jonkman and Kilcher, 2012) which was developed using measurements of the flow structure at the Puget Sound. This model takes the friction velocity and reference hub height as

an input, rather than L_i, thus fine tuning is required to achieve the desired L_i. In addition, the channel depth of 18 m is quite site specific and not representative of where a commercial scale tidal turbine rated at 1 MW or above will be deployed. Recent characterisation studies of the turbulent flow structure at the Sound of Islay ascertained that the von Kármán spectra predicted well the measured velocity spectra (Milne et al., 2013b, 2017).

Synthetic eddy methods for synthesising three dimensional turbulence

If spatial correlations of the flow exist, then state of the art spectral methods can simulate spatially coherent, three-dimensional turbulence. For spectral methods this is done using the Sandia method (VEERS, 1984). The Sandia method is well established in the wind energy industry for generating turbulent velocity fields the. The approach is to compute a cross spectrum between spatial points using a coherence function. Various correlations of the flow exist for wind turbines, however, for tidal channels such correlations are yet to be established. Another approach of generating spatially coherent turbulence is the Synthetic Eddy Method (SEM) (Jarrin et al., 2006). As discussed in subsection 1.4.1 this method is primarily used as an initial condition for Large Eddy Simulations. Carlier et al. (2015) carried out a study into using the SEM to generate ambient turbulence in a tidal channel. Togneri et al. (2018) utilised both the Sandia and SEM inside a blade-element momentum model and reported little differnce between the two models. Mullings and Stallard (2018) used both the von Kármán spectrum and the SEM to recreate tank scale turbulent flow. The authors found that the recovered values of L from the simulations were better conserved using the von Kármán spectrum than the SEM, with observed differences of 10% and 20%, respectively, between the input and output.

2.3.4 Generation of a turbulent velocity time series using the von Kármán spectrum

The streamwise von Kármán spectra S_x is defined as

$$S_x = \frac{4L_x\sigma_x}{\bar{U_x}} \frac{1}{(1+70.7n^2)^{\frac{5}{6}}}, \tag{2.6}$$

where σ_x is the standard deviation, defined as $\sigma_x = I_x \bar{U}_x$, $n = L_x f_t / \bar{U}_x$ and f_t is the turbulent frequency component. The spectra in the y-direction is

$$S_y = \frac{4 L_y \sigma_y}{\bar{U}_x} \frac{1 + 753.6 n^2}{(1 + 282.8 n^2)^{\frac{11}{6}}}, \tag{2.7}$$

where $\sigma_y = R_t \sigma_x$, $L_y = R_t L_x$ and R_t is the anisotropy ratio. For $R_t = 1$, turbulence is isotropic and anisotropic if $R_t < 1$. The vertical component $S_z = S_y$. Streamwise velocity spectra are shown in Figure 2.2 for $L_x = 2$ m and 5 m, and $I_x = 10\%$ and 20%. These show that as L_x increases the value of f_t at which energy transfers from the integral scale to the inertial subrange occurs at a lower frequency. Increasing I_x amplifies the energy content in S_x. A velocity time series can be simulated from a von

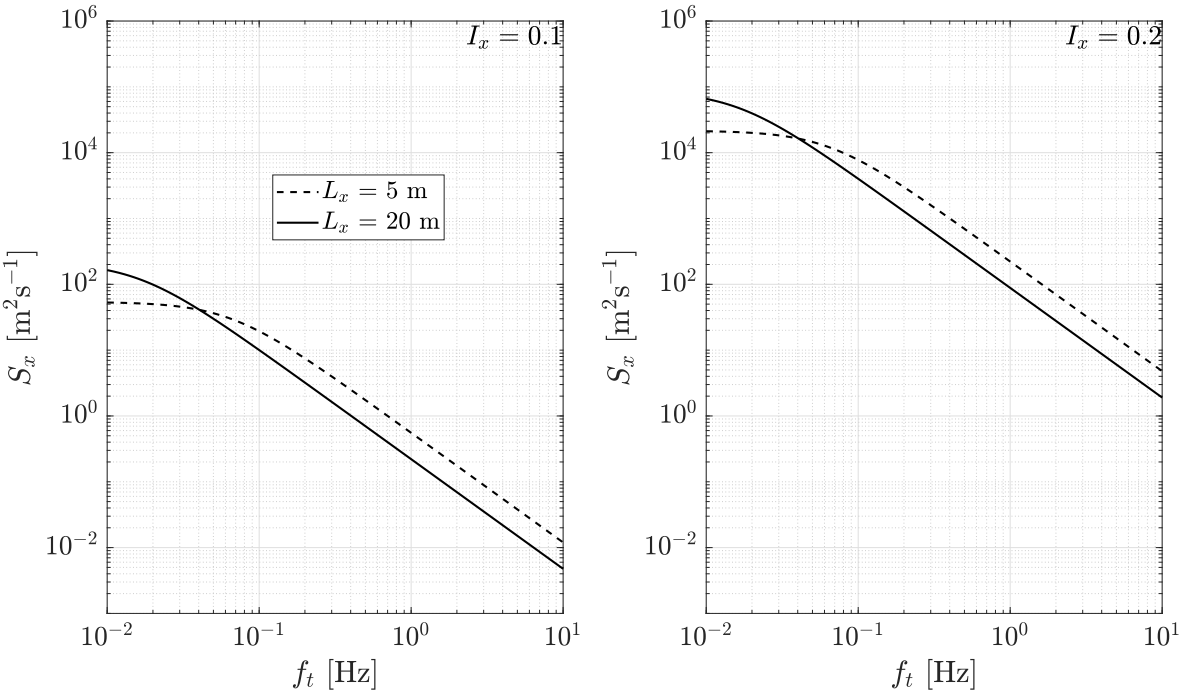

Figure 2.2: Stream wise turbulent kinetic energy recreated using the von Kármán spectrum for length scales of 5 m and 20 m and turbulent intensity of 10% and 20%.

Kármán spectrum using the method of Shinozuka (1972):

$$u_i' = \sqrt{\frac{2}{N}} \sum_{j=1}^{N} \sqrt{S_{ij}} \cos\big(2\pi f_{t_j} t + \Phi_j\big), \tag{2.8}$$

where N is the number of f_t components and Φ is the phase angle, which is a random value, distributed uniformly between 0 and 2π.

2.4 Waves

A tidal turbine will encounter a wide range of surface waves. Regular linear waves are periodic and sinusoidal; yet in the ocean waves are almost never perfectly regular. They are irregular, with randomly varying amplitude, period and direction. However, such sea states can by modelled by the linear superposition of many regular waves. The components can then be analysed in the frequency domain making a Fourier transform of the time domain signal to give a frequency amplitude spectra of representative regular wave periods ($T_w(f)$) and heights ($H(f)$). Statistical quantities can then be used to described random waves. The significant wave height (H_s), is the average height of the 1/3 largest observed waves, which is equivalent to H_{m0}, the zero moment computed from the power spectrum. The zero crossing wave period (T_z), is the average time between the upward and downward crossings of the zero line or SWL, and the peak wave period (T_p) which is the period corresponding to the most energetic frequency in the wave spectrum (Holthuijsen, 2007).

At the EMEC tidal site reported annual average and extreme values for H_s and T_z are 2 m and 6 s, and 10 m and 10 s, respectively (Norris and Droniou, 2007). In the winter months large peaks occur due to storm conditions. At the Fromveur Strait site in Western Brittany mean values of $T_z = 10$ s and $H_s = 3$ m were reported during November (Guillou et al., 2016), and at the Skerries tidal site in Anglesey, $T_z \approx 9$ s and $H_s > 5$ m have been reported during January (Hashemi et al., 2015).

Wave particle velocities decay with depth. Thus a tidal turbine blade section will experience a time-varying velocity as it rotates at period T_r through a velocity profile that oscillates with wave period T_w about the mean velocity profile and for which the rate of decay of velocity amplitude with depth is a non-linear function (Equation 3.13) of wave period. The relative velocity to the blade will therefore be across a range of periods/frequencies. In deep water a wave particle will follow a circular orbit which decreases in size with increasing distance from the surface approaching zero by $z = -L_w/2$, where L_w is the wave length. In shallow water the bottom boundary causes the wave orbital to flatten into an ellipse.

A plethora of theories exist to model waves. One of the earliest and simplest is linear

(Airy) wave theory (Airy, 1841), in which the wave problem is addressed by solving the Laplace equation with linearised freesurface and the bottom boundary conditions. This restricts the analysis to wave amplitudes (a_0) which are small compared to the wavelength, or more formally that the steepness, $Ka_0 \ll 1$, where K is the wavenumber in m^{-1}. This range insures that the waves are not breaking. Stokes 2nd order wave theory extends linear theory by expanding the boundary conditions to second order (Stokes, 1847). This introduces into the equations a superharmonic component describing the self interaction, for monochromatic waves (see Dean and Dalrymple (1991)), and wave-wave interactions for a wave train (see Dalzell, 1999). For a tidal turbine blade the difference between linear and 2nd order non-linear waves is negligible for small waves. Larger waves, however, exhibit more non-linearity such that the crests are sharper and the troughs flatter. This means that the peak velocities and accelerations will be larger, albeit for a shorter period. The will be less pronounced with depth. Therefore the blade will experience more variation in wave orbital velocities over its depth range.

The streamwise wave particle velocity for monochromatic waves from Stokes 2nd order wave theory is

$$W_x = \frac{gHK}{2\omega_a}\frac{\cosh K(z+d)}{\cosh(Kd)}\cos(Kx-\omega_a t)+\frac{3}{16}H^2\omega_a K\frac{\cosh 2K(z+d)}{\sinh^4(Kd)}\cos\Big(2(Kx-\omega_a t)\Big), \tag{2.9}$$

and the depthwise particle velocity (U_z) is

$$W_z = \frac{gHK}{2\omega_a}\frac{\sinh K(z+d)}{\cosh(Kd)}\sin(Kx-\omega_a t)+\frac{3}{16}H^2\omega_a K\frac{\sinh 2K(z+d)}{\sinh^4(Kd)}\sin\Big(2(Kx-\omega_a t)\Big), \tag{2.10}$$

where H is the wave height, d is the depth from SWL (see Figure 2.1), t is time, g is gravitational acceleration and ω_a is the apparent angular velocity. The wavenumber is determined by solving the linear dispersion relation given by

$$\omega_a^2 = gK\tanh(Kd). \tag{2.11}$$

This important relation describes the evolution of waves. It can be shown that in deep water ($Kd \gg 1$) the phase speed of a wave is independent of d, and that longer waves travel faster. In shallow water, waves travel at the same phase speed which is a function of d.

Waves interact with the current: when they follow it they are elongated and when

they oppose it they are shortened. In the Pentland Firth a study to quantify wave energy found that the energy can be attenuated or amplified in following and opposing currents, respectively, by up to 60% (Saruwatari et al., 2013). The wave period is altered by the superposition of a uniform current. The relative wave period, T_w is the period observed when travelling with the current. Whereas for a fixed observer at the turbine hub the apparent wave period (T_a) is observed which includes the Doppler shift due to the current. In the case where there is no current, T_w is equivalent to T_a. The Doppler effect can be modelled by making a simple modification to the linear dispersion relation to superimpose the effect of the current. The modified relation is given by

$$(\omega_a + KU_\infty \cos\theta)^2 = gK \tanh(Kd), \tag{2.12}$$

where θ is the oblique wave angle relative to U_∞. For a velocity, which does not vary with depth.

The effect of the current on the horizontal wave particle velocity at hub height are shown in Figure 2.3, for waves with zero current, following current and opposing current. The current velocity at hub height is 2.8 ms^{-1}, $H = 5$ m, $T_w = 10$ s, the total depth is 45 m and the hub is at a depth of 27 m. As shown, waves which follow the current have a greater standard deviation, compared to waves with zero current, whereas for opposing waves, the standard deviation is significantly reduced from the zero current case.

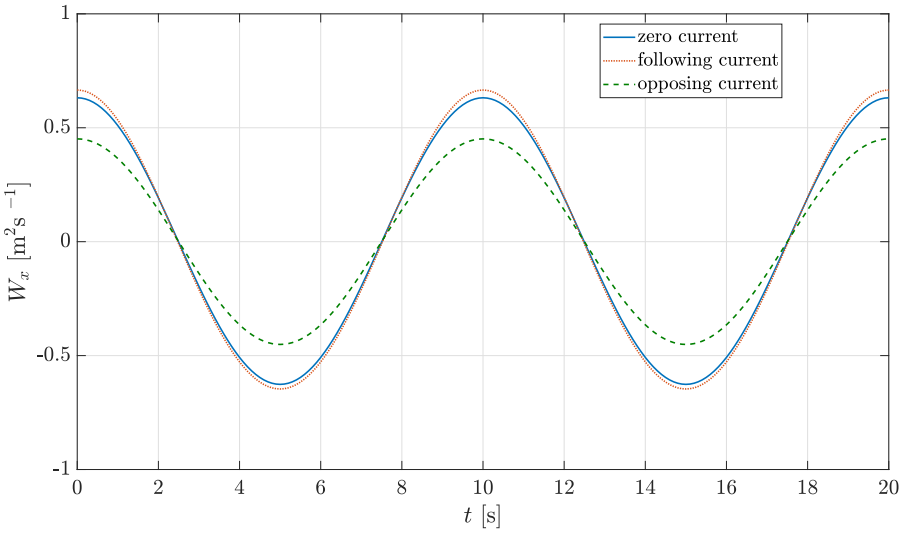

Figure 2.3: Time series of the streamwise wave particle velocity at hub height for waves with zero current, following current and opposing current.

The velocity components for the onset flow conditions described in this chapter are combined as described in section 6.2. They are used in Chapter 7 to analyse the unsteady load response for a wide range of flow cases.

Chapter 3

Rotor blade hydrodynamics

This second background chapter introduces the fundamental steady hydrodynamics for a rotor blade. The rotation of a streamline body such as an aeorofoil/hydrofoil introduces different hydrodynamic effects compared to a static foil. The force and velocity components acting on a blade section are given along with geometrical parameters. A brief review of the rotational forces and modelling techniques used to correct the load coefficients due to rotational augmentation are discussed. After which the effect that the rotor has on the incoming flow is described and the modelling technique, blade-element momentum theory and its various corrections presented. Lastly, the potential velocity field induced by a support structure such as a tower is discussed along with a simple potential flow modelling approach.

3.1 Blade section force components

A horizontal axis tidal turbine is a lift device. The blades comprise of streamline sections which promote the curvature of flow around them which creates a pressure gradient and subsequent lift force (Babinsky, 2003). The velocity and force components acting on a blade section are shown in Figure 3.1 (a) and (b), respectively. The tangential velocity component (U_ψ) is defined as $U_\psi = U_z \cos\psi + U_y \sin\psi + \Omega r$, where Ω is the rotor speed in [rads^{-1}]. The relative velocity (U_r) is the vector sum of the axial velocity $U_x(1-a)$ and the tangential velocity $U_\psi(1+a')$, where a and a' are the axial and tangential induction factors, respectively. The angle of attack (α) is the angle that U_r makes with with the chord line (c), $\beta = \beta_g + \beta_p$ is the pitch angle which is measured between c and the rotor plane, where β_g is the geometrical twist angle of the blade section and β_p is

any operational pitch which may be applied to the blade. The flow angle is $\phi = \alpha + \beta$. The sectional drag force (F_D) which is codirectional with U_r and the lift force (F_L)

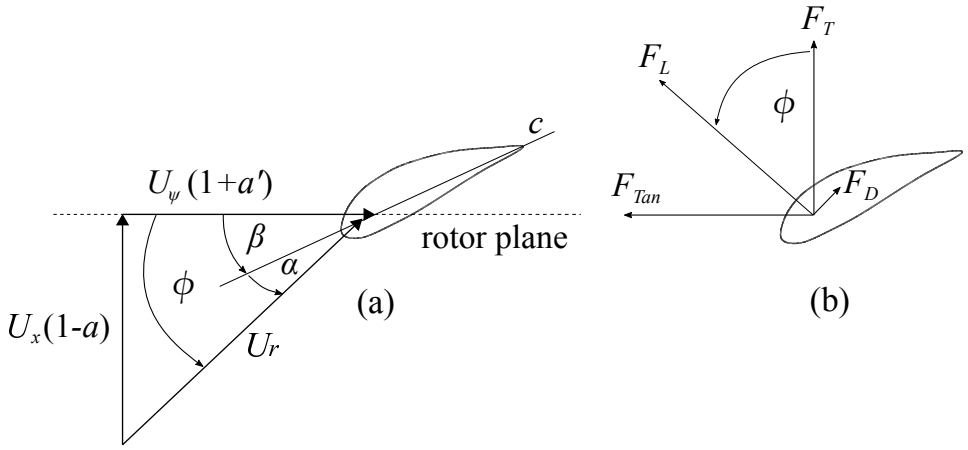

Figure 3.1: Blade section diagram showing (a) velocity components and (b) force components.

perpendicular to it are defined per unit length as

$$F_D = \frac{1}{2} C_D \rho U_r^2 c, \quad F_L = \frac{1}{2} C_L \rho U_r^2 c, \tag{3.1a, b}$$

where C_D and C_L are the sectional coefficients of drag and lift, respectively and ρ is the fluid density. The axial force known as thrust (F_T) is perpendicular to the rotor plane and is responsible for the blade bending around the y-axis known as root bending moment (M_y). The tangential force (F_{Tan}) drives the turbine and causes bending around the x-axis referred to as edgewise bending moment (M_x). F_T and F_{Tan}, expressed in terms of F_D and F_L, are

$$F_T = F_L \cos\phi + F_D \sin\phi, \quad F_{Tan} = F_L \sin\phi - F_D \cos\phi, \tag{3.2a, b}$$

which given in coefficient form are

$$C_{F_T} = C_L \cos\phi + C_D \sin\phi, \quad C_{F_{Tan}} = C_L \sin\phi - C_D \cos\phi. \tag{3.3a, b}$$

The blade bending moments are then defined as

$$M_y = \int_{R_h}^{R} F_T \cdot r \cdot \mathrm{d}r, \quad M_x = \int_{R_h}^{R} F_{Tan} \cdot r \cdot \mathrm{d}r. \tag{3.4a, b}$$

3.2 Rotational augmentation

In the rotor environment stall is delayed to higher angles of attack leading to an increased lift force compared to a non-rotating blade for the same angle of attack.

The National Renewable Energy Laboratory (NREL) investigated the effects of both unsteadiness and rotation on a 10.1 m diameter wind turbine employing NREL S809 profiles (Hand et al., 2001). This study, named the NREL Phase VI test, found that for inboard blade sections both lift and drag force are augmented compared to a non-rotating blade. However, conversely, for outer blade sections, both lift and drag are reduced. Steady values for C_L and C_D from these tests are shown in Figure 3.2 for a blade section near the root ($r \approx 0.3R$) and a section near the tip ($r \approx 0.95R$).

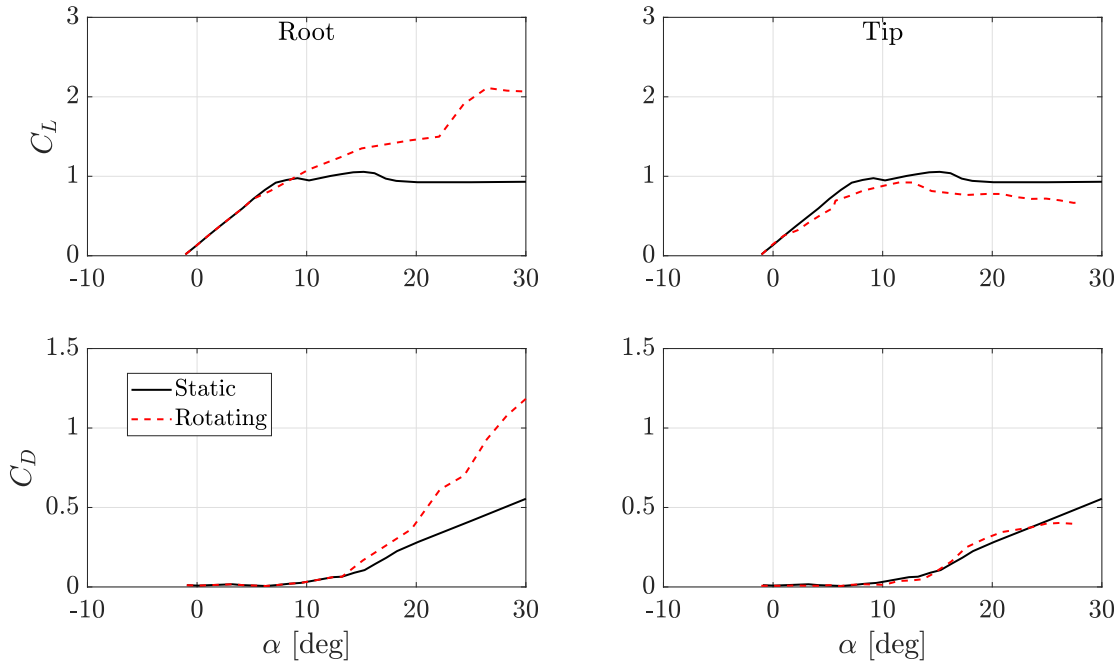

Figure 3.2: Measured lift and drag coefficients at blade locations near the tip and hub for a rotating and non-rotating blade. Data from the NREL Phase VI test of a 10.1 m diameter wind turbine (Hand et al., 2001).

The physics which cause rotational augmentation are not very well understood. It is widely agreed (Harris, 1966; Klimas, 1986; Eggers and Digumathi, 1992; Du and Selig, 2000; Lindenburg, 2004) that the blade rotation induces a centrifugal force, which acts on the fluid that rotates with the blade, such as the boundary layer, separation bubbles and the separated flow region near the trailing edge, causing a spanwise flow, towards the blade tip. Since the flow is moving perpendicular to the rotation it experiences an

apparent Coriolis force which deflects it towards the trailing edge. These effects reduce the adverse pressure gradient in the boundary layer to promote flow reattachment and delay stall, which in turn leads to lift augmentation from the stationary value (Du and Selig, 2000). The chordwise pressure distribution consists of a large suction peak just aft the leading edge which decreases towards the trailing edge. The magnitude of the suction peak is proportional to U_r, and since $U_r \propto r^2$, the peak increases towards R. The leads to a mechanism referred to as "centrifugal pumping" (Eggers and Digumathi, 1992), whereby the chordwise negative pressure gradient and spanwise dynamic pressure gradient enable the fluid in separated regions to flow towards the tip and overcome the Coriolis force (Lindenburg, 2004).

Modelling this behavior is a challenge. Breton et al. (2008) tested the prediction capabilities of a number of rotational augmentation models to predict the NREL Phase VI test data. Their study determined that none of the models could satisfactorily predict C_L and C_D across the entire blade span, and that only the model of Lindenburg (2004) successfully captured a reduction in C_L at the outer sections.

The expression for the lift coefficient corrected for rotation (C_L^{rot}) given by Lindenburg is

$$C_L^{rot} = C_L + \frac{b_3 c}{r}\cos^2(\phi)((1-f)^2\cos\big(\alpha^{rot}\big) + b_4\cos\big(\alpha^{rot} - \alpha_0\big)), \tag{3.5}$$

where b_3 and b_4 are empirical coefficients tuned to the NREL S809 using data from the NREL Phase VI tests, f is the trailing edge separation point, α_0 is the zero lift angle and $\alpha^{rot} = \alpha + \delta\alpha^{rot}$ is the equivalent rotational angle of attack with the following shift applied

$$\delta\alpha^{rot} = \frac{b_3 b_4 c}{2\pi r}\cos^2(\phi). \tag{3.6}$$

At the outer sections ($r \geq 0.8R$) where a reduction from the non-rotating lift and drag values occur C_L^{rot} is given as

$$C_L^{rot} = C_L - \Big(\frac{\cos^2(\phi)\exp(-1.5A_{R_{\text{out}}})C_L(C_{N_\alpha}(\alpha-\alpha_0)-1)}{C_{N_\alpha}(\alpha-\alpha_0)}\Big), \tag{3.7}$$

where $C_{N_\alpha} = \frac{\mathrm{d}C_N}{\mathrm{d}\alpha}|_{\alpha_0}$ is the slope evaluated at α_0 and $A_{R_{\text{out}}}$ is the aspect ratio of the part of the blade outboard of the section; r_i, which is being analysed. It is defined as

$$A_{R_{\text{out}}} = \frac{(R-r_i)^2}{\int_R^{r_i} c\,\mathrm{d}r}. \tag{3.8}$$

Lindenburg defines the drag coefficient corrected for rotation (C_D^{rot}) at all sections as

$$C_D^{rot} = C_D \frac{b_3 c}{r} \cos^2(\phi)(1-f)^2 \sin\left(\alpha^{rot}\right), \tag{3.9}$$

3.3 Blade-element momentum theory

To determine the forces acting on a rotor's blade one must consider the affect that the rotor has on the flow. As shown in Figure 3.1 the rotor induces a velocity ($u_0 = -aU_\infty$) which opposes the freestream and a velocity ($a'U_\psi$) which opposes the rotation. The simplest method to determine the induction factors is blade-element momentum (BEM) theory. As the name implies it is a combination of blade-element and momentum theory. There are a number of limitations and assumptions to the theory: (1) a steady flow, (2) no radial flow (i.e blade sections are independent), (3) that the rotor is perpendicular to the flow, (4) there are an infinite number of blades and (5) that the rotor wake does not become turbulent. Even so modifications and corrections have been developed to circumvent all but (2). A brief description of the model, some corrections and the solution method are given herein.

The following description of blade-element momentum theory is based on the text-book descriptions of Burton et al. (2011). The hydrodynamic forces are equated to the momentum rate of change acting on a blade annulus of width dr and position r on the blade, as shown in Figure 3.3. The blade-element equations describe what is happening

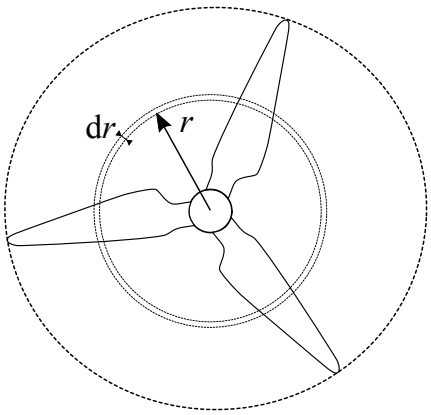

Figure 3.3: Incremental annulus swept out by a blade element.

locally on the blade. They are defined as

$$\mathrm{d}T = N_b \frac{1}{2}\rho U_r^2 C_{F_T} c\,\mathrm{d}r, \quad \mathrm{d}Q = N_b \frac{1}{2}\rho U_r^2 C_{F_{Tan}} c\,\mathrm{d}r, \tag{3.10a, b}$$

where $\mathrm{d}T$ and $\mathrm{d}Q$ are the incremental thrust and torque components acting on the annulus and N_b is the number of blades.

Momentum theory is based on the actuator disc concept where the steady Bernoulli equation is applied upstream and downstream of the disc to determine the maximum extractable energy from the flow, leading to the well known Betz limit. Applying conservation of angular momentum to the actuator disc model and allowing some radial variation leads to the following momentum balance equations for $\mathrm{d}T$ and $\mathrm{d}Q$:

$$\mathrm{d}T = 4\pi r \rho U_x^2 (1-a) a L\,\mathrm{d}r, \quad \mathrm{d}Q = 4\pi r^3 \rho U_x \Omega (1-a) a' L\,\mathrm{d}r, \tag{3.11a, b}$$

where L corrects for the fact that the blades are not infinetely long, thus, tip losses (L_T) and hub losses (L_H) arising from flow leakages at the extremities where a jump in the tangential velocity occurs causing the flow to roll up forming a trailing vortex, which for a rotor forms a helical wake structure. Using the Prandtl model (see Burton et al., 2011, p. 81), tip losses are defined as

$$L_T = \frac{2}{\pi}\cos^{-1}\left[\exp\left(\frac{-N_b}{2}\Big(\frac{1-\mu}{\mu}\Big)\sqrt{1+\frac{(\lambda_r\mu)^2}{(1-a)^2}}\right)\right], \tag{3.12}$$

and hub losses expressed as

$$L_H = \frac{2}{\pi}\cos^{-1}\left[\exp\left(\frac{-N_b}{2}\Big(\frac{\mu-\mu_R}{\mu}\Big)\sqrt{1+\frac{(\lambda_r\mu)^2}{(1-a)^2}}\right)\right], \tag{3.13}$$

where $\mu = r/R$, $\mu_h = R_h/R$ and the $\lambda_r = \Omega r/U_x$. Then the total losses $L = L_T L_H$. The blade-element and momentum equations are equated and rearranged to give the following implicit definitions for a and a':

$$a = \frac{g_1}{1+g_1}, \quad a' = \frac{g_2}{1-g_2}, \tag{3.14a, b}$$

where

$$g_1 = \frac{\sigma_r C_{F_T}}{4L\sin^2(\phi)}, \quad g_2 = \frac{\sigma_r C_{F_{Tan}}}{4L\sin(\phi)\cos(\phi)}, \tag{3.15a, b}$$

and $\sigma_r = N_b c/2\pi r$ is the local solidity.

Momentum theory breaks down for high induction and incorrectly predicts wake reversal and a decrease in thrust for $a > 0.5$. Where in reality the wake enters a turbulent state and the thrust increases as the flow becomes increasingly blocked. To circumvent this corrections are applied from $a > 0.4$. Glauret provides an empirical relationship between a and the thrust coefficient C_T for the entire rotor (see Burton et al., 2011, p. 65). The relationship was further modified by Buhl (2005) for application on individual blade elements. This correction is defined as

$$a = \frac{\tau_1 - \sqrt{\tau_2}}{\tau_3}, \tag{3.16}$$

where

$$\tau_1 \equiv 2g_1 L - \Big(\frac{10}{9} - L\Big), \quad \tau_2 \equiv 2g_1 L - L\Big(\frac{4}{3} - L\Big), \quad \tau_3 \equiv 2g_1 L - \Big(\frac{25}{9} - 2L\Big). \tag{3.17a, b, c}$$

If the turbine is at a yaw angle (γ) to the mean flow then the loadings at a section change as the blade rotates. Blade sections downstream relative to the center of the hub, encounter more of the wake, therefore, a greater induced velocity, whereas, blade sections upstream of the hub, outside of the wake encounter a lower induced velocity. This is problematic since the generalised momentum theory assumes an averaged force at each annulus. Glauert (1926) proposed a simple definition for the axial velocity which was later extended by Pitt and Peters (1981). Here u_0 is either attenuated or amplified by an azimuthally varying component u_1, as illustrated in Figure 3.4. The definition for the azimuthally varying axial induction factor (a_γ) is given as

$$a_\gamma = a\Big(1 + \frac{15\pi}{32}\mu \tan\chi \cos\psi\Big). \tag{3.18}$$

where χ is the wake skew angle which is approximated as $\chi \approx (0.6a+1)\gamma$ (Burton et al., 2011). This post BEM correction is uncoupled from the BEM equations (Equation 3.14 (a) and (b)). A more physical representation would be to correct the velocity terms in the blade-element and momentum equations and then redefine the BEM equations, coupling them with γ. Such an approach has been proposed by Ning et al. (2015) which the same authors plan to implement into the NREL software AeroDyn, however, the complexity of the solution method has so far delayed the implementation.

The BEM equations are solved by first making an initial guess for ϕ, from which β

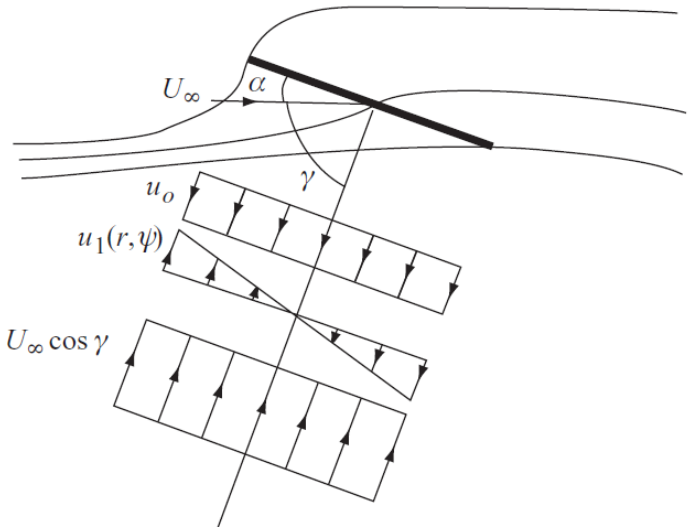

Figure 3.4: Induced velocity components in a skewed flow (reproduced from Burton et al. (2011)).

is subtracted to give α, then the corresponding values of C_L and C_D are selected from look-up tables and C_{F_T} and $C_{F_{Tan}}$ are determined. A new value for ϕ is computed with a and a' and the process continues until convergence. The simplest convergence method is fixed point iteration, however, this is slow and a quicker, more effective solution is obtained using Newton-Raphson iteration. Convergence problems have led to more complex solution methods such as the Monte Carlo initialiser of Masters et al. (2011) and the heuristic smoothing method of Maniaci (2011). Although these methods have improved convergence, they are still not guaranteed to converge (Ning, 2014). A simpler solution method has been developed by Ning (2014), who utilises a residual equation to converge on ϕ rather than solving for both a and a'. This enables the use of a root finding algorithm which guarantees convergence. Using the geometrical definition for ϕ shown in Figure 3.1(a), the following residual equation is formed

$$R(\phi) = \frac{\sin(\phi)}{(1-a)} - \frac{\cos(\phi)}{\lambda_r(1+a')}, \tag{3.19}$$

The value ϕ^* which satisfies $R(\phi) \leq 10^{-6}$ is determined and used in the following iteration to recompute a and a'. The process is repeated until $R(\phi) \leq 10^{-6}$.

3.4 Tower shadow

The presence of a support structure will deflect the flow around it causing a velocity deficit. As a rotor's blade passes the structure it will experience a periodic fluctuation. The support structure could be a monopile, tripod, truss, etc., it could be bed fixed or mounted to some floating structure. Depending on the effected region the fluctuation may occur at multiples of the rotational frequency. However, if the rotor is located far enough upstream of the tower, or is mounted to the side of the tower such as with the SeaGen device (Atlantis Resources Ltd, 2016), then the fluctuations are likely to be negligible.

A simple physical representation of the velocity field due to a tower structure, which causes a velocity deficit in x and an induced velocity in y, is modelled as potential flow around a cylinder (Bossanyi, 2012). For a doublet superimposed on a uniform flow, the stream function (Ψ) is defined as

$$\Psi = U_x\Big[1 - \frac{(\frac{D}{2})^2}{x^2 + y^2}\Big]y. \tag{3.20}$$

where D is the tower diameter, y is the coordinate of the blade relative to the centre of the hub and x is the blade location in front of the tower. The streamwise and transverse velocity components by definition are then

$$V_x = \frac{\partial \Psi}{\partial y}, \quad V_y = -\frac{\partial \Psi}{\partial x}. \tag{3.21a, b}$$

3.5 Yaw correction during waves

If the turbine is yawed relative to the freestream a small correction is made to combine the effect of a yawed rotor sampling waves. When this happens wave particle velocities either lead or lag relative to those experienced at the hub. The correction given by Galloway et al. (2014) is used, where a lag t_γ is applied to t in Equation 2.9 and Equation 2.10, which is defined:

$$t_\gamma = \frac{r \sin\psi \sin\gamma}{U_\infty}. \tag{3.22}$$

The effect of a 20° yaw misalignment on the streamwise wave particle velocities seen by the blade as it rotates is illustrated in Figure 3.5. For a blade section near the hub ($r = 0.15R$), there is little difference in the velocity magnitude for the yawed case. Conversely, for a section near the blade tip ($r = 0.95R$) there is a significant difference, this is due to the increased difference in position relative to the hub. The trends are similar for waves opposing the current ($\theta = 0°$).

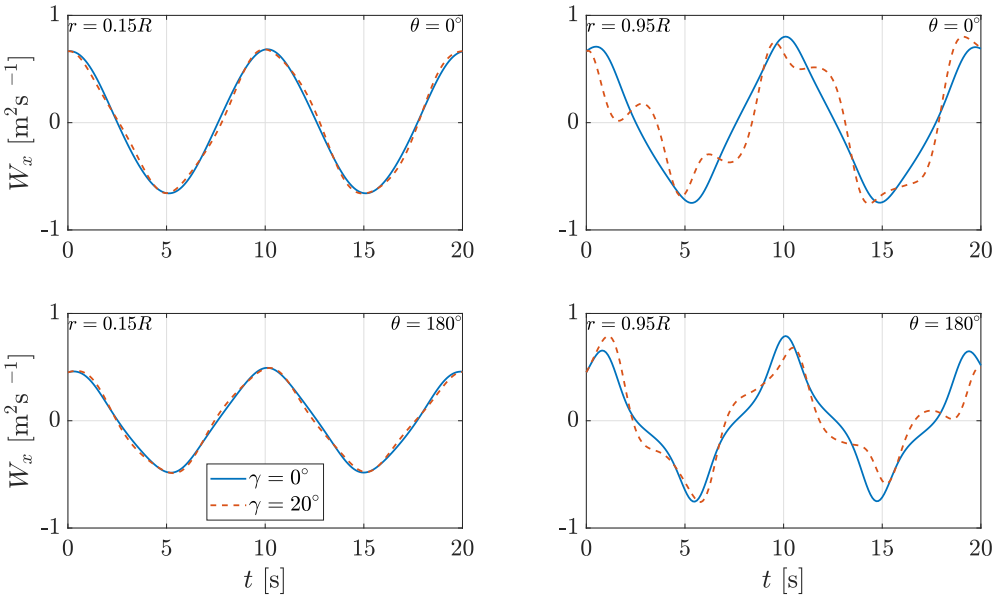

Figure 3.5: Horizontal wave particle velocity seen by the blade near the hub ($r = 0.15R$) and tip ($r = 0.95R$) during a yaw misalignment for following ($\theta = 0°$) and opposing ($\theta = 0°$) waves.

Chapter 4

Unsteady hydrodynamics

This third background chapter introduces unsteady flow. A review of the physical flow phenomena which may occur during both attached and separated flow is given. Then descriptions of low order modelling techniques to predict the unsteady load coefficients are given. This begins by describing classical analytical theories valid for attached flow and moves on to reviewing dynamic stall modelling techniques for separated flow. The chapter concludes with a short description of the Beddoes-Leishman model which has widely been used in the helicopter industry.

The aerodynamic theory introduced in this section are defined using the freestream velocity, U_∞. It is important to clarify that for a rotor blade the parameter would be the relative velocity, U_r since the inflow velocity contains a tangential component due to the blade rotation.

4.1 Unsteady flow phenomena

The unsteady hydrodynamics of a tidal turbine blade strongly depends on whether the flow is attached to or separated from its surface. The latter induces moderate load oscillations, whereas the former can elicit significant fluctuations. If α exceeds the static stall angle (α_{ss}), an unsteady phenomena known as dynamic stall can manifest leading to large overshoots from the static aerodynamic forces and moments (Carr, 1988). Operating below α_{ss} is a constraint for most fixed wing aircraft. However, in the rotor environment rotational sampling of unsteady flow can produce oscillations that exceed it, which induces dynamic stall. The associated flow phenomena and methods to accurately reconstruct the unsteady aerodynamic forces and moments are ongoing areas

of research. The reduced frequency, defined in Equation 1.1 is the non-dimensional parameter used to measure the extent of unsteadiness. For a commercial scale tidal turbine the typically range is $k \in [0.1, 1]$, with waves occupying the lower limit and turbulence and blade rotation the upper limit.

4.1.1 Attached flow

In unsteady attached flow there are two key phenomena which affect the loading. The first, known as the circulatory effect, arises when vorticity is shed from the trailing edge. This causes a change in the bound circulation around the foil and a subsequent amplitude reduction and phase lag in C_L with α, compared to the quasi-steady value. The second, non-circulatory effect, also referred to as the added mass effect, is due to the time change in the pressure gradient over the foil. The combined response of the two phenomena is a hysteresis in C_L, as illustrated in Figure 4.1. This response is representative of what may occur towards the tip of a tidal turbine blade.

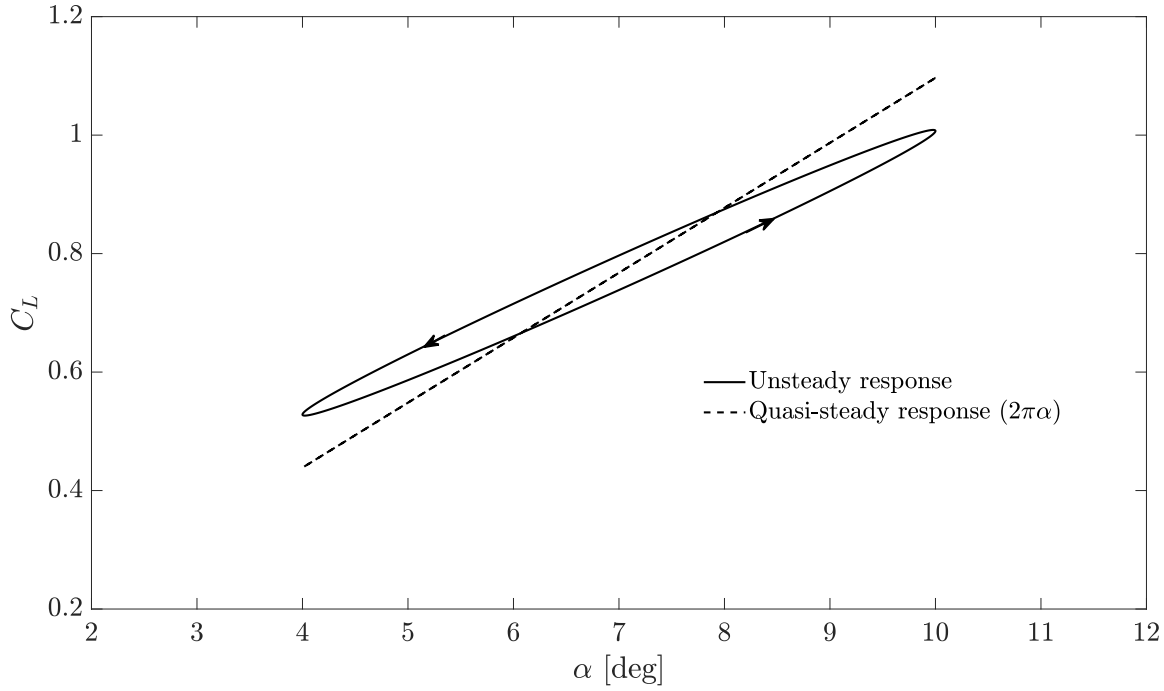

Figure 4.1: Unsteady lift coefficient in attached flow showing compared to the quasi-steady response.

4.1.2 Separated flow

As α increases an adverse pressure gradient builds up in the boundary layer. The flow reverses and separates from the surface forming a viscous layer, which moves towards the leading edge of the foil as α increases. Static stall then occurs resulting in a sudden decrease in lift and an increase in drag.

Unsteady separated flow is analogous with dynamic stall. This non-linear flow phenomena manifests when unsteady separation and stall occur resulting in a clockwise hysteresis loop of the lift response with α. There are two dynamic stall regimes: light stall and deep stall. The flow characteristics of each are illustrated in Figure 4.2 for a non-rotating foil, where (a) shows light stall and (b) shows deep stall. Light stall is characterised by trailing edge separation and boundary layer viscous-inviscid interactions, where the viscous layer is typically of the same order as the aerofoil thickness (McCroskey, 1981). Deep stall materialises at larger mean angles of attack ($\bar{\alpha}$) and is characterised by the presence of a leading edge vortex (LEV) and a viscous layer of similar order to the chord length. The unsteady loads are influenced by two distinct flow phenomena, those that are quasi-steady and those which are inherently transient (Ericsson and Reding, 1988). The quasi-steady effects can be further separated into time lag effects and boundary layer improvement effects, both reduce the adverse pressure gradient in the boundary layer, which delays separation, however, the latter also serves to increase the loads. These effects are termed quasi-steady because they can be represented by modifying the steady load coefficients for unsteady effects. Whereas the transient effects; the formation and convection of the leading edge vortex, require a separate time scale. Figure 8.5 which has been adapted from Leishman (2002), chronologically illustrates the typical stages during a deep stall event, where (a), (b) and (c) show the histories of C_L, pitching moment (C_M) and C_D with α, respectively, and (d) illustrates the key flow phenomena occurring at each stage in the cycle. At point 1 in Figure 8.5, (a) α_{ss} is exceeded and C_L increases linearly up to point 2 where separation occurs at the leading edge. At a critical angle, a LEV sheds and convects over the top surface (stage 2-3), which induces maximum lift and moment stall as shown in Figure 8.5 (a) and (b), respectively. At stage 3 lift stall occurs, which can be very abrupt compared to static stall. The flow then fully separates from the surface (stages 3-4). Then once α decreases sufficiently the flow reattaches to the surface from front to back (stage 5), and the coefficients recover to pre-stalled values. The vortex convection can produce gradients much steeper than that shown in Figure 8.5 (b), and if α

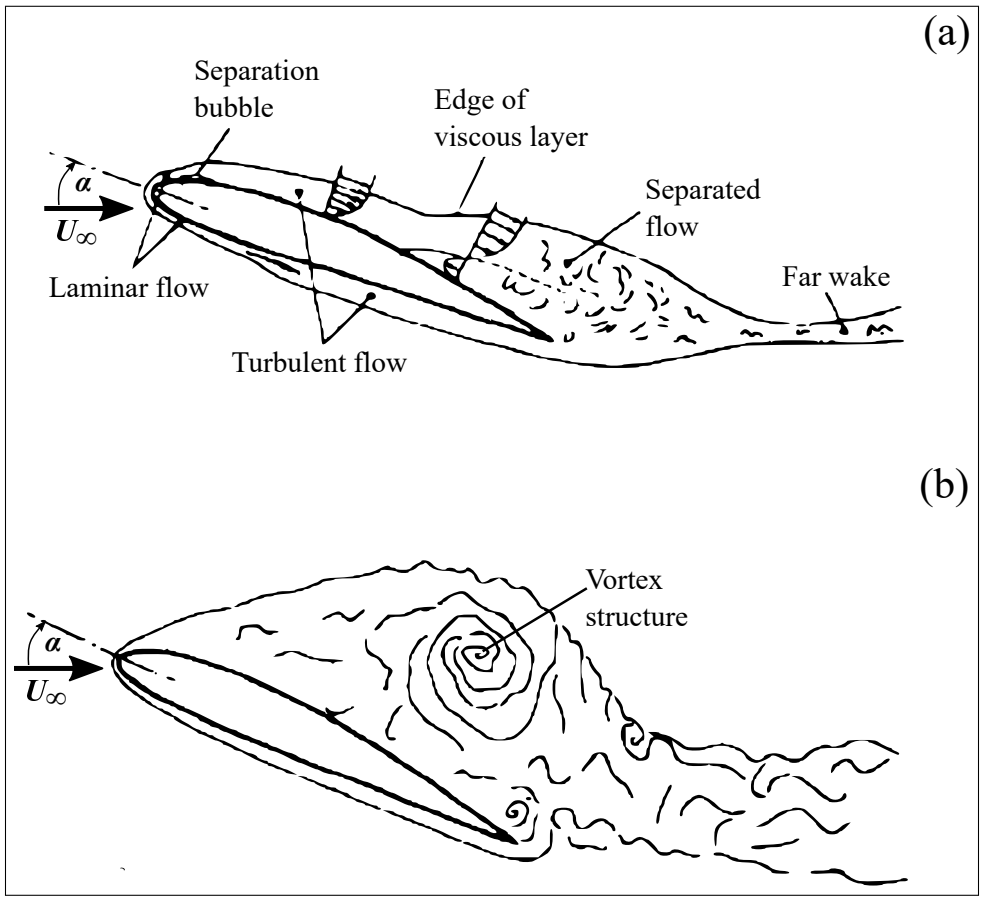

Figure 4.2: Flow characteristics of dynamic stall regimes where (a) shows a light stall event and (b) a deep stall event. Edited from McCroskey (1981)

continues increasing secondary or even tertiary vortices may shed giving rise to further load overshoots (McCroskey, 1981).

The effect of different parameters on the dynamic stall process was investigated by McCroskey (1981, 1977) who documented large effects for aerofoil geometry, reduced frequency, amplitude and mean angle of attack, and Mach number (M). The prominence of the leading edge was found to affect light stall, with separation more likely to occur at the leading edge and propagate downstream towards the trailing edge for profiles with sharper leading edges, resulting in a more concentrated vortex, whereas trailing edge separation is more likely to occur on foils with rounded leading edges. The angle of attack magnitude mostly affects the light stall regime, but limiting the amplitude in deep stall leads to no vortex shedding. The LEV was found to develop in strength for $0.15 \geq k \geq 0.05$, outside of which it was independent of k. There are significant effects for high Mach number flows such as static stall delay for M $\approx$ 0.18, shock

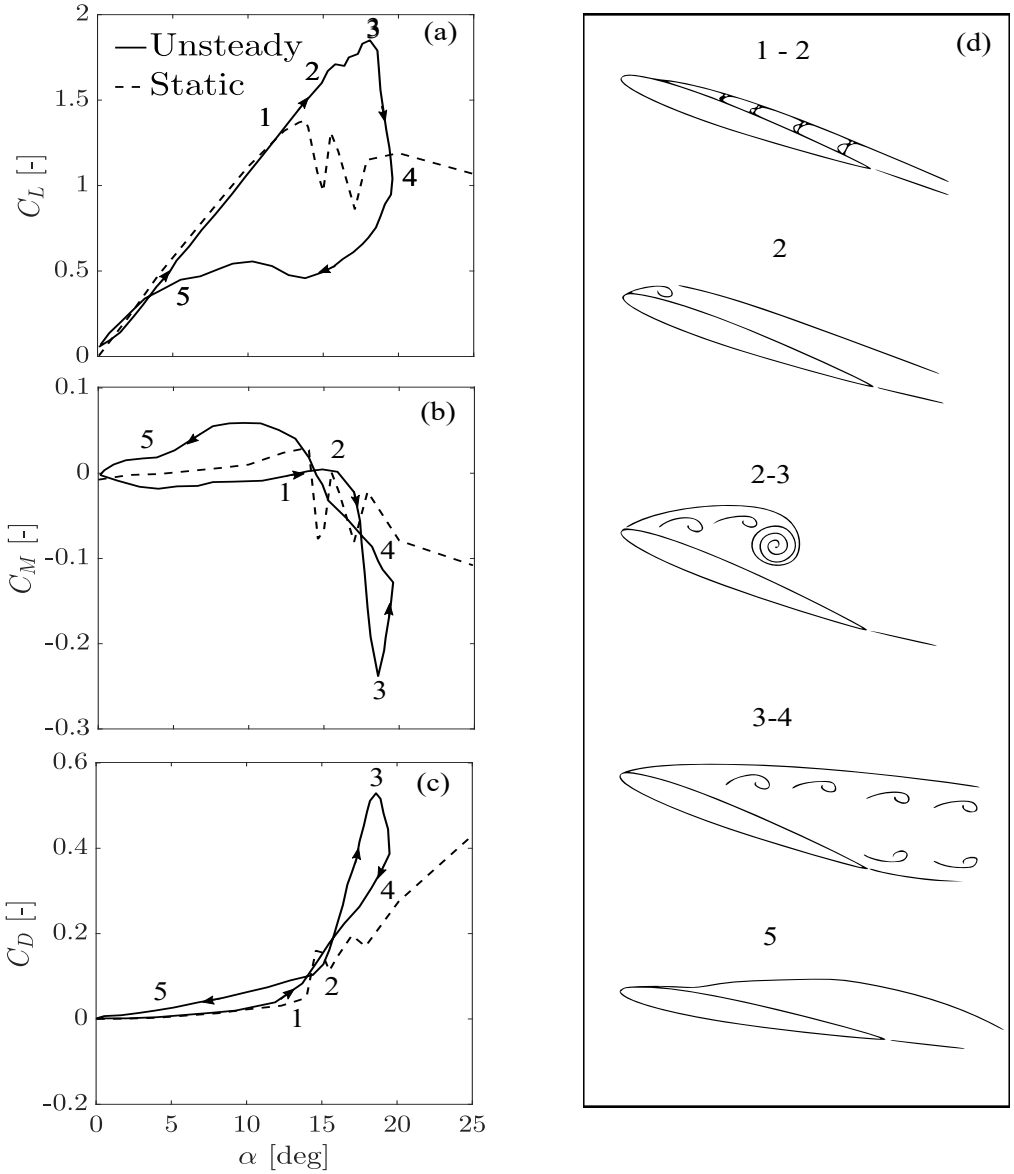

Figure 4.3: Unsteady and static load coefficient curves for each stage of a deep dynamic stall event (a) lift coefficient, (b) pitching moment coefficient, (c) drag coefficient and (d) the subsequent flow phenomena at each stage of the process. Edited from Leishman (2002)

induced stall for $M \geq 1$, and an inverse relationship with vortex strength (Corke and Thomas, 2015). Reynolds number dependence is largely unknown due to difficulties separating the effects from compressibility. However, as tidal turbines operate at lower Reynolds numbers, typically 10^6 and 10^7 for model scale and full scale, respectively, than helicopters which can attain 10^8, its sensitivity could be a factor, whereas Mach number is not.

4.2 Attached load response in the frequency-domain

The following section introduces two analytic models to determine the transient load response in the frequency domain. First to be introduced is the model of Theodorsen which gives the unsteady lift coefficient for a flat plate undergoing oscillations in angle of attack, pitch or plunge. The solution is given explicitly, but is restricted to pure harmonic forcing. Then the theory of Loewy is introduced which includes a new term that is applied to Theodorsen's theory to account for the helical wake occurring behind the rotor. These frequency-domain solutions can be used to investigate the effects of simple transient conditions on the loads since the closed form solution restricts the forcing to harmonic oscillations.

4.2.1 Theodorsen

Theodorsen (1935) solved explicitly the unsteady loads on a flat plate for small sinusoidal pitching or plunging perturbations by assuming an irrotational and incompressible fluid. Theodorsen's method was to conformally map the flow around a flat plate to a unit circle through the Joukowski transform, and determine velocity potentials separately for the non-circulatory, and circulatory shed wake contribution. The non-circulatory lift contribution is found by applying the unsteady Bernoulli equation to determine the pressure difference over the foil and then integrating along the chord. The circulatory case is non trivial since the magnitude of the circulation due to the shed vorticity is required. It is assumed that the shed vortices propagate downstream with the freestream velocity. The velocity potentials are then evaluated at the trailing edge, where by applying the Kutta condition, they are finite. This yields an integral ratio, with limits extending from the trailing edge of the foil to infinity, which is evaluated analytically by prescribing pure sinusoidal motion, allowing the integral forms to be matched to known solutions in terms of Bessel functions. The result is a complex

valued lift deficiency function, known as Theodorsen's function, where the argument is shown to be the reduced frequency. The full lift coefficient for combined pitching and heaving motion is

$$C_{L_0} = \pi b\left(\frac{\dot{\alpha}}{U_\infty} + \frac{\ddot{h}}{U_\infty^2} - \frac{ba_c\ddot{\alpha}}{U_\infty^2}\right) + 2\pi C(k)\left(\frac{\dot{h}}{U_\infty} + \alpha + b\left(\frac{1}{2} - a_c\right)\frac{\dot{\alpha}}{U_\infty}\right) \tag{4.1}$$

where dots denote partial time derivatives, $b = c/2$, $a = x_c/b$, is the non-dimensional coordinate of the pitch axis (x_c), with the origin located at the mid chord, and positive rightwards such that at the trailing edge $a_c(x_c = b) = 1$, and at the leading edge $a_c(x_c = -b) =$ -1. Thus for a pitching axis at the quarter chord, $a_c = -1/2$. $\dot{h}$ is a plunging velocity, which acts normal to the chord line. The first term in Equation 4.1 is the non-circulatory added mass component (C_L^{nc}), and the second term is the circulatory component (C_L^c). $C(k)$, which multiplies (C_L^c) is Theodorsen's complex transfer deficit function, which is defined as

$$C(k) = \frac{H_1^{(2)}(k)}{H_1^{(2)}(k) + iH_0^{(2)}(k)}, \tag{4.2}$$

where $H_v^{(2)} = J_v - iY_v$ is a Hankel function of the second kind, J_v and Y_v are Bessel functions of the first and second kind respectively; v refers to the order, which in this model takes either the value 0 or 1.

4.2.2 Loewy's returning wake

Loewy (1957) addressed the problem of a helicopter rotor in hover, where a blade section may encounter its own returning vorticity and that of neighbouring blades. The solution was to modify Theodorsen's function with a new term. This term has the effect of amplifying or attenuating C_L depending on k, the wake spacing (h_w) and the frequency ratio ($m = \omega/\Omega$) where Ω is the rotational frequency of the rotor. A tidal turbine is analogous to a helicopter rotor in hover, however, the wake convects with the mean velocity rather than the induced downwash. In Loewy's model C' is used in place of C in Equation 4.1, where

$$C'(k, W) = \frac{H_1^{(2)}(k) + 2J_1(k)W}{H_1^{(2)}(k) + iH_0^{(2)}(k) + J_1(k) + iJ_0(k)W}, \tag{4.3}$$

and Loewy's function (W) is defined as

$$W(k, h_w, m) = (e^{kh_w} e^{i2\pi m/N_b} - 1)^{-1}, \tag{4.4}$$

where N_b is the number of blades. The wake spacing parameter is

$$h_w = \frac{4\pi v_i}{\Omega N_b c}, \tag{4.5}$$

where v_i is the averaged wake convection velocity. For a helicopter rotor v_i is the average induced downwash, whereas for a tidal turbine it is the streamwise velocity. From actuator disc theory, the convective velocity at the blade is $U_0(1 - \bar{a})$, where U_0 is the mean current velocity and $\bar{a}$ is the mean axial induction factor, and in the far wake, the convective velocity is $U_0(1 - 2\bar{a})$. A simple linear average between the two velocities gives

$$v_i = U_0\Big(1 - \frac{3}{2}\bar{a}\Big). \tag{4.6}$$

4.3 Attached load response in the time-domain

Leishman (2002) suggests that k is an ambiguous parameter for rotor analyses since the blade experiences different relative velocity, and typically variation of chord length, along the span, thus k changes along the span. A more general solution is obtained in the time domain using the indicial reponse which provides the lift coefficient to any arbitrary forcing.

4.3.1 Wagner's step change in angle of attack

Wagner's theory gives lift in the time domain using the indicial response (Wagner, 1925). An indicial function is the unit step response to an input applied at $t = 0$, which is held constant thereafter. In circuit theory the indicial response is the current (in our case lift) response to a linear network, to a suddenly applied unit voltage (in our case α). As with the frequency domain solution the lift coefficient for a single step change in α consists of two terms

$$C_L(t) = \frac{\pi c}{2U_\infty}\delta(t) + 2\pi\alpha\Phi(s), \tag{4.7}$$

where the first term is the non-circular component which is a Dirac-delta function $\delta(t)$ for a unit step impluse. The second term is the circular component containing Wagner's function $\Phi(s)$, which is analogous to Theodorsen's function. The argument s is the reduced time which gives the distance travelled in semi-chords as

$$s = \frac{2}{c}\int_0^t U_\infty(t)\mathrm{d}t, \tag{4.8}$$

which for constant U_∞ gives $s = \frac{2U_\infty t}{c}$. Wagner does not give a convenient analytic solution to $\Phi(s)$. Garrick (1938) related it to Theodorsen's function, whereby

$$\Phi(s) = \frac{2}{\pi}\int_0^\infty \frac{F(k)}{k}\sin(ks)\ \mathrm{d}k, \tag{4.9}$$

where $F(k) = \mathrm{Re}\{C(k)\}$. However, it is more practical to approximate $\Phi(s)$ as an exponential decay

$$\Phi(s) = 1 - A_1 e^{-b_1 s} - A_2 e^{-b_2 s}. \tag{4.10}$$

Decay parameters for $\Phi(s)$ are shown in Table 4.1. The A1-24 is an aerofoil developed by

Table 4.1: Parameters to approximate the indicial response to angle of attack changes for different profiles

Profile	A_1	A_2	b_1	b_2	Source
Flat plate	0.165	0.335	0.0455	0.300	(Jones, 1940)
Risø A1-24	0.294	0.331	0.0664	0.327	(Hansen et al., 2004)

Risø which has a maximum thickness of 24%. Wagner's model is based on a flat plate, however, it has been shown that through curve fitting using unsteady panel methods that the indicial response can be determined for any arbitrary profile (Bergami et al., 2013).

If the indicial response is known for any arbitrary time dependent forcing (a number of different unit step changes in α), then C_L can be determined through Duhamel's integral using the principle of superposition. An excellent account of the mathematical theory involved is given by Von Karman and Biot (1940). The expression for the circular component is

$$C_L^c = 2\pi\Big(\alpha(0)\Phi(s) + \int_0^s \frac{\mathrm{d}\alpha(\sigma)}{\mathrm{d}s}\Phi(s-\sigma)\mathrm{d}\sigma\Big), \tag{4.11}$$

where σ is a dummy time variable of integration. The non-circular component is evalu-

ated outside of the Duhamel integral as long as the flow remains incompressible, which is given by Theodorsen for α oscillations as

$$C_L^{nc} = \frac{\pi c}{2U_\infty^2}\Big(\dot{\alpha}U_\infty - a_c\frac{c}{2}\ddot{\alpha}\Big), \tag{4.12}$$

For a pitching axis at the quarter chord ($a_c = -1/2$) the non-circular lift coefficient becomes

$$C_{L\ (1/4)}^{nc} = \frac{\pi c}{2U_\infty^2}\Big(\dot{\alpha}U_\infty + \frac{c}{4}\ddot{\alpha}\Big). \tag{4.13}$$

The numerical solution to C_L^c can be obtained for any arbitrary forcing using exponential approximation (Equation 4.10). The method and full solution are given in Appendix A.

4.4 Modelling dynamic stall

As described the unsteady flow phenomena associated with dynamic stall are either quasi-steady meaning they can be modelled by modifying their static counterparts, or are inherently transient, thus require temporal modelling. In the helicopter industry and more recently the wind industry semi-empirical models have been developed which couple theory with experimental correlations to predict the aerodynamic loads and moments.

4.4.1 Review of semi-empirical dynamic stall models

A variety of semi-empirical dynamic stall models exist. One of the simplest is the Boeing-Vertol (Tarzanin, 1972) method. The approach is to modify static α for dynamic effects by relating the static stall angle to the dynamic stall angle. A time-constant determined during pitching foil experiments is used to obtain an equivalent dynamic angle which corrects C_L. The ONEREA method (Tran and Petot, 1981) matches the lift curve through a set of differential equations as opposed to modelling the physical system. Which makes it easily applicable to aeroelastic modelling. A first order equation models the attached loads and a second order equation for the viscous effects. The dynamic C_L is then comprised of both parts. This model requires five empirical parameters. The dynamic lift is linearised so strictly restricts the forcing to small oscillations, however, has successfully modelled large amplitude forcings. The Beddoes-Leishman

(BL) method (Beddoes, 1978; Leishman and Beddoes, 1986, 1989) was devised for helicopter blade analysis. However, more recently a number of BL-type models (Hansen et al., 2004; Larsen et al., 2007; Gupta and Leishman, 2006; Sheng et al., 2007) have been developed for analysis of wind turbine blades. The original model comprises of three coupled physical modules. An attached flow module which uses the indicial method previously discussed but compressibility included, a dynamic flow separation model which implements two time lags on f, one for the lag in the leading-edge pressure distribution and another for the lag in the boundary layer, and lastly, a vortex lift module which temporally models the growth and passage of a LEV. The original model requires 12 empirical parameters, some of which are Mach dependant. The Øye method (Øye, 1991) is similar to the BL model in that a dynamic f is determined. The process requires knowledge of the angle at which full separation occurs. Then f across the range is determine by interpolating between C_L in fully attached and fully separated flow. A time constant describing the separation delay is used to apply a first order lag to the dynamic separation point. As with the Boeing-Vertol method attached flow or vortex shedding are neglected.

The ability of these models to successfully predict the loading for any given condition are mixed. Comparisons have found all to be lacking in some area (Larsen et al., 2007; Holierhoek et al., 2013). Larsen et al. (2007) developed a BL-type model which they compared with the original BL model the modern Risø BL-type model (Hansen et al., 2006), and the Øye, ONERA and the Boeing-Vertol models. The study concluded that only the BL models adequately reproduced the loadings under both attached and separated flow. Given that a tidal turbine blade may contain regions concurrently experiencing attached and separated flow, the ability to model both phenomena in a single algorithm is desirable. Although the Boeing-Vertol model only requires a single parameter making it attractive over the original BL model. The results of Larsen et al. (2007) suggest that the use of it by Galloway (2013) may have led to the authors misinterpreting the significance of dynamic stall for tidal turbine blades.

4.4.2 Beddoes Leishman dynamic stall model

The following description of the original BL-method is reproduced from Beddoes (1978); Leishman and Beddoes (1986, 1989) with some minor modifications to the descriptions

to clarify application to tidal turbines.

The BL model provides definitions for the normal force coefficient (C_N), chord-wise force coefficient (C_C), and C_M. The process to determine C_N is herein explained.

1. Attached flow.

   The linear response is the precursor to the onset of non-linear trailing edge separation and dynamic stall. The circulatory normal force coefficient C_N^c is determined using the indicial method described in section 4.3 with a compressibility correction. A modified time scale $s' = s(1-M^2)$ replaces s as the argument in Wagners's function $\Phi(s')$. A compressible non-circulatory C_N^{nc} coefficient is determined using piston theory, which is based on the analogy of a piston moving through a cylinder to create a compressions wave (Bisplinghoff et al., 1996, Chap. 6).

2. Leading edge separation.

   Under static conditions leading edge separation occurs at a critical pressure which corresponds to a critical normal force coefficient C_{N_1}. In the original model this is obtained from the value corresponding to either the break in C_M or C_C at stall. Due to unsteadiness there is a lag in the leading edge pressure resulting in it occurring at a higher C_N than under steady conditions, which contributes to stall delay. This can be modelled as a first order time lag

   $$\frac{\mathrm{d}C'_N}{\mathrm{d}s} = -\frac{(C'_N - C_N^p)}{T_p}, \tag{4.14}$$

   where $C_N^p = C_N^c + C_N^{nc}$ and T_p is an empirically determined non-dimensional time constant which describes the lag between the pressure distribution at the leading edge and the lift. Leishman and Beddoes (1986) determine the value of T_p to be Mach dependent, but largely independent of aerofoil geometry.

3. Trailing edge separation.

   The next step is to relate the position of the trailing edge separation point to the static normal force coefficient C_N. For this, Kirchhoff theory (Thwaites, 1960, p. 170) is integral. The separation point coordinate x is normalised by c

giving a non-dimensional separation point f, as illustrated in Figure 4.4. When the boundary layer is fully attached, $f = 1$, and when fully separated, $f = 0$.

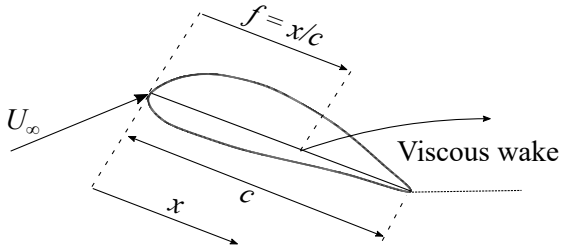

Figure 4.4: Trailing-edge separation point described by Kirchhoff flow past a flat plate.

The relationship between C_N, α and f is

$$C_N = C_{N_\alpha}(\alpha - \alpha_0)\Big(\frac{1+\sqrt{f}}{2}\Big)^2. \tag{4.15}$$

Equation 4.19 is then rearranged to solve for f, in terms of C_N using static test data. In the original model data for the NACA 0012 is used to relate f to α by a least squares fit using two exponential curves

$$f = \begin{cases} 1 - 0.3\exp((\alpha - \alpha_1)/S_1) & \alpha \leq \alpha_1 \\ \\ 0.04 + 0.66\exp((\alpha_1 - \alpha)/S_2) & \alpha > \alpha_1, \end{cases} \tag{4.16}$$

where α_1 corresponds to the value at $f = 0.7$ which is approximately the point at which static stall occurs, S_1 and S_2 are empirical coefficients describing the static stall characteristics. These parameters are all defined from the static lift data.

An effective angle of attack due to the pressure lag is defined using the lagged normal force coefficient

$$\alpha_f = \frac{C'_N}{C_{N_\alpha}}, \tag{4.17}$$

α_f is then used to determine an effective separation point f' by replacing the static value α in Equation 4.16.

The separation point is then further modified to account for the lag in boundary

layer separation due to the transient motion. A first order lag is applied to f''

$$\frac{\mathrm{d}f''}{\mathrm{d}s} = -\frac{(f'' - f')}{T_f}, \tag{4.18}$$

where T_f is a time constant describing the lag in f' due to the transient boundary layer, which is Mach dependent, however, for clarity, this is not relevant for tidal turbine applications. The non-linear normal force coefficient (C_N^f) describing trailing edge separation can then be determined using the Kirchhoff equation

$$C_N^f = C_N^c \Big(\frac{1 + \sqrt{f''}}{2} \Big)^2 + C_N^{nc}. \tag{4.19}$$

4. Vortex lift.

The final part of the model determines the lift due to the shedding and convection of a vortex over the top surface of the aerofoil. In the LB model the criterion for vortex lift is the attainment of the force coefficient value C_{N_1} which corresponds to the critical leading edge pressure value where static leading edge flow separation occurs. Thus vortex shedding occurs when

$$C_N' \geq C_{N_1}. \tag{4.20}$$

The vortex is tracked in time using a non-dimensional time parameter (τ). At the leading edge τ =0, and at the trailing edge $\tau = T_{vL}$. It has been shown for low Mach numbers that the vortex convects at approximately $U_\infty/3$, Beddoes (1978). Therefore the non-dimensional travel time $T_{vL} = c/3U_\infty$. The lift contribution due to the vortex is described as the excess build up of circulation until the critical leading edge pressure is attained. The circulation build up (C_v) is defined as the difference between the circulatory attached coefficient and the dynamic contribution given by the Kirchhoff expression:

$$C_v = C_N^c \left(1 - \Big(\frac{1 + \sqrt{f''}}{2} \Big)^2 \right). \tag{4.21}$$

The vortex contribution (C_N^v) decays exponentially in time whilst also growing

by a new increment. The first order lag is given as

$$\frac{\mathrm{d}C_N^v}{\mathrm{d}s} = -\frac{(C_N^v - C_v)}{T_v}, \tag{4.22}$$

where T_v is the vortex decay time constant, which is independent below transonic speeds. When the vortex reaches the trailing edge ($\tau = T_{vL}$), C_N^v ceases. If α continues increasing subsequent shedding can occur, which has been observed at lower values of k coupled with higher α. The shedding was found to coincide with a Strouhal number $St \approx 0.19$. An effective Strouhal number (T_{St}) can then be determined using the non-linear trailing edge separation point

$$T_{St} = \frac{2(1 - f'')}{St}. \tag{4.23}$$

A secondary vortex is then allowed to build up after non-dimensional time T_{St}.

The total nonlinear unsteady normal force coefficient is then defined as

$$C_N^u = C_N^c \left(\frac{1 + \sqrt{f''}}{2}\right)^2 + C_N^{nc} + C_N^v. \tag{4.24}$$

Chapter summary

Sources of unsteady flow for a tidal turbine and the methods to model both the unsteady flow and loads along the blade have been reviewed. A differentiation of the loads which occur in steady, unsteady attached and unsteady separated flow conditions has been given. Classical unsteady aerodynamic models have been introduced and their applicability to tidal turbine applications discussed. The Beddoes-Leishman method was identifies as the state of the art modelling technique for wind turbine engineering load models. The method was described in detail to aid the selection of an appropriate unsteady load model for tidal turbines, which is carried out in the proceeding chapter.

Chapter 5

Unsteady loads on rotor blades

To help understand how dynamic stall may occur for a tidal turbine blade this final background chapter looks at how the phenomena occurs on wind turbine blades. Firstly, experimental data from unsteady wind tunnel tests for a range of aerofoil geometries of various thicknesses are examined. Then a number of Beddoes-Leishman type dynamic stall models, developed specifically for analysing the unsteady loads on wind turbine blades are reviewed. This leads on to the description of a modern low speed dynamic stall model for wind turbine applications.

5.1 Unsteady loads on wind turbine blades

There is little evidence of dynamic stall occurring on tidal turbine blades. However, the phenomena is known to contribute to the transient loads on all types of horizontal-axis wind turbines. Early work by Butterfield et al. (1991) showed it often occurs when operating at large yaw angles, or when tower shadow, boundary shear or turbulence cause large α excursions. Thus the phenomena is likely prevalent on tidal turbine blades, too, where these conditions occur with the addition of waves. In addition some tidal power companies passively regulate power by employing stall-regulated blades, these profiles are designed to stall at high α, making them particularly susceptible to dynamic stall.

The blade profiles of installed tidal turbines are not openly available, however, to the authors knowledge at least one full scale and one model scale device employ profiles developed by NREL, these aerofoils as well as those designed by RISØ National Laboratory in Denmark and The Delft University of Technology in the Netherlands were

designed specifically for the wind industry so as to minimise sensitivity to leading edge roughness, which for a wind turbine blade is caused by bugs and debris, etc. as well as to provide a gentler stall, and to cap the maximum lift coefficient for optimum design conditions (Burton et al., 2011). They have also been found to improve the annual energy yield by up to 35% for stall-regulated and up to 20% for pitch regulated wind turbines over wind turbines which employ aeronautical aerofoils (Tangler and Somers, 1995). Since fouling is also a significant problem for tidal turbine blades it is likely that similar profiles will be used. Therefore, a good indication of how dynamic stall might occur on tidal turbine blades is to investigate tests from wind turbine blade sections.

5.1.1 Pitching oscillations on NREL foils

A series of experiments funded by NREL investigated the effects of grit roughness and pitching oscillations on the aerodynamic forces and moments on a range of aerofoils designed for wind turbines. The tests were carried out at The Ohio State University (OSU) wind tunnel. Four flows were tested with $\mathrm{Re} \in [0.75, 1.5]$ millions. For each flow the foil was oscillated about its pitch axis at three different frequencies, three mean angles and two pitch amplitudes ($\Delta\alpha$). Test results are summarised in Table 5.1 and 5.2 for eight NREL aerofoils (Reuss Ramsay et al., 1995, 1996a,b,c; Janiszewska et al., 1996; Reuss Ramsay et al., 1996d, 1998a,b). The aerofoils are arranged in ascending thickness from left to right, and represent aerofoil families for different rotor types and locations along the blade. The inboard sections are typically thicker to withstand structural loads, which comes at an aerodynamic cost for thicknesses greater than 26% (Tangler and Somers, 1995). Tidal turbine blades are likely to have even thicker blade sections (Evans et al., 2013), therefore the profiles in Table 5.1 and 5.2 with maximum thickness ($\max t$) greater than 20% are a good representation for a mid-blade section of a 1 MW rated tidal turbine. Table 5.1 lists α_{ss} and the maximum static lift coefficient for each foil, and Table 5.2 summaries the results from the dynamic tests where the peak lift coefficients, maximum percentage overshoot from the static lift coefficient $\Delta C_{L_{\%}}$ and pitching moment coefficient $\Delta C_{M_{\%}}$, are shown for $\Delta\alpha = 5.5^{\circ}$, 10°. Comparing C_L values from Table 5.1 and 5.2 we observe that for each value of $\Delta\alpha$ tested the static coefficient is exceeded for every aerofoil, with C_L greatest for $\Delta\alpha = 10^{\circ}$. The criterion for the occurrence of deep dynamic stall is the presence of a large negative pitching moment, as shown at stage 3 in Figure 8.5(b). For $\Delta\alpha = 5.5^{\circ}$, the S814 and S815 did not experience deep dynamic stall, and for the larger $\Delta\alpha = 10^{\circ}$ case, only the S815 did

	S801	S813	S825	S810	S809	S812	S814	S815
$\max t$ (%)	13.5	16	17	18	21	21	24	26
α_{ss} (°)	16.2	14.3	10.9	15.2	15.2	16.2	11.2	12.1
C_L	1.46	1.16	1.41	1.15	1.03	1.12	1.29	1.27

Table 5.1: Static properties of eight NREL aerofoils

not. The maximum percentage overshoot for both coefficients are considerable. $\Delta C_{L_{\%}}$ ranges from 53% up to 110% for the S814, and $\Delta C_{M_{\%}}$ from 137% up to 800% for the S810. These results indicate that both deep and light dynamic stall could occur on tidal

	S801	S813	S825	S810	S809	S812	S814	S815
$C_{L_{(\Delta\alpha=5.5°)}}$	1.79	1.53	1.83	1.61	1.30	1.48	1.85	1.75
$C_{L_{(\Delta\alpha=10°)}}$	2.12	2.08	2.4	1.91	1.89	1.96	2.42	2.18
$\Delta C_{L_{\%}}$ (%)	53	82	73	97	86	92	110	53
$\Delta C_{M_{\%}}$ (%)	137	340	300	800	195	350	200	137

Table 5.2: Summary of peak unsteady lift coefficient and maximum lift and moment coefficient percentage overshoots for pitch amplitudes of 5.5° and 10° for eight NREL aerofoils

turbine blades, and that for large amplitude oscillations deep dynamic stall is likely to occur. The large percentage overshoots from the static values highlight the importance of analysing the unsteady loads. Frequent excursions in α may result in fatigue loads, which if not properly accounted may result in failure before the predicted lifetime of the blade.

5.2 Modelling the unsteady loads on wind turbine blades

The NREL Phase VI experiment (briefly introduced in section 3.2) is the first and to date the only full-scale (10.1 m rotor diameter) laboratory test of a wind turbine (Hand et al., 2001). The experiment was carried out in the NASA Ames wind tunnel and tested over 1,700 configurations, producing an extensive data set to aid the development of both steady and unsteady models. A number of modellers were invited to participate in blind testing using the experimental results. In total 19 modelling tools were used

to predict the loads using 20 data sets ranging from steady to highly unsteady. The results showed high disagreement between the data and different models, even for simple steady flow conditions the bending moment predictions ranged from 25% to 175% of the predicted, and for higher wind speeds from 60% to 150% of the predicted (Simms et al., 2001). These results highlighted the difficulty of modelling the unsteady loads on wind turbine blades. Analysis of the results found shortcomings due to the different measured two-dimensional aerofoil data and a lack of correlation with the stall delay due to rotational augmentation occurring at the inboard sections (Tangler, 2002; Coton et al., 2002). With regard to unsteady model approaches Coton et al. (2002) found that models with dynamic stall implementations, in general, improved load prediction during large yaw angles. However, shortcomings in the dynamic stall models were identified, in that they were developed for helicopter blades which operate at higher Mach numbers compared to wind turbine blades.

The early use of dynamic stall models for wind turbine blades made minor modifications to the original BL model for helicopter blades. An example is the model of Pierce and Hansen (1995) which extended the range of α since a wind turbine blade may be incident to flow in the full 360° range. Gupta and Leishman (2006) took a similar approach and tuned the time constants to the NREL S809 profile which is employed on wind turbine blades. Models developed specifically for wind turbine blades are the model of Hansen et al. (2004), which has vortex lift removed, and the model of Larsen et al. (2007) which does include vortex lift, however, definitions for both the drag and the pitching moment coefficients are not provided.

A model which includes all the parameters required to model both light and deep dynamic stall is that of Sheng et al. (2008). This low speed dynamic stall model includes a number of adaptations to achieve better prediction at lower Mach numbers, making it well suited to tidal turbine blade analyses. The motivation behind the development of this model was the identification that at low Mach numbers ($M \approx 0.12$) the original BL model under predicts stall and fails to capture the reattachment process, leading to the loads being over predicted (Sheng et al., 2008). The authors identified that at low M stall onset was being predicted too early. To remedy this they identified a new stall onset parameter by establishing a relationship between the pitch rate and the critical stall onset angle. They also identified that at low M there is a wave of separated flow which convects over the foil during the reattachment process. To this end they suggest a method whereby this process could be modelled. The downside of this model is the complexity. To determine C_N and C_C 16 empirical parameters

are needed with a further six required to determine C_M. However, in a subsequent publication, (Sheng et al., 2010) the authors test the model with test data from the previously discussed Ohio State University wind tunnel experiments for a number of NREL aerofoils. With some fine tuning of the model was shown to perform well. In addition the authors conveniently provide the empirical parameters for a number of NREL aerofoils of varying thickness. As discussed on subsection 5.1.1, tidal turbine blades are likely to employ similar profiles.

5.3 Low speed dynamic stall model

In the previous section the low speed dynamic stall model of Sheng et al. (2008) was found to better predict the unsteady loads at lower speeds as opposed to the original model developed for the higher Mach speeds encountered by helicopter blades. A full description of the model is provided in this section.

5.3.1 Load response in attached flow

The attached force coefficients are computed using the method of Beddoes (1993). This indicial, Mach dependant implementation is very similar to that used in the original BL model.

5.3.2 Load response in separated flow

The first part of the non-linear solution is the load response in separated flow. To quantify this, as with the BL model, Kirchhoff theory is used, which relates the position of the trailing-edge separation point to the static normal force coefficient C_N (see Figure 4.4 and Equation 4.19). When considering NREL aerofoils the method of obtaining f is to rearrange Equation 4.19 and solve for f using static C_N wind tunnel test data Sheng et al. (2010). Then, f can be obtained for any α using a look-up table. Under unsteady conditions, boundary layer separation is delayed to a higher value of α. This lagged angle (α') is modelled as a first-order lag in the s domain, namely

$$\frac{\mathrm{d}\alpha'}{\mathrm{d}s} = -\frac{(\alpha' - \alpha)}{T_\alpha}, \tag{5.1}$$

where T_α is an empirical non-dimensional time constant describing the angle of attack delay. The solution for α' is

$$\alpha' = \alpha\Big(1 - \exp\Big(\frac{-s}{T_\alpha}\Big)\Big). \tag{5.2}$$

For arbitrary forcing the exponential decay is modelled numerically with a deficit function D_α such that

$$\alpha' = \alpha - D_\alpha. \tag{5.3}$$

Then numerically

$$D_{\alpha_j} = D_{\alpha_{j-1}} \quad \exp\Big(\frac{\delta s}{T_\alpha}\Big) + (\alpha_{_j} - \alpha_{_{j-1}}) \quad \exp\Big(\frac{\delta s}{2T_\alpha}\Big), \tag{5.4}$$

where j denotes the current time s_i and δs the time step. With α' determined, the dynamic separation point f' is found using the look-up table and replacing α as follows

$$f'(\alpha) = f(\alpha' - \delta\alpha_1), \tag{5.5}$$

where $\delta\alpha_1$ is a shift delay from the static stall angle (α_{ss}).

5.3.3 Dynamic stall onset

The critical dynamic stall onset angle is defined

$$\alpha_{cr} = \begin{cases} \alpha_{ds0}, & \dot{r} \geq \dot{r_0} \\ \alpha_{ss} + (\alpha_{ds0} - \alpha_{ss})\frac{\dot{r}}{\dot{r_0}}, & \dot{r} < \dot{r_0}, \end{cases} \tag{5.6}$$

where $\dot{r} = \dot{\alpha}c/2U_r$, is the reduced pitch rate, $\dot{r_0}$ is the value of $\dot{r}$ above which α_{cr} increases linearly and α_{ds0} is the constant dynamic stall onset angle.

The shift delay from α_{ss} is evaluated is evaluated in a similar manner

$$\Delta\alpha_1 = \begin{cases} \alpha_{ds0} - \alpha_{ss}, & \dot{r} \geq \dot{r_0} \\ (\alpha_{ds0} - \alpha_{ss})\frac{\dot{r}}{\dot{r_0}}, & \dot{r} < \dot{r_0}. \end{cases} \tag{5.7}$$

Then stall onset occurs when

$$\alpha' \geq \alpha_{cr}. \tag{5.8}$$

5.3.4 Dynamic stall load response

After the onset of dynamic stall an additional lag in the separation point occurs, as the leading edge vortex forms causing an additional load overshoot. As with α' a first-order lag is implemented to determine the dynamic separation point (f'')

$$\frac{\mathrm{d}f''}{\mathrm{d}s} = -\frac{(f'' - f')}{T_v} \tag{5.9}$$

The solution is again modelled with a deficit function (D_{ff}) which describes the lag due to the dynamic vortex as

$$f'' = f' - D_{ff}, \tag{5.10}$$

with D_{ff} solved numerically as

$$D_{ff_j} = D_{f_{j-1}} \quad \exp\left(\frac{\delta s}{T_v}\right) + (f'_j - f'_{j-1}) \quad \exp\left(\frac{\delta s}{2T_v}\right). \tag{5.11}$$

Vortex shedding follows the method of Beddoes (1993), which uses a vortex shape function (v_x) defined as follows:

$$v_x = \begin{cases} \sin^{3/2}\left(\frac{\pi\tau}{2T_v}\right), & 0 < \tau \leq T_v \\ \\ \cos^2\left(\frac{\pi(\tau - T_v)}{T_{vL}}\right), & T_v < \tau, \end{cases} \tag{5.12}$$

Subsequent vortex shedding occurs for $\tau > T_v$ until the foil starts pitching down ($\dot{r} < 0$) and v_x is set to zero. The additional lift contribution due to vortex shedding is then computed as the difference between the delayed and the static separation points multiplied by the shape function

$$C_N^v = B(f' - f)v_x, \tag{5.13}$$

where B is a constant dependent on aerofoil geometry.

5.3.5 Non-linear force coefficients

The final expression for the normal force coefficient C_N is

$$C_N^u = C_N^c\left(\frac{1+\sqrt{f''}}{2}\right)^2 + C_N^{nc} + C_N^v. \tag{5.14}$$

The expression for the chordwise force coefficient is

$$C_C^u = \zeta C_{N\alpha}(\alpha_E - \alpha_0)^2(\sqrt{f'} - E_0), \tag{5.15}$$

which has no contribution from the vortex. The parameter ζ is the leading edge pressure recovery factor provided by Leishman and Beddoes (1989) and E_0 is a constant used to reconstruct the chordwise force post stall (Sheng et al., 2010).

Chapter Summary

This chapter has shown that dynamic stall is significant for wind turbine blades, where even thick blade sections can undergo deep dynamic stall. Thus the phenomena is likely to occur for tidal turbine blades which are thicker, but operate in higher levels of unsteady flow due to waves combined with turbulence. A review of the blind tests carried out on the NREL Phase VI dataset using 19 different unsteady models revealed the difficulties predicting the loadings on wind turbine blades, even under steady flow conditions. This led on to a review of a number of Beddoes-Leishman type models for wind turbine blades. The model of Sheng et al. (2008) was found to be an excellent candidate for dynamic stall modelling on tidal turbine blades due to its representation of the dynamic stall process for low speed flows. At low Mach numbers this representation greatly improves the lift coefficient prediction compared to the original Beddoes-Leishman model.

Part II

Method

Chapter 6

Formulation of the model

A model is formulated comprising theories and modelling techniques reviewed in the preceding chapters. To recap, in Chapter 2 the unsteady flow conditions: a sheared current, turbulence and waves were reviewed. Then in Chapter 3 a review of how these conditions are compounded by induced velocities due to the presence of the rotor and the support structure is given. Following on from this it is shown that blade rotation induces rotational forces on the flow, that augments the lift and drag forces, compared to a non-rotating blade. Modelling rotational augmentation was identified as being particularly difficult. In Chapter 4 analytical models were introduced which are useful for simple harmonic analysis during attached flow, and dynamic stall models were reviewed for modelling unsteady separated flow. The Bedddoes-Leishman model was identified as the state of the art. Chapter 5 investigated how dynamic stall occurs on wind turbine blades. By analysing experimental data from pitching experiments on a number of NREL aerorfoils, it was determined that even these thick blade sections undergo deep dynamic stall, which is characterised by leading edge vortex shedding. A review of the blind tests carried out on the NREL Phase VI dataset using 19 different models revealed the difficulties encountered predicting the loadings on wind turbine blades, even under steady flow conditions. This led on to a review of a number of Beddoes-Leishman type models for wind turbine blades. The model of Sheng et al. (2008) was found to be an excellent candidate for dynamic stall modelling on tidal turbine blades due to its representation of the dynamic stall process for low speed flows. At low Mach numbers this representation greatly improves the lift coefficient prediction compared to the original Beddoes-Leishman model.

The remainder of this chapter proceeds as follows. Firstly, the parameters of the

commercial-scale tidal turbine rotor addressed in this study are given. Next the methodology to create a synthetic flow field by building up and linearly combining turbulence, channel velocity shear, tower shadow and waves are given along with corrections for a yaw misalignment. The unsteady model comprises three components: angle of attack, dynamic load coefficients and rotational augmentation, which are coupled as detailed herein.

The model presented herein assumes no radial flow along the blade span and that the blades are infinitely stiff.

6.1 Turbine specification

The dimensions of a 3-bladed, 1 MW tidal turbine representative of the Tidal Generation Ltd. DEEPGEN IV device deployed at the EMEC test site during the ReDAPT (Reliable Data Acquisition Platform for Tidal) project are used. The turbine has a gravity base, as shown in Figure 2.1 in section 2.1, where the distance from the base to the hub ($d - z_0$) is 18 m, the rotor diameter is 18 m, with a tip radius (R) of 9 m and a hub radius (R_h) of 1 m.

Three dimensional views of the blade are shown in Figure 6.1. Here (a) shows the leading edge of the foil and the increase in thickness from the tip to the hub, (b) presents the pressure surface view which illustrates how the chord increases towards the hub, then tapers back in to form a cylinder at the root, and (c) shows the trailing edge where the geometrical twist of the blade can be seen. The distributions of c and β_g along the blade span, which have been taken from Gretton (2010), are shown in Figure 6.2.

The original blade profile has a non-uniform thickness and comprises NACA 63-4XX geometries, where XX denotes the maximum camber thickness of each section in relation to c. To simplify it is assumed that all sections have uniform thickness comprising of the NACA 63-418, and to aid the modelling of dynamic stall the NACA profile is replaced with a NREL profile since a large database of empirical dynamic stall parameters are available for a series of NREL aerofoils (Sheng et al., 2010). A suitable profile was selected by matching the maximum power coefficient (C_P) at the optimum tip-speed ratio. The power coefficient is defined as

$$C_P = \frac{P}{\frac{1}{2}\rho\langle U_x^3\rangle A}, \tag{6.1}$$

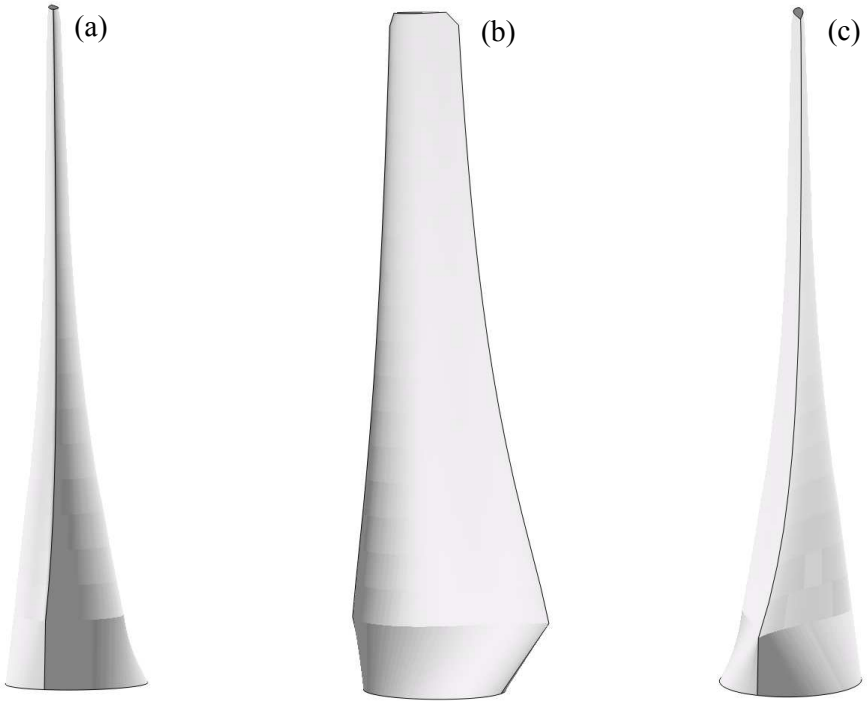

Figure 6.1: Blade profile views of (a) the leading edge (b) the pressure surface and (c) the trailing edge.

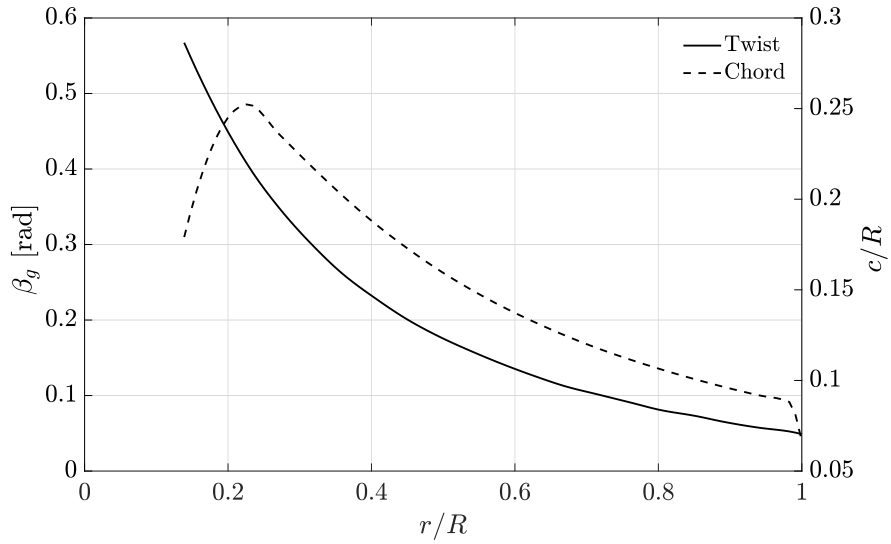

Figure 6.2: Blade chord and twist radial distribution (from Gretton (2010)).

where A is the area swept by the rotor and the angle brackets indicate the double

average over Δt and A. The rotor power P for a turbine with three blades is defined as

$$P = \Omega \sum_{j=1}^{3} Q_j, \tag{6.2}$$

where j denotes the blade and Q_j is the torque on blade j, which is

$$Q_j = \int_{R_h}^{R} F_{Tan} \cdot r \cdot \mathrm{d}r. \tag{6.3}$$

In this analysis $\langle U_x^3 \rangle = 2.7\ \mathrm{ms}^{-1}$, which is the velocity at which rated power is achieved for the DEEPGEN IV device. As shown in Figure 6.3 the NREL S814 profile which has a thickness of 24% provides a similar C_L with α curve to the NACA 63-418 profile. The stall characteristics are slightly different due to geometry differences, as illustrated in Figure 6.4. The S814 is clearly thicker, which is desirable for inboard blade sections that incur large α fluctuations. This profile has been employed on the tank scale tidal turbine rotors of both Milne et al. (2013a) and Barltrop et al. (2007) indicating that it is suitable for tidal turbine application.

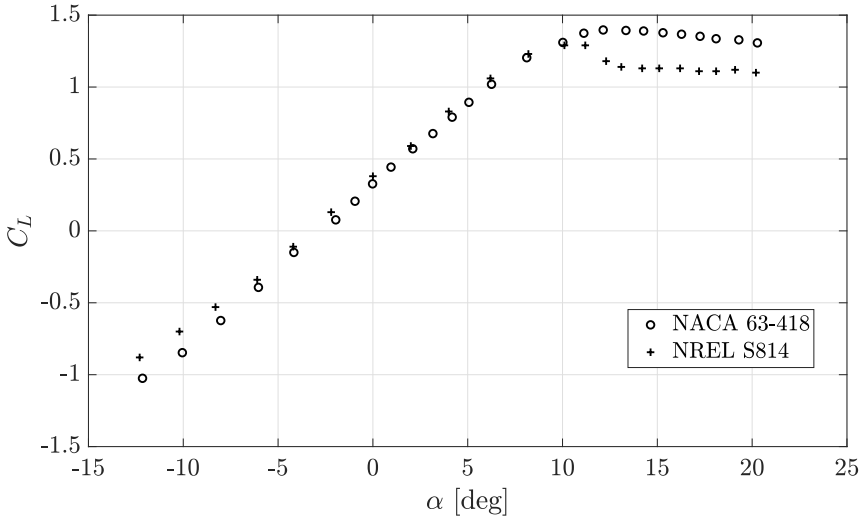

Figure 6.3: Lift coefficient with angle of attack for the NACA 63-418 and the NREL S814 geometries.

Power coefficients for $\lambda \in [0, 10]$, are shown for both profiles in Figure 6.5. A $\max C_P \approx 0.47$ occurs at $\lambda = 4.5$ for both geometries. Thus, the NREL S814 profile will be used throughout. The static C_L and C_D data used to analyse the NACA 63-418 and NREL S814 have been obtained from Janiszewska et al. (1996) and (Abbott and

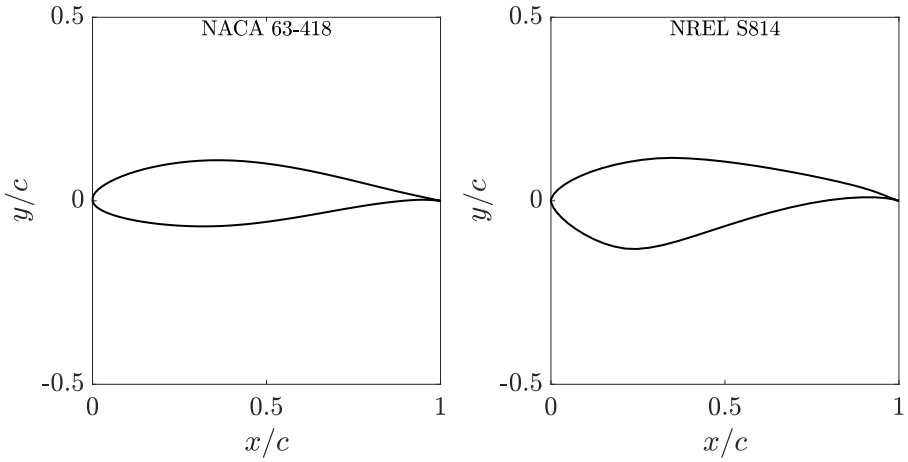

Figure 6.4: Comparison of the NACA 63-418 and the NREL S814 geometries.

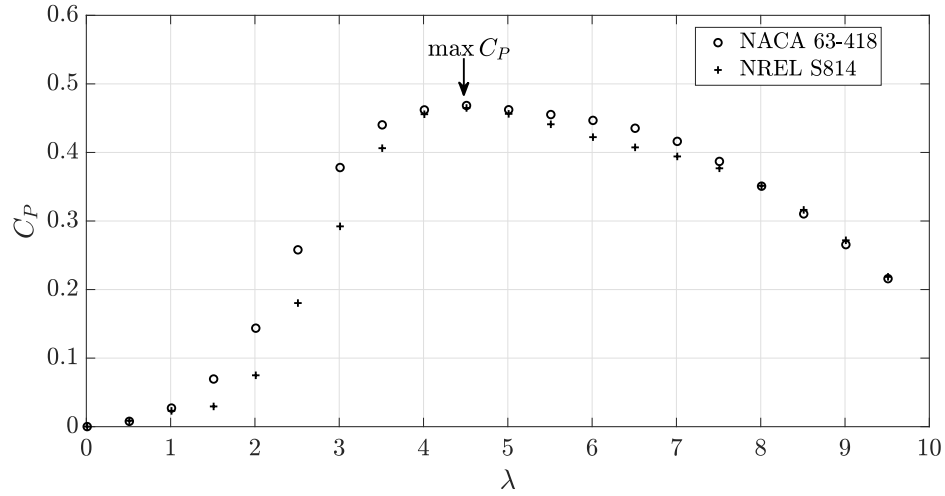

Figure 6.5: Power coefficient with tip-speed ratio relationship for the NACA 63-418 and the NREL S814 geometries.

Albert Edward Von Doenhoff, 1959), respectively, both of which were measured in a uniform flow at a Reynolds numbers in the order of 10^6.

6.2 Unsteady inflow

In this section the method to generate an unsteady time series is described using the theory introduced in chapter 2. This method is used in chapter 8 to investigate a range of unsteady flow conditions on the local and global blade loads, whereas in chapter 9 a measured time series will be considered.

Turbulence is synthesised using the von Kármán spectral model to generate a velocity spectrum. To date spatial correlations have not been recorded for tidal channel turbulence. Therefore, it is assumed that turbulence is spatially uniform and referenced to the current velocity at the hub: $U_0 = \sqrt[3]{\langle U_x^3 \rangle}$. A comparison of the streamwise velocity spectra measured at EMEC with that predicted using the von Kármén spectrum is carried out. Measurements were recorded during the ReDAPT campaign, using a Single-Beam Acoustic Doppler Profiler at a sample rate of 4 Hz, full details of the data acquisition method are described in Sellar et al. (2018). The flow sample was measured during flood tide with $H_s < 0.8$ m. The location of the measurements: $x = -20$ m, $y = 0$ m and $z = -27$ m, corresponds to hub height. The measured flow statistics are: $U_0 = 2.74$ ms^{-1}, $I_x = 9\%$ and $L_x = 26.5$ m. Observing Figure 6.6, the modelled spectrum fits the measured data very well. Doppler noise from the instrument distorts the measurements from about 0.5 Hz, without this the profile would continue along the 5/3 slope or steeper.

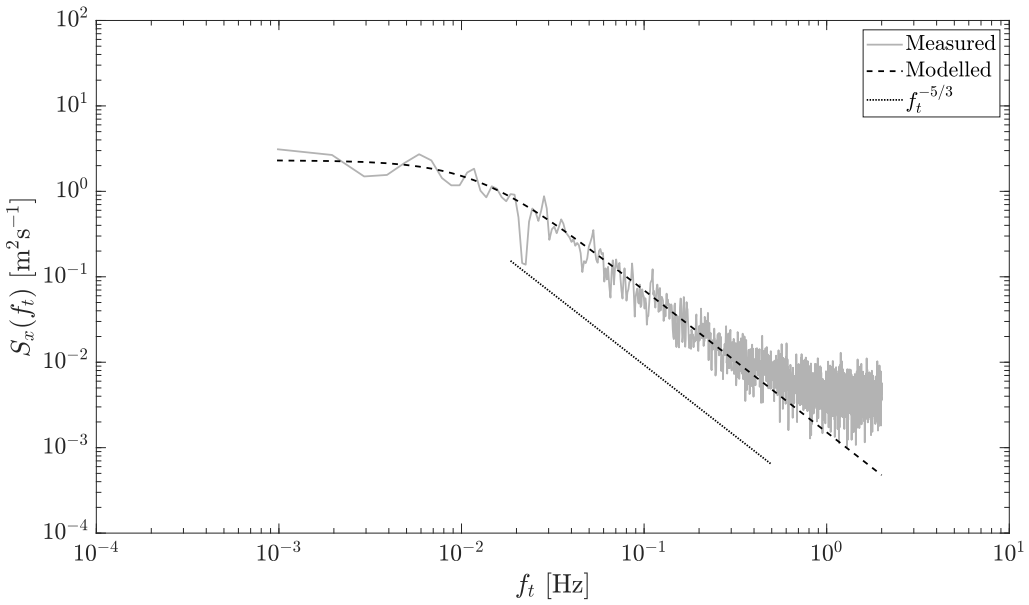

Figure 6.6: Comparison of the measured and modelled streamwise velocity spectrum from the European Marine Energy Center in Orkney.

The Shinazuka method (Shinozuka, 1972) is used to create a velocity time series using uniformly distributed random phases between components. A representative time series is shown in Figure 6.7 which was been generated over 50 blade rotations with $\lambda = 4.5$, $I_x = 0.1$, $L_x = 10$ m and $U_0 = 2.7$ ms^{-1}. The recovered $I_x = 0.0975$, which is a 2.5% difference from the input. The $R(\hat{t})$ decay is shown in Figure 6.8, from which

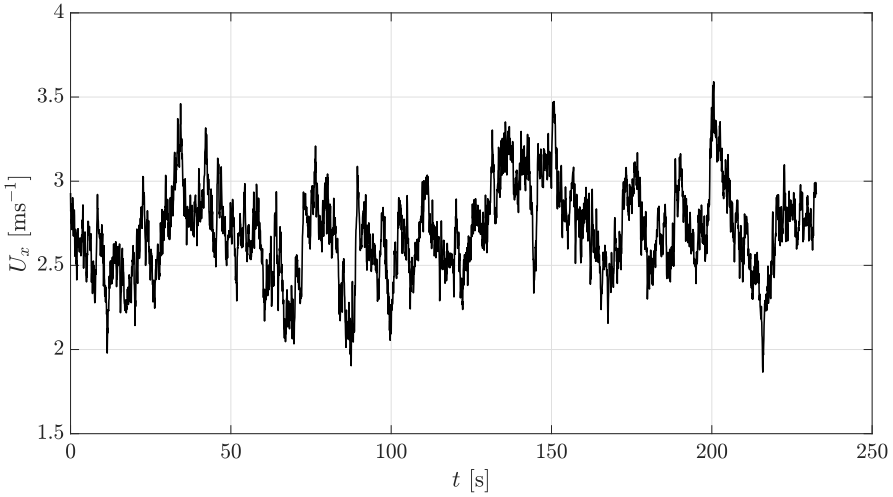

Figure 6.7: Turbulent velocity time series generated using the von Kármán spectrum.

the integral time scale is 3.4 s resulting in L_x= 9.1 m, which is a 9% difference from the input value used to generate the von Kármán spectrum, which concurs with the difference reported by Mullings and Stallard (2018).

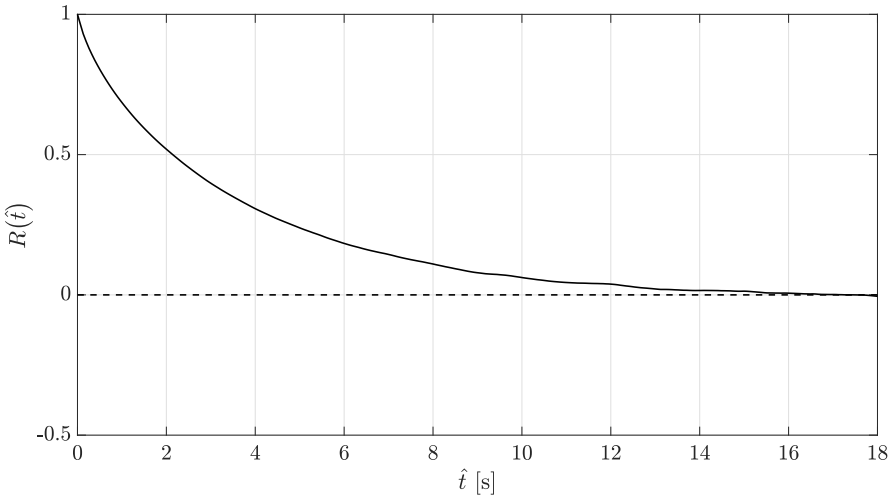

Figure 6.8: Correlation coefficient with time lag for a time series generated using the von Kármán spectrum.

Shear, turbulence and tower shadow, as described in chapter 2, are superimposed in respective order to give a linearly combined velocity profile, which is then combined with the wave velocity profile. In cylindrical coordinates the combined tangential and

axial (U_X) velocity components are

$$U_\psi = (W_z + u'_z)\cos(\psi - \theta_b) + (V_y + u'_y)\sin(\psi - \theta_b) + \Omega r, \tag{6.4}$$

and

$$U_X = V_x + W_x, \tag{6.5}$$

respectively, where θ_b is the phase lag from the leading blade. The z-coordinate of a blade section is $z_0 + r\sin(\psi - \theta_b)$ and the y-coordinate is $r\cos(\psi - \theta_b)$.

6.3 Angle of attack time history

With the flow velocity time series computed the instantaneous angle of attack time is determined using the BEM implementation outlined in section 3.3. In all cases the static C_L and C_D values are corrected for rotational augmentation using the Lindenburg model explained in section 3.2. However, since the NREL phase VI results show a reduction in the drag coefficient at the outer sections of the blade Hand et al. (2001). The present model will assume for $r \geq 0.8R$, that $C_D^{rot} = C_D$ to avoid any over-prediction.

BEM theory is strictly steady, to circumvent this, the instantaneous, local tip-speed ratio ($\lambda'_r = U_\psi/U_X$) replaces λ_r in the residual equation (Equation 3.19), and the induction factors are solved at every time step over a rotational period (T_r). With the induction factors determined for each time step, these are time averaged over the previous T_r. The time averaged solution $\langle a \rangle$ at time t_i is

$$\langle a \rangle = \frac{1}{T_r}\int_{t_i - T_r}^{t_i} a(t)\,\mathrm{d}t, \tag{6.6}$$

likewise, the time average of $\langle a' \rangle$ follows the exact same procedure.

The effect of yaw is incorporated into the axial induction factor using the uncoupled approach described by Ning et al. (2015) using Equation 3.18. In the present model a post correction occurs on a after the time averaging process. The tangential induction factor remains unchanged.

Lastly, α time histories are calculated for each r as follows

$$\alpha(t) = \tan^{-1}\left(\frac{U_x(t)(1 - a(t))}{U_\psi(t)(1 + a'(t))}\right) - \beta. \tag{6.7}$$

6.4 Dynamic load coefficients

The total unsteady load response comprises of three elements: attached flow, trailing edge separation and leading edge vortex shedding. The non-linear load coefficients are determined using the dynamic stall model of Sheng et al. (2008) as detailed in section 5.3, with modifications for attached flow, drag and rotational augmentation which are now discussed.

6.4.1 Load response in attached flow

Sheng et al. (2008) determine the linear solution using a method developed by Beddoes (1993), which considers compressibility effects. However, for a tidal turbine the maximum Mach number is approximately 0.03, which occurs at the blade tip and is an order of magnitude less than the compressible range. Thus the attached loads are determined using the incompressible time domain solution of Wagner (1925) (see subsection 4.3.1). The C_L^c time history for a number of arbitrary unit step changes in α is determined by superposition through the Duhamel integral as follows:

$$C_L^c = 2\pi\alpha_E, \tag{6.8}$$

where the equivalent angle of attack that lags the physical α is

$$\alpha_E = \alpha(0)\Phi(s) + \int_0^s \frac{\mathrm{d}\alpha(\sigma)}{\mathrm{d}s}\Phi(s-\sigma)\mathrm{d}\sigma, \tag{6.9}$$

where $\Phi(s)$ is computed using Equation 4.10 with the indicial response parameters for the Risø A1-24 profile shown in Table 4.1. The non-circulatory coefficient C_L^{nc} is treated outside of the Duhamel integral. For this term, the following approximation given by Hansen et al. (2004) is used:

$$C_L^{nc} = \frac{\pi c\dot{\alpha}}{2U_r}. \tag{6.10}$$

Then the full unsteady lift coefficient in attached flow is

$$C_L^p = C_L^c + C_L^{nc}. \tag{6.11}$$

For an arbitrary α time-variation, (Equation 6.8) and (Equation 6.10) are determined numerically. The numerical solution can be found in Appendix A.

6.4.2 Non-linear lift and drag coefficients

The unsteady force coefficients C_N^u and C_C^u are computed as described in section 5.3. The lift coefficient is then defined as

$$C_L^u = C_N^u \cos(\alpha) + C_C^u \sin(\alpha). \tag{6.12}$$

Sheng et al. (2008) define the drag coefficient as

$$C_D^u = C_N^u \sin(\alpha) - C_C^u \cos(\alpha) + C_{D_0}, \tag{6.13}$$

where C_{D_0} is the drag coefficient at α_0, however, this definition does not bound C_D^u to the static drag curve in steady conditions. Therefore, the definition provided by Hansen et al. (2006) is used, which is expressed as three terms

$$C_D^u = C_D^{st} + C_D^{ind} + C_D^{vis}, \tag{6.14}$$

where

$$C_D^{ind} = C_L^u(\alpha - \alpha_E), \tag{6.15}$$

and

$$C_D^{vis} = (C_D^{st} - C_{D0})\Big(\frac{1+\sqrt{f''}}{2}\Big)^2 - \Big(\frac{1+\sqrt{f(\alpha_E)}}{2}\Big)^2, \tag{6.16}$$

where C_D^{st} is the static drag coefficient determined from wind tunnel test data. The three terms on the right hand side of (6.14) are the static, induced and viscous components, respectively. C_D^{vis} is zero when the flow remains attached since $f'' = f(\alpha_E)$, and under near steady conditions $C_D^{ind} \to 0$ as $\alpha_E \to \alpha$.

The empirical parameters for the NREL S814 are shown in Table 6.1. The empirical constants are taken from Sheng et al. (2010), with slight modifications made using the Ohio State University (OSU) wind tunnel test data (Janiszewska et al., 1996). The dynamic constants are shown in bold. The rotational parameters: $b_3 = 0.5$ and $b_4 = 0.5$, are tuned to the NREL S809 profile using the NREL Phase VI test data (as discussed in section 3.2), since no empirical data is available for any other profiles, these are used.

Table 6.1: Table of empirical parameters for the NREL S814.

$\alpha_{\mathbf{ds0}}$	0.2426
α_{ss}	0.2007
α_0	-0.0573
C_{D0}	0.01
$C_{N\alpha}$	6.267
E_0	0.1
ζ	1
$\dot{r_0}$	0
$\mathbf{T}_\alpha$	6.33
$\mathbf{T_v}$	4
$\mathbf{T_{vL}}$	6
B	0.5
b_3	0.5
b_4	0.5

6.5 Rotational augmentation correction

For a rotor blade the combination of blade rotation, which induces a centrifugal and Coriolis force on the flow, with dynamic stall can produce very large lift amplitudes compared to the non-rotational case (Guntur et al., 2016). This recent study by Guntur et al. (2016) used the NREL Phase VI data, an in-house Navier-Stokes solver and dynamic stall models to investigate modelling dynamic stall on blades undergoing rotational augmentation. The authors used the steady rotational data for the NREL S809 profile with their dynamic stall model to give reasonable prediction. These results show that the non-rotational dynamic stall models should be able to reasonably predict the rotational hydrodynamics when combined with a suitable rotational augmentation model.

The Lindenburg model is well-suited to combination with the Beddoes-Leishman dynamic stall modelling approach since both use the separation point parameter f. To this end, Lindenburg's model is combined with the low speed dynamic stall implementation to superimpose the effect of rotation on both C_L^u and C_D^u. To the best of my knowledge combination of these two models has not been attempted before. The correction proceeds by first modifying f such that it is also a function of r and then by applying the rotational angle shift, $\delta\alpha^{rot}$ to the static stall angle and the critical dynamic stall angle. These are then used in the dynamic stall model. The steps are as

follows:

1. Compute C_N^{rot} for each section using Equation 3.5 to Equation 3.9.
2. Replace C_N with C_N^{rot} in Equation 4.19 to determine f^{rot} for each r.
3. Replace f in Equation 5.5 and Equation 5.13 with f^{rot}.
4. Angle shift given by Equation 3.6 is applied to the static stall angle: $\alpha_{ss}^{rot} = \alpha_{ss} + \delta\alpha^{rot}$.
5. Angle shift given by Equation 3.6 is also applied to the critical dynamic stall onset angle: $\alpha_{ds0}^{rot} = \alpha_{ds0} + \delta\alpha^{rot}$.
6. Replace f, α_{ss} and α_{ds0} with f^{rot}, α_{ss}^{rot} and α_{ds0}^{rot} in the dynamic stall model as described in section 5.3 and section 6.4 .

6.6 Coupled model

The unsteady, rotational load coefficients are coupled with the BEM model to investigate the effect on the induction factors; something which has not previously been reported in the literature.

Due to hysteresis and non-linearities, $C_L^u(t)$ and $C_D^u(t)$ are non-unique for a given α. This is a problem for the BEM model which requires predefined values of C_L and C_D for a given α. To accomodate this, $C_L^u(t)$ and $C_D^u(t)$ are collected from the previous time steps over the period of revolution, sorted into α bins, and the mean value calculated for each bin. A smoothing spline is then applied to the points to achieve a continuous set of values. After this the Viterna-Corrigan deep stall extrapolation Viterna and Corrigan (1981) is applied. This extends the coefficients α range between $-\pi$ and π, which is a numerical requirement of the BEM model. The look-up tables, containing unique values of $C_L^u(\alpha)$ and $C_D^u(\alpha)$ for each r are then passed to the BEM model. New values of a and a' are determined and fed back into the numerical model, coupling the unsteady response with the induction factors. The solution is iterated until the sum of the squares error over r is $L_2 \leq 10^{-6}$, where

$$L_2 = \sum_{r=R_h}^{R} (\delta a)^2 , \tag{6.17}$$

here δa is the difference between the current and the previous value.

A flow diagram is shown in Figure 6.9 which illustrates the key stages and logic of the numerical model. The initial conditions first determine U_x and U_ψ as previously described, then solve a and a' for the first rotation using the static coefficients. After this α and the subsequent unsteady, rotational coefficients are calculated. The coefficients are then transformed into $C_L^u(\alpha)$ and $C_D^u(\alpha)$, enabling the BEM model to solve the new induction factors at each time step, which are then time averaged and fed back into the coupled model until convergence is satisfied. After which time increases by an increment δt, and the converged solution becomes the new initial condition. The process continues until the time history is complete.

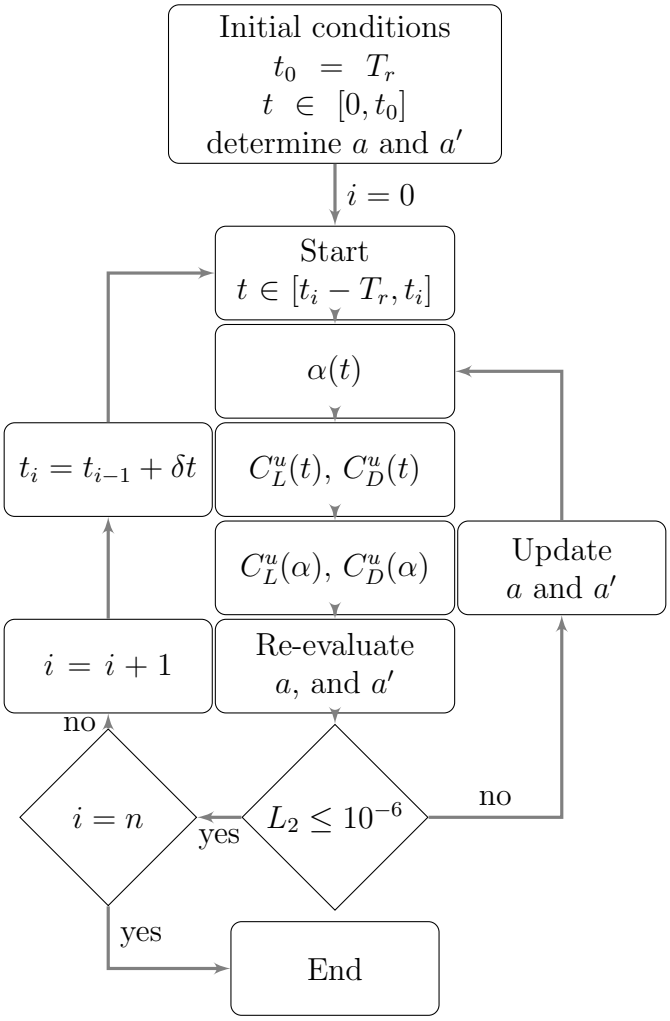

Figure 6.9: Process diagram of the coupled model.

6.7 Code implementation

The code is written in MATLAB and is freely available for use and can be downloaded from the author's GitHub repository (Scarlett and Viola, 2017). The code is modular and comprises of multiple functions which are called from a run script. All functions have been developed by the author other than"zero.m" which is the Brent algorithm (Brent and Burkardt, 2002) used to solve the root of the BEM residual equation,"simps.m" which applies Simpson's rule to numerical integration (Garcia, 2013) which is used to integrate the distributed blade loads and "wavenumber.m" which solves the linear dispersion equation with a current (Sanchex, 2013) which is used to model waves. The code has been vectorised such that the loads on a full blade are evaluated concurrently. The BEM implementation cannot be vectorised since it relies on the Brent algorithm. For this reason further optimisation was carried out using the MATLAB parallelisation toolbox to run concurrent simulations on multiple CPU's.

6.8 Computational costs

The computational cost of the model is examined for three convergence parameters after which the performance of the coupled model is evaluated by comparing the prediction with a steady BEM prediction and a quasi-steady BEM prediction.

A five minute flow sample is simulated with waves; $H_s = 5$ m, $T_a = 10$ s, $z_0 = -27$ m, turbulence, $I_x = 0.1$, $L_x = 10$ m, $R_t = 1$, and a sheared current; $U_0 = 2.7$ ms^{-1}, $\nu = 1/7$. In total 65 rotations are simulated with δt corresponding to a 5° rotation, which gives 4680 time steps. Referring to the process diagram shown in Figure 6.9, a compute cycle can be defined as the number of times which to convergence parameter is evaluated. In Figure 6.10, the compute cycle counts are shown for three convergence criteria; $L_2 \leq 10^{-6}$, $L_2 \leq 10^{-2}$ and $L_2 \leq 5 \times 10^{-2}$, which correspond to errors of 0.0001%, 1% and 5%, respectively. The simulations were carried out on a desktop computer with 12, 3.0 GHz CPU cores. The simulation times were approximately 15 hours, 6 hours and 3 hours, respectively.

The performance of the coupled model is compared with a steady BEM model, where the inflow velocity is a constant 2.7 ms^{-1} over the entire rotor plane and with a quasi-steady method, where the inflow is unsteady but unsteady load phenomena are ignored. The induction factors for three different tip-speed ratios are computed; λ =4.5, 4.0, 3.5. The time step corresponds to a 5° increment in the azimuthal position

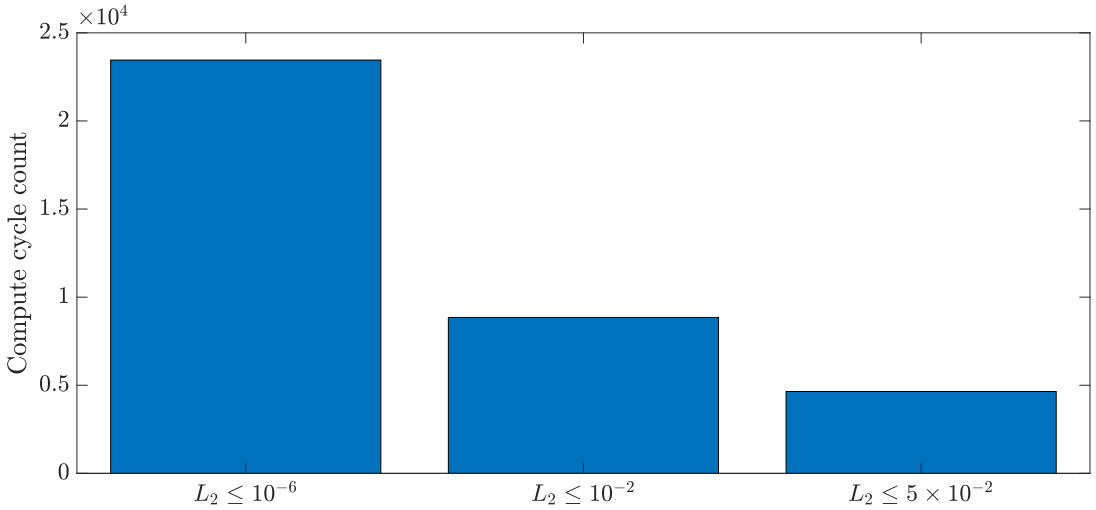

Figure 6.10: Compute cycle count from coupled model for three convergence criteria.

and for the unsteady cases convergence is on $L_2 \leq 10^{-6}$. The results, presented in Figure 6.11, show there is no discernible difference between the unsteady and the quasi-steady predictions. However, there is a moderate difference compared to the steady prediction. The maximum percentage difference between the unsteady and quasi-steady for $\bar{a}$ is 0.6% and for $\bar{a'}$ is 5.4%, both for the $\lambda = 3.5$ case. The unsteady simulation took approximately 15 hours compared to 3 minutes for the quasi-steady simulation. This gain in accuracy, arguable comes at too high a computational cost. Conversely, the maximum percentage difference between the quasi-steady and steady prediction are 8.6% and 25.7% for $\bar{a}$ and $\bar{a'}$, respectively, again both for the $\lambda = 3.5$ case. These results indicate that using the instantaneous flow is more important than the unsteady load phenomena for the BEM algorithm.

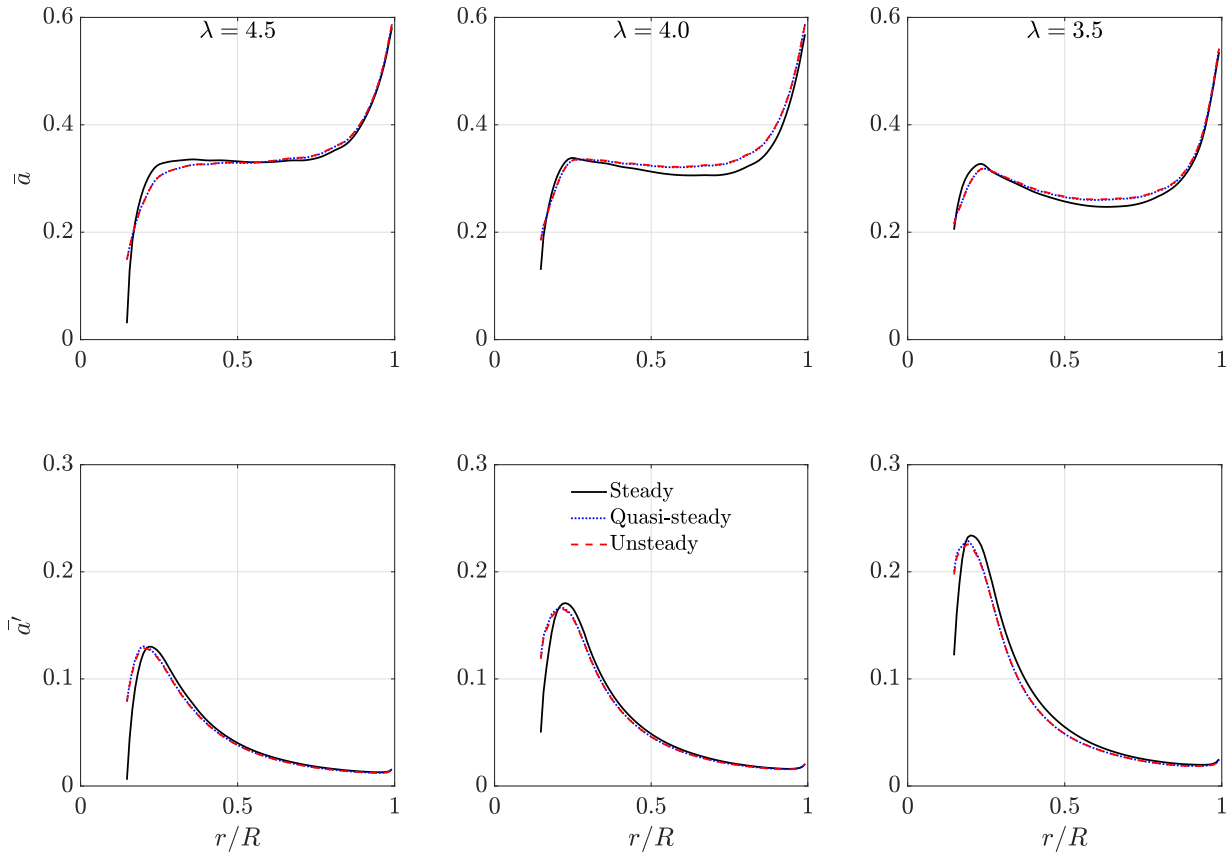

Figure 6.11: Time averaged induction factor predictions at each blade section, compared with a steady, quasi-steady and coupled unsteady blade-element momentum implementation.

Chapter 7

Evaluation of the model

In this chapter the model is validated. Firstly the individual key components of the numerical model are validated. The blade-element momentum model is validated against the AeroDyn by predicting the power and thrust coefficients for a range of tip-speed ratios. The dynamic stall model is then used to predict the lift coefficient for a pitching (non-rotating) aerofoil using experimental data. Following on from this a qualitative validation is carried out for the rotating case by inspecting the difference in the lift coefficient hysteresis for the non-rotating and rotating cases and comparing these with data for a different aerofoil profile. After validating these individual components the full model is used to predict the root bending moment for a tank scale turbine undergoing wave loading.

7.1 Blade-element momentum validation

First the BEM implementation is used to predict values of C_P and thrust (C_T) coefficients, respectively, for a range of tip-speed ratios ($\lambda = \Omega R/U_0$) $\in [0.5, 8]$, which are compared to those predicted using AeroDyn, an opensource aerodynamic software developed by NREL, which also uses the theoretical implementation of Ning et al. (2015). The turbine (described in section 6.1) employs uniform thickness NREL S814 profiles at each section, the flow is steady with a current velocity of 2.77 ms^{-1}, the rotor is normal to the flow and $\beta_p = 0$. The results are shown in Figures 7.1(a) and 7.1(b) for C_P and C_T, respectively. The predicted values of C_P are in very good agreement with that of AeroDyn with both models predicting a similar maximum C_P occurring at $\lambda = 4.5$. From $\lambda = 5$ onwards, C_P is slightly under predicted compared to AeroDyn, although

both have similarly decreasing slopes. The predicted values of C_T agree across the full range, apart from a slight over prediction for $\lambda \in [4, 5]$. This validation is sufficient for the analysis carried out in chapter 8 and chapter 9 since values of $\lambda = 4.5$ or less are mostly considered.

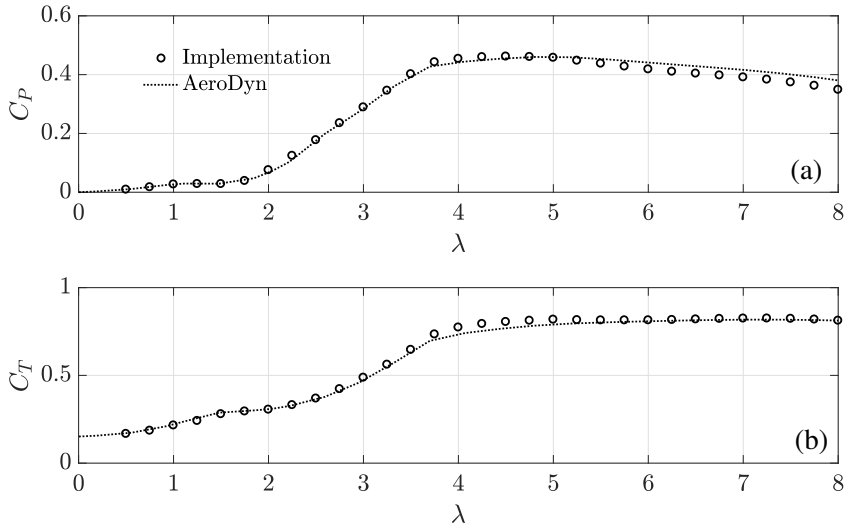

Figure 7.1: Power (a) and thrust (b) coefficient performance curves for a turbine operating in steady conditions.

7.2 Dynamic stall validation

Next, the predictive capabilities of the dynamic stall model are tested. The relationship between C_L and α for the S814 aerofoil is shown in Figure 7.2 for a number of cases. Empirical values from the OSU wind tunnel tests are shown for the measured static and dynamic cases (Janiszewska et al., 1996). Predicted values are shown for the dynamic case, and for both the static and dynamic cases with the effect of rotational augmentation. The forcing is $\alpha = 13.8° + 10.75° \sin(\omega t)$, $k = \ 0.091$ and for the rotational case, $r = 0.47R$. The predicted values of C_L when pitching positively from around 3° to 18° agree with the measured dynamic data, and the shape of the load hysteresis matches qualitatively.

The model predicts the increase in lift at around 18° caused by vortex shedding, as well as the partial recovery from stall at around 23° due to a secondary vortex being shed. During the return from stall, when α is decreasing the model over predicts C_L. Prediction in this region could be improved by using an additional return from stall

model (Sheng et al., 2008). However, the accuracy is satisfactory to address the research questions in this thesis, and is therefore, not included.

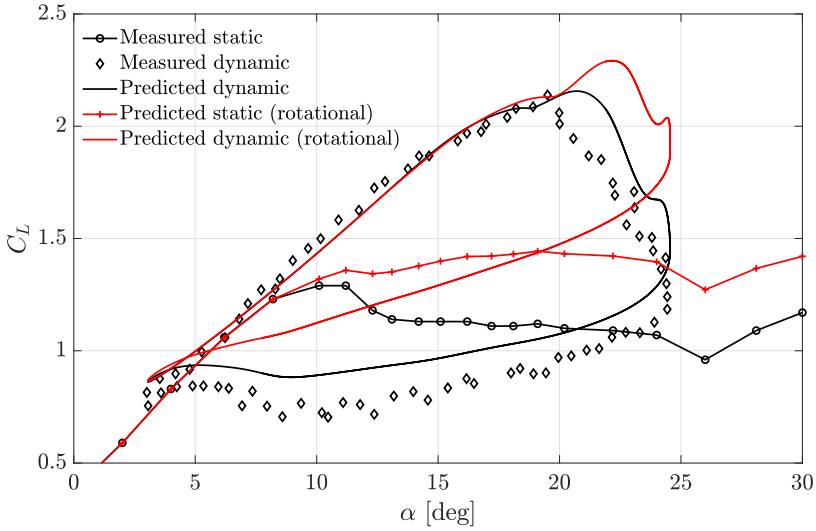

Figure 7.2: Lift coefficient as a function of angle of attack for static and dynamic conditions, with and without the effect of rotation. Comparison is made with measured data from Janiszewska et al. (1996)

The modification made to combine the effects of dynamic stall with rotational augmentation cannot easily be validated since no dynamic rotational data exists for the NREL S814. However, a qualitative comparison can be made using the NREL Phase VI experimental data for the S809. Figure 7.3 which has been reproduced from Guntur et al. (2016) shows the lift coefficient curve for a NREL S809 foil while dynamically pitching for both non-rotational and rotational cases. Here $k = 0.1$ and the location along the blade is $0.47R$. The difference between the non-rotational and rotational curves for the S809 matches qualitatively with the difference between modelled dynamic and dynamic rotational curves for the S814 shown in Figure 7.2. However, while pitching up the non-rotational and rotational curves are not aligned as would be expected. In this region the linear lift curve of the S809 for both the rotational and rotational static curves produce $C_L(10°) = 1$ (see Breton et al., 2008, Figure 3). During dynamic stall C_L follows the linear static lift curve, and then exceeds it. Yet, the non-rotational data shows $C_L(10°) = 0.9$. There are two possible explainations for the discrepancy; firstly that there is ambiguaty in the α values. Guntur et al. (2016) explain that these are computed through inverse steady BEM, where the loads are averaged over the cycle, so actual values may differ, secondly, that the α amplitude is greater for the non-rotational case. In Figure 7.3 a corrected non-rotational curve has been

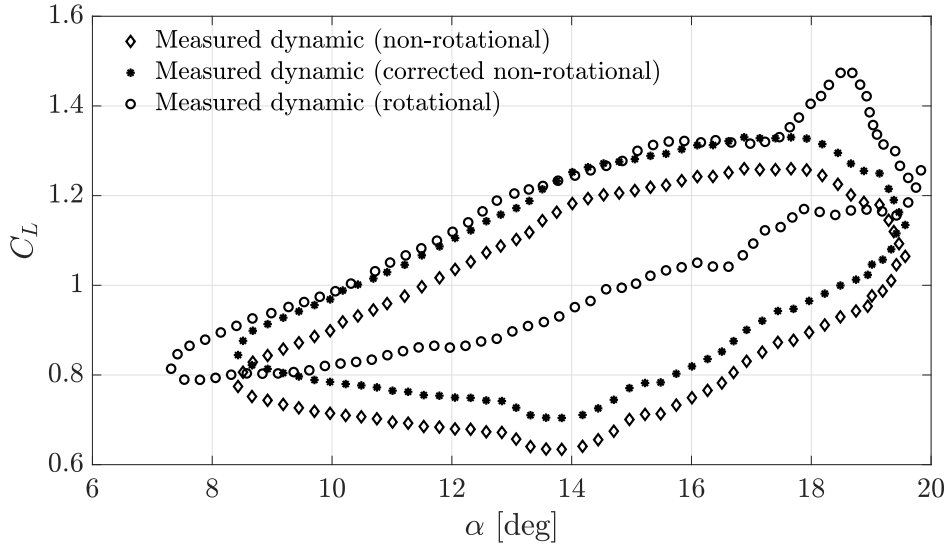

Figure 7.3: Unsteady lift coefficient with angle of attack for the NREL S809 aerofoil for a rotating and non-rotating aerofoil (reproduced from Guntur et al. (2016)).

produced by aligning with the expected $C_L(10°) = 1$. The corrected curve is compared with the rotational curve.

The rotating foil generates a larger value of C_L, with a prominent increase due to vortex shedding visible from 17° to 19°. During the return from stall the value of C_L is approximately 50% greater for the rotational case. This confirms that dynamic lift is enhanced by rotational augmentation, and the severity, in terms of the area enclosed by the hysteresis is reduced.

7.2.1 Accuracy of dynamic stall model

The dynamic stall model agrees well quantitatively for increasing α, and captures qualitatively the hysteresis shape and transient vortex shedding which characterises dynamic stall. The non-rotational model over predicts C_L while returning from stall, however for a rotating blade the corresponding C_L are much greater in this region (Guntur et al., 2016). A qualitative comparison with rotational dynamic data for the NREL S809 was made. There is some discrepancy with this data since the non-rotational and rotational curves are not aligned in the linear region, as one would expect. After applying a correction to the non-rotational data the difference between the curves agrees qualitatively with the difference between the modelled curves, suggesting that the modification is sufficient to superimpose the effect of rotational augmentation on

the unsteady loading.

Load prediction errors in the subsequent chapters through dynamic stall modelling will have little affect globally. This is because dynamic stall is mostly confined to inner blade regions, near the hub, which contribute less to power and bending moments than outer blade sections do.

7.3 Tank scale validation

In this section a global evaluation of the model is made against tank scale measurements.

The proposed model is used to predict the root bending moment (M_y) time series for a tank scale turbine. The turbine has three blade, with a rotor diameter of 1.2 m and is bottom mounted. Full specifications of the turbine can be found in Payne et al. (2017). The blades comprise NACA 63-8XX profiles of various thickness. Unfortunately, the dynamic stall time constants required by the proposed model are unavailable for this profile. On this basis the static lift and drag coefficients for each section are here assumed to follow the NACA 63-816, which is representative of the blade section at $0.75R$, which has a 16% maximum thickness. The load coefficients for this profile were obtained using the Xfoil software (Drela, 1989). The Xfoil simulation was carried out using a Reynolds number of 0.249×10^6 and $N_{crit} = 5$, where N_{crit} describes the turbulence level of the fluid or roughness of the surface, both of which affect the location where laminar to turbulent transition in the boundary layer occurs. The value of 5 was selected because of recent experiments carried out on wind turbine sections where this value was computed for a turbulent intensity of 8% in the flow (Wilcox and White, 2017), which is the same turbulence level encountered in here. As discussed in subsection 2.3.2, the turbulence level in U_r at the blade may be greater than that of the flow due to wake distortion. However, this effect is neglected in the subsequent analysis. The dynamic stall time constants for the NREL S813, are used in the simulation because this profile also has a maximum thickness of 16%.

The empirical parameters for the NREL S813 are shown in Table 7.1, with the dynamic time constants shown in bold. The empirical constants are taken from Sheng et al. (2010), with slight modifications made using the Ohio State University (OSU) wind tunnel test data (Janiszewska et al., 1996). The dynamic constants are shown in bold. The rotational parameters: $b_3 = 0.5$ and $b_4 = 0.5$, are tuned to the NREL S809 profile using the NREL Phase VI test data (as discussed in section 3.2), since no

empirical data is available for any other profiles, these are used.

Table 7.1: Table of empirical parameters for the NREL S813.

$\alpha_{\mathbf{ds0}}$	0.3306
α_{ss}	0.2443
α_0	-0.0436
C_{D0}	0.021
$C_{N\alpha}$	6.876
E_0	0.1
ζ	1
$\dot{r_0}$	0
$\mathbf{T}_\alpha$	4
$\mathbf{T_v}$	8
$\mathbf{T_{vL}}$	11
B	0.5
b_3	0.5
b_4	0.5

The turbine dimensions used in the simulation are shown in Table 7.2.

Table 7.2: Dimensions of tank scale turbine

Parameter	Value
Tip radius	0.6 m
Hub height	1.0 m
Tower diameter	0.1 m
Hub distance from tower	0.12 m
Radius at three quarter span	0.45 m
Chord at three quarter span	0.05 m

Experiments were carried out in the FloWave curved wave tank (Ingram et al., 2014) at The University of Edinburgh, during the FlowTurb campaign (Draycott et al., 2019). The onset flow conditions are monochromatic opposing waves, in a sheared current with both turbulence and tower shadow present. The flow parameters are shown in Table 7.3. Those relating to waves are measured in the presence of the current. A flow time series is modelled using these parameters, where the peak wave induced velocity is aligned with the peak freesurface elevation measured at the turbine.

The modelled and measured M_y time series are shown in Figure 7.4 over 50 periods of revolution (T_r). The fluctuations appear to be dominated by the wave period (T_a),

Table 7.3: Flow and operating parameters used in the comparison

Parameter	Value
Water depth	2 m
Tip-speed ratio	7
Current velocity (rms at hub height)	0.81 ms^{-1}
Froude number	0.183
Reynolds number (diameter)	1.092×10^6
Reynolds number (three quarter span)	0.249×10^6
Shear exponent	1/15
Wave height	0.1 m
Wave period	2.5 s
Wave direction	π
Turbulent intensity	8%
Turbulent length scale	0.2 m

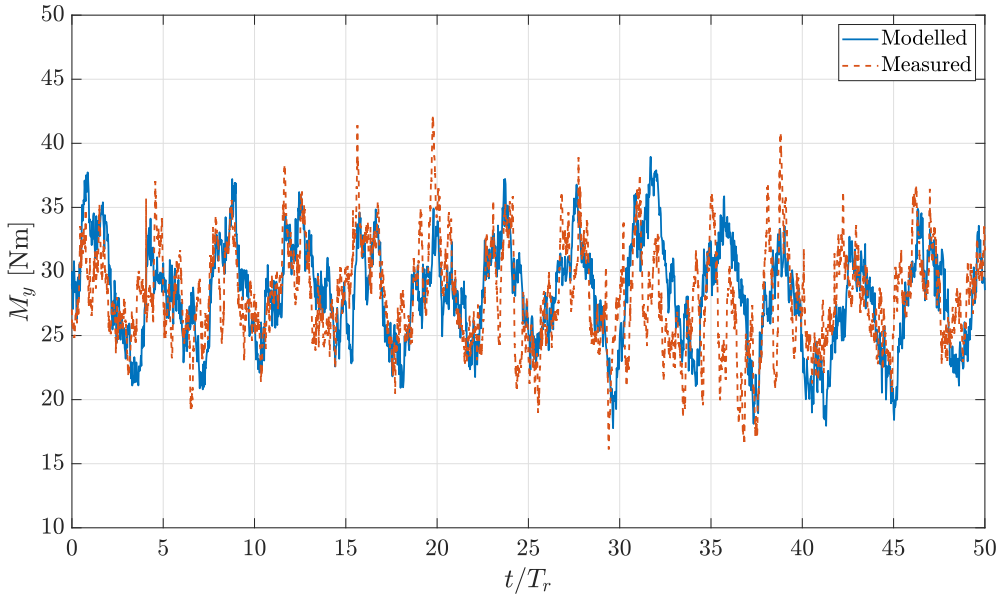

Figure 7.4: Measured and predicted root bending moment time series for a tank scale tidal turbine over 50 periods of revolution.

where $4T_a \approx 15T_r$. The proposed model agrees qualitatively with the measured data by reproducing these dominant fluctuations. Quantitatively, there is a 1% difference between the mean values and a 3% difference between the standard deviations, showing good agreement. However, there is a 17% difference between the kurtosis values (4th statistical moment), which indicates that the extremes are not predicted well. At this

high tip-speed ratio the mean angle of attack is small, therefore the flow is likely to be attached over most of the blade, so using the simplified static load coefficient and dynamic stall coefficients are unlikely to have caused the difference in the extreme values. A possible source of disagreement is a build up of wave reflections in the tank, resulting in the formation of a standing wave, which could combine in phase with the incident wave resulting in a two-fold amplitude increase. This is not captured by the model, however, this eventuality was minimised by not considering the final 30 rotations, when the build up would be most prominent.

A comparison is made in the frequency domain using the amplitude spectrum. The positive amplitudes of the Fourier components are normalised by half the signal length to obtain the M_y amplitude components in Nm. To check convergence a large number of T_r were simulated. Simulations were made from $300T_r$ in steps of $300T_r$ which is equal to $80T_a$. The spectra are shown in Figure 7.5 for each simulation for (a) the full frequency range and (b) a close up of the maximum amplitude, which corresponds to the wave frequency. The frequency (F) is non-dimensional by the rotational frequency (F_r). The maximum amplitude decreases with increasing rotational periods, falling from approximately 3.7 Nm for $300T_r$ to 2.8 Nm for $1800T_r$, with the peak also becoming narrower. It was not possible to simulate past $1800T_r$ due to a lack of memory. However, as shown in Figure 7.6, the maximum amplitude matches the measured data very well.

In Figure 7.6 the energy peaks are annotated to aid the comparison between measured and modelled (over $1800T_r$) values of M_y. As discussed the amplitude of the wave peak is predicted well, however, the 1P peak is under predicted by a factor of three. There are also peaks at 2P and 3P, evident in the measured spectrum, which are absent from the modelled spectrum. The reason for these could be that the blade experiences multiple frequencies due to the tower, or that the blade is sampling returning and neighbouring wakes, which is a realistic problem at high tip-speed ratios. Lastly, the measured spectrum contains lobes either side of the 1P frequency, which are approximately twice the amplitude as those predicted by the model. These side-lobes which occur at $F_r \pm F_a$ are due to the rotational sampling of the wave. They are equivalent to an amplitude modulation and are discussed in more detail in Drayott et al. (2019).

The validation carried out herein demonstrates that the model is capable of predicting the root bending moment for a model scale turbine to a reasonable accuracy. The difference between the mean and standard deviation values were within 1% and 3%, respectively. In the frequency domain the wave amplitude is predicted well, however

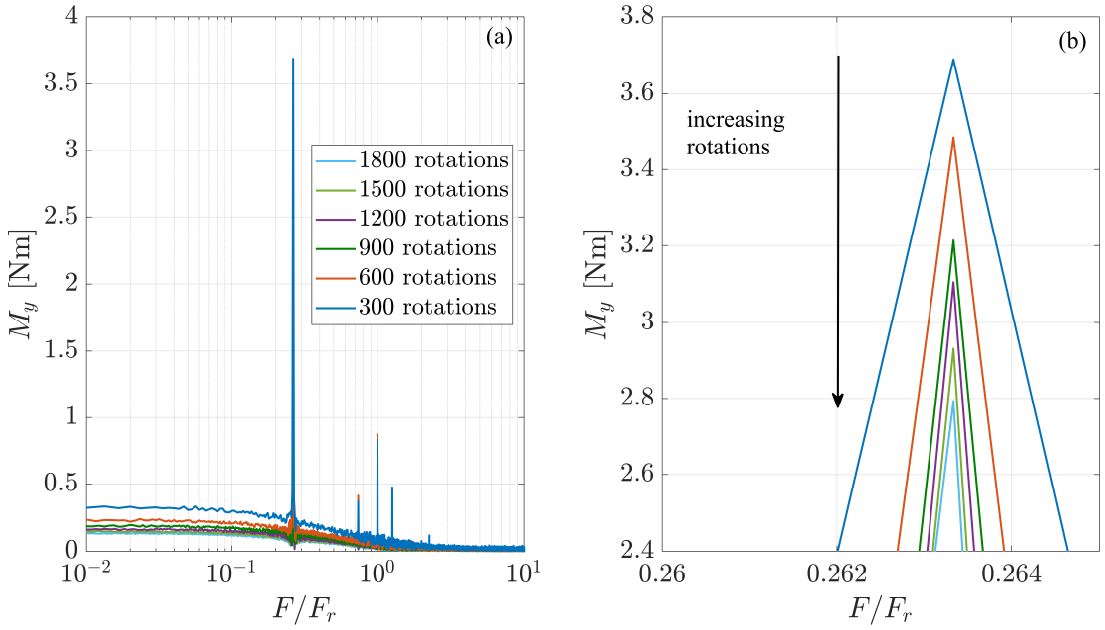

Figure 7.5: Convergence of the modelled bending moment amplitude spectrum where (a) shows the full range and (b) shows the convergence of the maximum amplitude (which corresponds to the wave frequency) with increasing rotations.

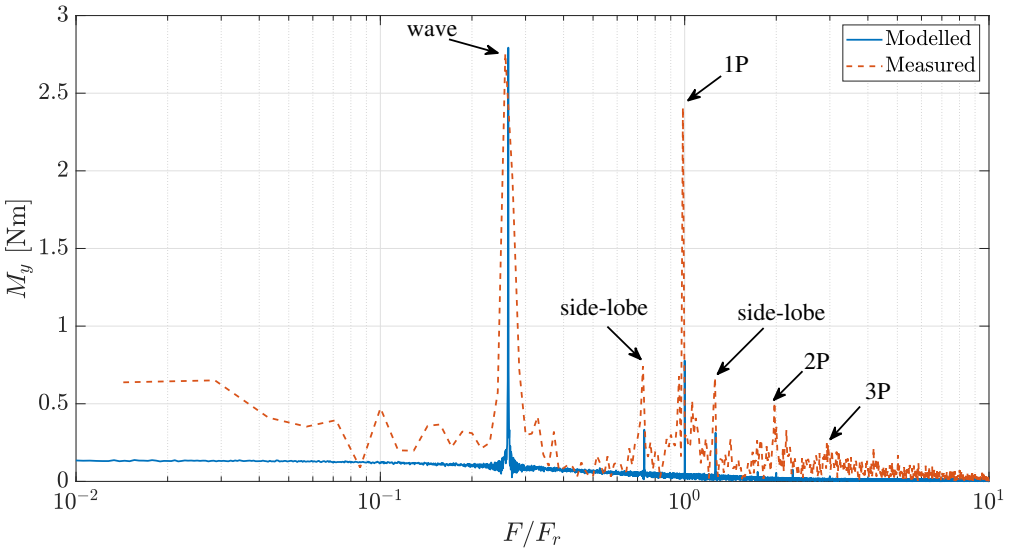

Figure 7.6: Measured and predicted root bending moment amplitude spectrum for a tank scale tidal turbine over measured 50 and 1800 modelled periods of revolution. With frequency non-dimensional by the rotational frequency.

the rotational peaks are under predicted. It is thought that this is due to the high tip-speed ratio. The analysis carried out in the following chapters does not consider tip-speed ratios this high.

Part III

Results

Chapter 8

Blade response to unsteady flow

In this first results chapter the flow conditions considered are artificially synthesised. The unsteady phenomena acting on a tidal turbine blade in both attached and separated flow are explored. A wide range of individual flow and operating conditions are simulated in order to determine which conditions elicit the most severe loads. The responses are categorised by the standard deviation of the root bending moment and the ratio between the unsteady and the quasi-steady mean values, this latter quantity reveals when dynamic stall has a global effect on the loads. After identifying the conditions which elicit the most significant load fluctuations, these results are used to select combined realistic flows which are further examined to reveal how unsteadiness manifests itself along the span of the blade.

The chapter is laid out as follows. Firstly, the lift response at sections along the blade are analysed for single frequency oscillations in angles of attack to determine how the response varies with both frequency and amplitude. Next, the global quantity; the blade root bending moment is investigated for a range of individual flow conditions. In the following section a selection of individual flow conditions are combined to investigate the global response due to combined, realistic flow conditions when operating at rated power. Then for these combined cases the local unsteady characteristics are examined along the blade span. The chapter concludes by investigating how unsteadiness is affected when the turbine operates above the rated current velocity and the power is capped.

8.1 Monochromatic oscillations on the lift amplitude

In this section the nature of the unsteady lift response for both attached and separated flow are investigated. The rotor is assumed to be operating at the optimum $\lambda = 4.5$ and the channel depth, $d =$ 45 m. Single monochromatic α oscillations are considered in the reduced frequency range; $0.05 < k < 1$, in which tidal turbines operate. This preliminary investigation highlights how the amplitude of the lift coefficient is effected by both the frequency and amplitude of the fluctuations.

8.1.1 Attached flow

Attached flow effects are investigated analytically for simple harmonic forcing using the theory of Theodorsen (1935) for a blade section and Loewy (1957) for a rotor blade, as described in section 4.2. This investigation reveals how the effect of shed vorticity, added mass and returning wakes affect the lift response in attached flow.

Assuming pure α oscillations of the form $\alpha(t) = \bar{\alpha} + \mathrm{Re}(\Delta\alpha e^{i\omega t})$, where $\bar{\alpha}$ is the mean value and $\Delta\alpha$ the amplitude, Theodorsen's solution (Equation 4.1) reduces to

$$C_L = \mathrm{Re}([i\pi k + 2\pi C(k)]\alpha(t)). \tag{8.1}$$

The first term in Equation 8.1 is the non-circulatory, added mass effect, and the second term which is multiplied by Theodorsen's function $C(k)$ is the circulatory effect. For a moderate forcing, with $U_r = 7.0$ ms^{-1}, $\Delta\alpha = 4°$, and $\bar{\alpha} = 5°$. Figure 8.1 shows the unsteady lift response at a section near the blade tip, where $r \approx 0.98R$ and $c \approx 0.8$ m. The quasi-steady value ($2\pi\alpha$) corresponding to $k = 0$, is shown for comparison. Three values of k are simulated: $k = 0.07$, $k = 0.16$ and $k = 0.31$. Representing a wave period of 5.1 s, a 1P ($T_r = 2.3$ s) and a 2P forcing, respectively. It is observed that the unsteady responses are counter-clockwise hysteresis in C_L with α, and that there is an amplitude reduction and phase lag compared to the quasi-steady value, which for this k range decreases inversely with k.

Theodorsen's model conveniently separates the circulatory and non-circulatory components, enabling the contribution of each to the total C_L response to be quantified.

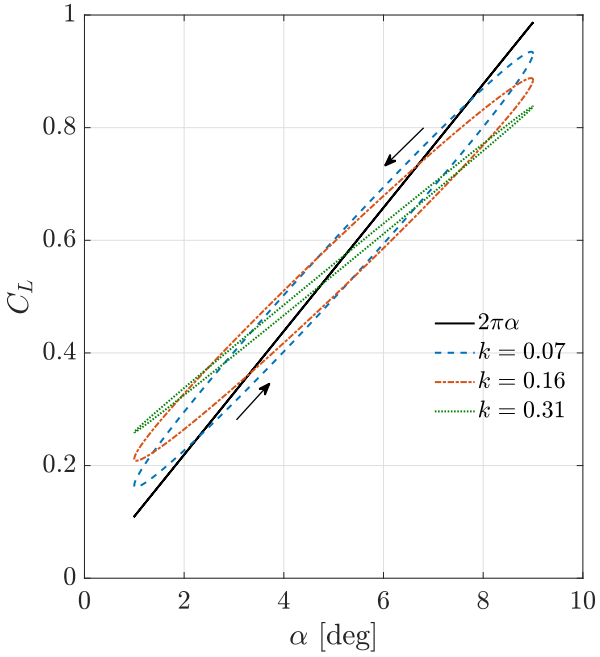

Figure 8.1: Unsteady lift coefficient given by Theodorsen for a section near the tip of the blade. The static linear value ($2\pi\alpha$) is shown for comparison.

Defining the normalised lift coefficient amplitude (ζ) as

$$\zeta = \frac{|C_L|}{2\pi|\Delta\alpha|} = |(F + iG) + i\frac{k}{2}|, \tag{8.2}$$

where the first and second terms are the circulatory and added mass components respectively, $F = \mathrm{Re}(C(k))$ and $G = \mathrm{Im}(C(k))$. In Figure 8.2(a) the contribution to ζ is shown for $k \in [0, 4]$. If $k \leq 1.8$ then $\zeta < 1$, however, when $k > 1.8$, the amplitude exceeds the steady value ($\zeta > 1$) and then increases linearly with k, approaching the added mass linear response in the limit. Figure 8.2(b) shows a magnification of the region $k \in [0, 1]$, which is the range in which a a tidal turbine operates. Interestingly, for $k < 0.6$ the total response is less than the circulatory response. To investigate the inequality; $|C_L^c| > |C_L|$, which states that the magnitude of the circulatory response is greater than the magnitude of the total response is examined and expanded. The

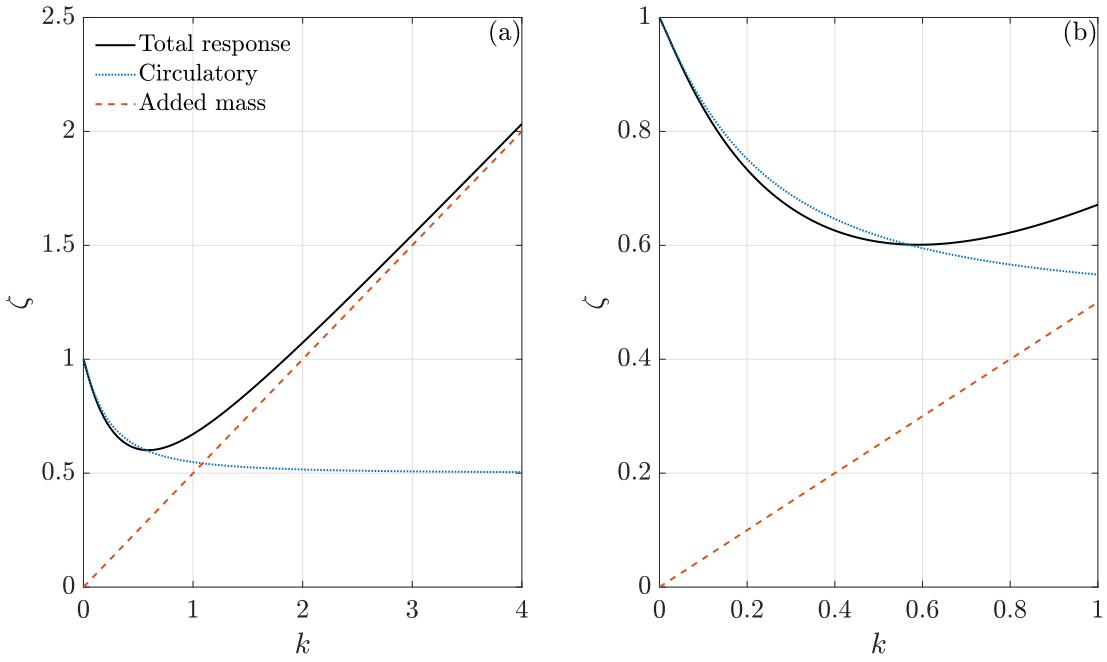

Figure 8.2: Normalised amplitude of the total, circulatory and non-circulatory coefficients with reduced frequency for pure angle of attack oscillations for (a) the full range and (b) a magnification of the range tidal turbines operate in.

inequality is split into real and imaginary parts and simplified,

$$\left[|C_L^c| > |C_L|\right] \equiv \left[\sqrt{F^2+G^2} > \sqrt{F^2+\left(G+\frac{k}{2}\right)^2}\right] \Leftrightarrow \left[G^2 > \left(G+\frac{k}{2}\right)^2\right] \\ \Leftrightarrow \left[0 > Gk+\frac{k^2}{4}\right] \Rightarrow \left[0 > 4G(k)+k\right]. \tag{8.3}$$

Solving $-4G(k) = k$, yields $k \approx 0.56$. Therefore, in the interval $[0 < k < 0.56]$, added mass dampens the total response. This is because the circulatory and added mass components are combined vectorially, which has previously been reported for harmonic heaving motion Leishman (2002). Since tidal turbines mostly operate within this interval, added mass effects are unlikely to become a problem. This is important since it has been suggested (Maniaci and Li, 2012; Whelan et al., 2009; McNae, 2013) that the high density of water might lead to significant added mass effects for tidal turbines. However, this is not the case as long as $k < 0.56$. Conversely, the circulatory response, associated with dynamic inflow, is the significant effect, which concurs with the scale model results of Milne et al. (2013a). Clearly the observation from Figure 8.1,

that the amplitude reduces inversely with k, is only true inside the interval $[0 < k < 0.56]$. For $k > 0.56$ the relationship inverts.

The significance of neighboring and returning wakes on the circulatory lift component can can be investigated by replacing $C(k)$ with $C(k, W)$ which is a function of Loewy's function W defined in Equation 4.4. To determine W the averaged wake convection velocity v_i for a tidal turbine is computed using Equation 4.6. In Figure 8.3 C_L hysteresis loops are predicted for a section near the tip for a range of $k \in [0.07, 0.72]$ using both Loewy and Theodorsen' models. In each case $\Delta\alpha = 4°$, $\bar{\alpha} = 5°$, $U_0 = 2.7$ ms^{-1}, $\bar{a} = 0.3$ and $U_r = 7.0$ ms^{-1}. The results show that as k increases, the phase lag and amplitude reduction from $2\pi\alpha$ also increases. For the lowest k, corresponding to a large 10 s wave, the width of the hysteresis ellipse predicted by Loewy is reduced compared to Theodorsen's prediction. However, the amplitude is slightly increased. The amplitude predicted by Loewy continues this trend until $k = 0.31$. For larger k there is a greater added mass contribution and the difference between the two theories becomes negligible. Thus, for this turbine and these operating conditions, a slight increase in the amplitude of C_L is expected for $k < 0.3$ due to returning and neighbouring wakes.

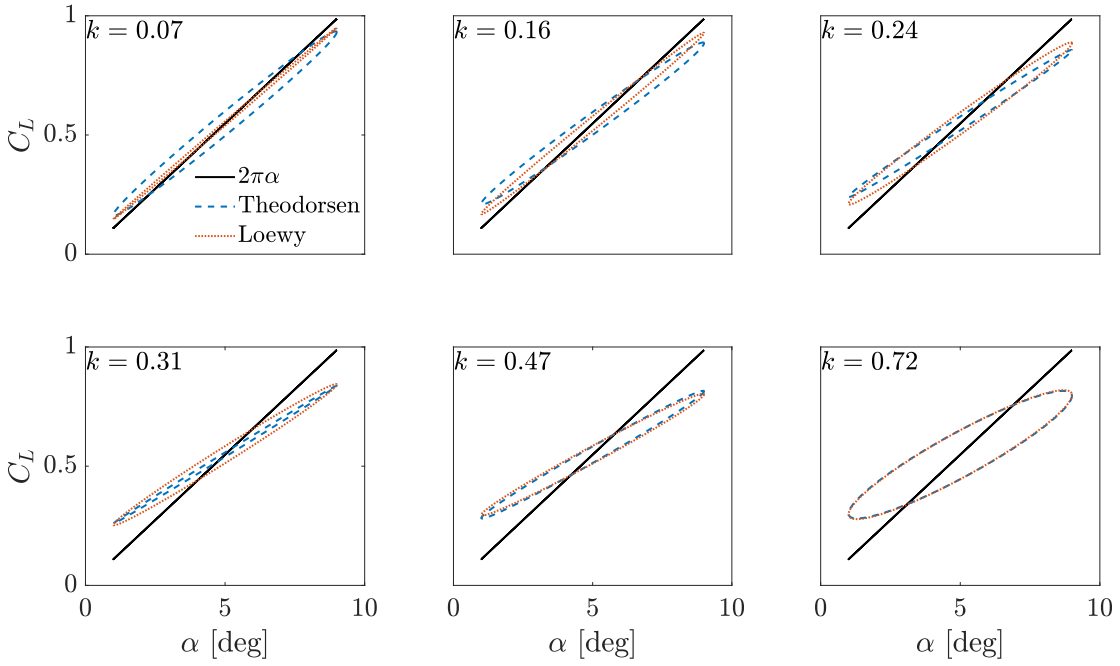

Figure 8.3: Unsteady lift coefficient given by Theodorsen and Loewy for a section near the blade tip for a range of oscillation frequencies.

Loewy's theory is now used to compare the C_L amplitude (ΔC_L) for different forcing conditions at the three quarter span. The individual components tested are: four waves

$T_a = [10, 7.5, 5, 2.5]$ s, $H = [5, 4, 2, 1]$ m, corresponding to $k = [0.05, 0.06, 0.09, 0.18]$, respectively, four turbulent constituents $f_t = [0.01, 0.1, 1, 4]$ Hz, shear with $\nu = 1/7$ and tower shadow with $D = 2$ m and $x = 6$ m. The waves, which are generated using wave theory, are following the current with $U_0 = 2.7$ ms^{-1}, $\lambda = 4.5$, $r = 0.75R$ and $c \approx 1.3$ m. The individual ΔC_L responses are shown in Figure 8.4. Here the forcing frequency ($\omega = 2\pi/T_a$) is non-dimensional by the rotational frequency Ω. Notably, the four largest values all have amplitudes which are an order of magnitude greater than that due to tower shadow. The ΔC_L due to shear is moderate and turbulent frequencies greater than unity are negligible in comparison. It is important to note, however, that wave frequencies shown here do not include rotation through the time-varying depth decay which results in variation of α at multiple frequencies.

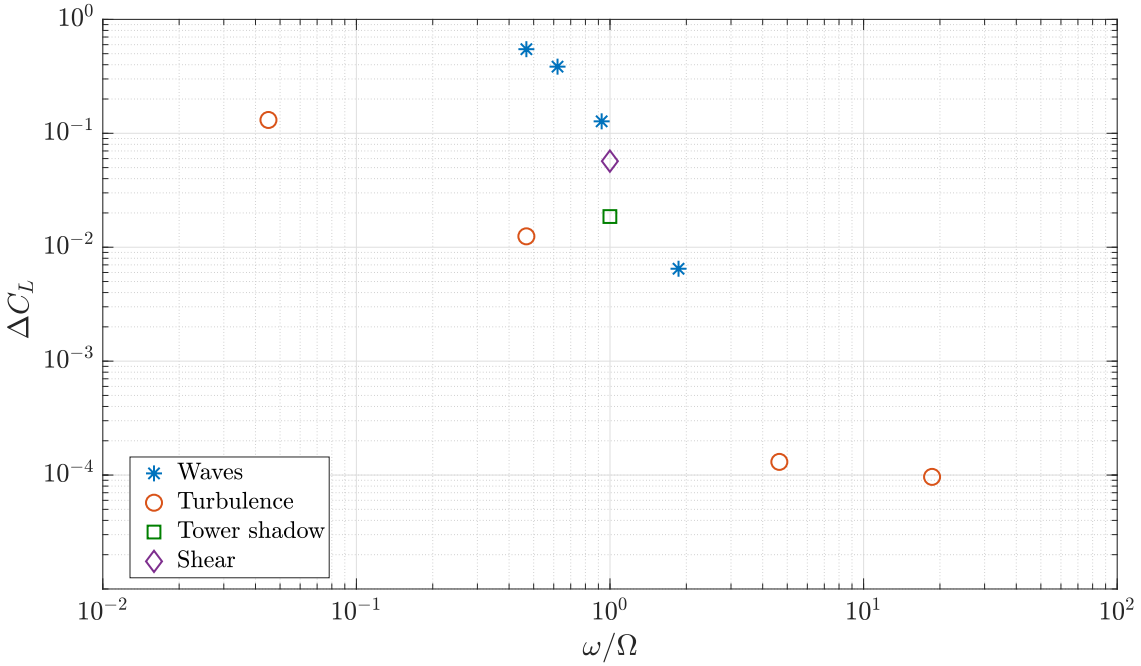

Figure 8.4: Individual lift amplitudes at the three quarter span for following waves).

8.1.2 Separated flow

Examples of dynamic stall lift hysteresis are simulated using the low-speed dynamic stall model introduced in section 5.3, with the rotational augmentation correction described in section 6.5.

Two blade sections undergoing unsteady flow separation are considered. Figure 8.5 (a) shows representative load hysteresis at a mid-blade section where $r \approx 0.56R$ and

$c \approx 1.26$ m, for a harmonic forcing representing a 10 s period wave, $\Delta\alpha = 5°$, $\bar{\alpha} = 10°$ and $k = 0.05$. The C_L response increases linearly past $\alpha_{ss} \approx 12°$, until the end of the cycle, then C_L lightly stalls and returns to the static value. In Figure 8.5 (b) the load hysteresis loop is shown for a blade section near the root where $r \approx 0.15R$ and $c \approx 1.6$ m. A larger $\Delta\alpha = 10°$, $\bar{\alpha} = 14°$ and $k = 0.09$ occur here due to the reduced tangential velocity, which increases the flow angle. There is a linear increase in C_L above α_{ss} until $\alpha \approx 19°$, which is the critical angle for dynamic stall. The flow then separates at the leading edge, and there is a build up of circulation into a concentrated vortex. A LEV then detaches and convects over the chord, producing a load overshoot more than twice the quasi-steady value. The vortex sheds near the trailing edge and stall occurs, however, as α continues to increase a secondary vortex forms, producing a slight C_L recovery at $\alpha \approx 23°$. Deep stall then occurs and C_L rapidly decreases. Then once α becomes sufficiently small enough the flow reattaches.

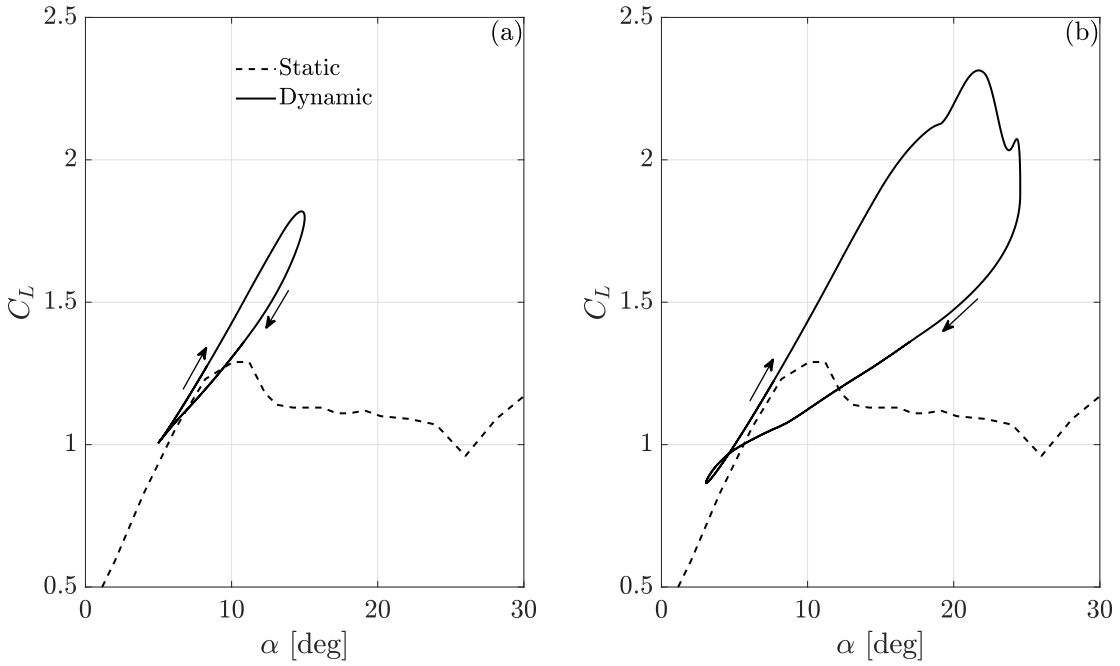

Figure 8.5: Unsteady lift coefficient with angle of attack for (a) light dynamic stall and (b) deep dynamic stall.

8.2 Individual flow conditions on the blade root bending moment

An investigation of the wide range of unsteady flow conditions which a tidal turbine blade may encounter is carried out. The individual flow conditions which are important are split into three types: once per revolution (1P) which is caused by the blade rotating through spatially non-uniform flow (sheared current, tower shadow and yaw), multiple frequency turbulence and monochromatic waves. These results are used to select combined realistic flows which are further examined in section 8.3.

The velocity time series and induction factors (using the quasi-steady method) are modelled as described in section 6.2. The unsteady load model, corrected for rotation, as described in chapter 6, is used to predict the loads at 100 sections along the full span of the blade, which are summed along the blade span to give the root bending moment (M_y). The responses are categorised by the standard deviation of the root bending moment coefficient (C_{M_y}), defined as

$$C_{M_y} = \frac{2M_y}{\pi R^3 \rho U_0^2}. \tag{8.4}$$

Events where the mean root bending moment coefficient exceeds the quasi-steady counterpart ($C_{M_y(q.s)}$) are identified by isolines of the ratio ($\bar{C}_{M_y}/\bar{C}_{M_y(q.s)}$), where the overbar denotes the time averaged value. This will indicate the extent to which dynamic stall is having a global effect.

8.2.1 Once per revolution

A tidal turbine blade will likely encounter a 1P load fluctuation on every rotation throughout its service life due to the sheared current or the potential field of the support structure, hence, the predictable 1P unsteady loads are very important for fatigue analysis. To investigate a range of inflow conditions, $U_0 \in [1.2, 3.5]$ ms^{-1}, $\nu \in [0.05, 0.3]$, $\hat{x} \in [1, 5]$ $\lambda \in [3, 7]$, $d =$ 45 m and $\gamma \in [0, \pi]$ are simulated over 50 rotations, where $\hat{x} = x/D$, is the non-dimensional upstream distance from the tower to the rotor. For each flow condition the standard deviation of the root bending moment ($\sigma_{C_{M_y}}$) is predicted. As shown in Figure 8.6, the fluctuations due to the rotation through the shear profile and tower shadow are small. The magnitude increases for the steepest shear gradient and when the blades are closer to the tower, however, since no isolines are present,

these instances do not lead to a global dynamic stall. Next, the fluctuations due to

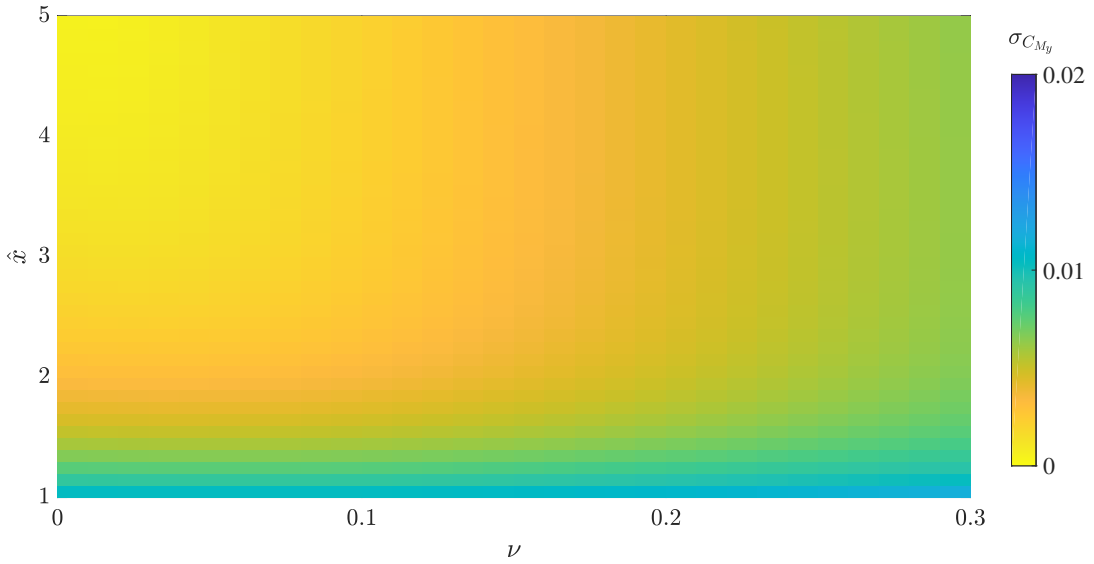

Figure 8.6: Filled contour map showing the standard deviation of the root bending moment due to tower shadow and the sheared current profile.

a change in λ and γ are simulated for a range of current velocities with $\nu = 1/7$. As previously shown in Figure 6.5, altering λ from the optimum value reduces C_P. This is also the case for $\gamma \neq 0$, since the freestream is reduced by $\cos\gamma$, as shown in Figure 8.7 for $\lambda = \in \{3, 5, 7\}$. Comparing the predicted C_P, $\lambda = 5$ which is close to optimum produces the highest C_P up to $\gamma = 28°$, for higher values of γ the results for $\lambda = 3$ indicate that the performance is improved by decreasing λ, whereas increasing λ degrades performance. Thus for lower λ the rate at which C_P degrades for an increase in γ is slower. The load fluctuations displayed in Figure 8.8 show that, $\sigma_{C_{M_y}}$ increases with γ and the inverse of λ. At low λ, dynamic stall effects the mean loads, even when the only source of unsteadiness is the rotation through the shear layer. This is evident by the 1.00 isoline indicating the boundary where $\bar{C}_{M_y}/\bar{C}_{M_y(q.s)}$ exceeds unity for the $\gamma = 0$ case. The range increases to $\lambda \approx 4$ for $\gamma = 40°$, and $\lambda \approx 4.5$ for the largest $\gamma = 50°$ case. However, as γ increases the ratio decreases, with no values above 1.10 occurring for $\gamma > 20°$. At high λ, added mass effects result in lower C_{M_y} compared to the quasi-steady counterpart. However, the ratio was never found to to be below 0.95, and hence no isolines of values below unity are displayed.

Thus, at low λ, unsteady conditions will always increase the mean loads compared to a quasi-steady prediction. This is due to the slower rotational speed, which reduces the tangential velocity, which increases α. As α increases along the blade, dynamic stall

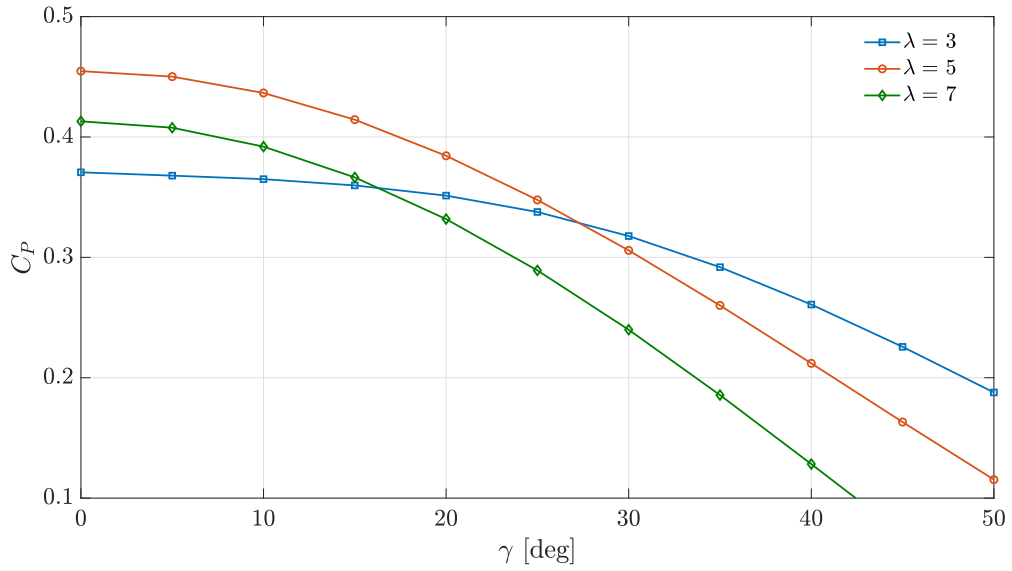

Figure 8.7: The relationship between the rotor power coefficient and a yaw misalignment angle when operating at the optimum tip-speed ratio.

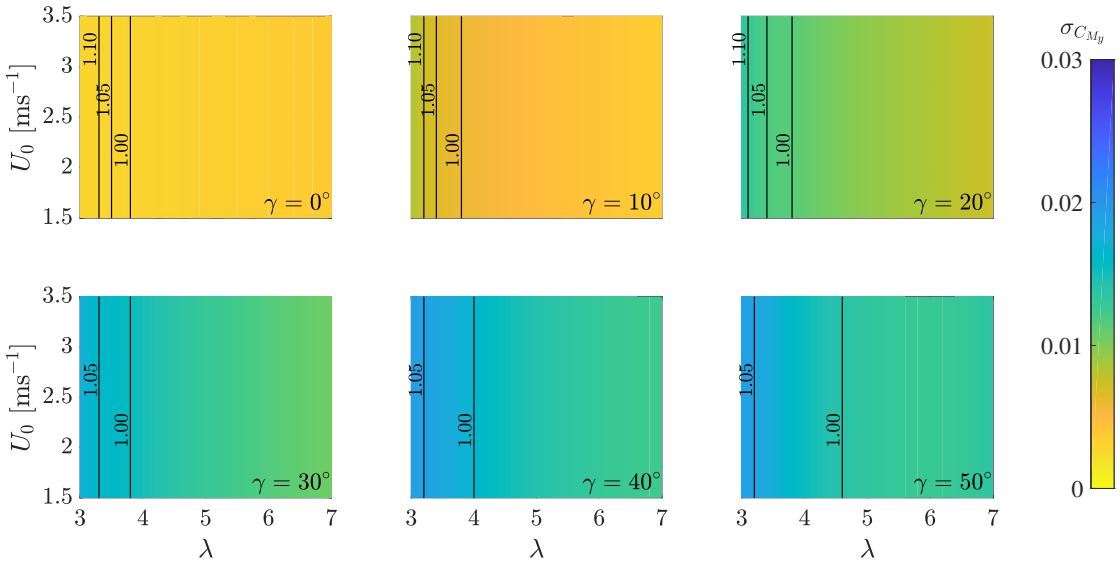

Figure 8.8: Filled contour map showing the standard deviation of the root bending moment due to varying current velocity, tip-speed ratio and yaw angle. Solid contour lines show the ratio between the mean root bending moment and the quasi-steady counterpart.

becomes the dominant loading regime. These results show that the yaw misalignment must be extremely significant to affect the mean loads at the optimal λ.

8.2.2 Turbulence

A range of turbulent parameters, $I_x \in [5, 20]\%$, and $R_t \in [0.5, 1]$, are simulated over 50 rotations with $L_x = 20$ m and $\lambda = 4.5$. From the results shown in Figure 8.9, it is clear that increasing turbulence intensity elicits the greatest change in $\sigma_{C_{M_y}}$, and that isotropic turbulence produces similar fluctuations to anisotropic turbulence. Notably, there are no isolines showing where the ratio between $\bar{C}_{M_y}$ and $\bar{C}_{M_y(q.s)}$ exceeds unity, which indicates that turbulence in isolation does not affect the mean loads for a rotor operating at optimal λ.

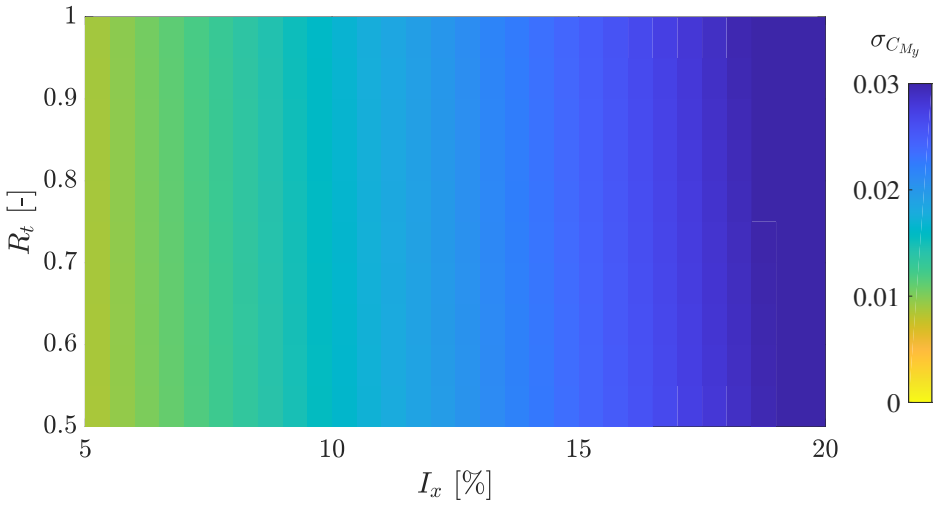

Figure 8.9: Filled contour map showing the standard deviation of the root bending moment due to varying turbulence intensity, length scale and anisotropy ratio.

8.2.3 Regular waves

A number of regular waves are simulated with parameters, $H \in [1, 6]$ m, $T_a \in [2, 12]$ s and $\theta \in [0, \pi]$, are simulated over 50 rotations with $\lambda = 4.5$, d= 45 m and U_0 =2.7 ms^{-1}. It is important to note that some of these waves cannot physically exist, such as $H = 6$ m with $T_a = 2$ s, which would break due to its large steepness, and opposing waves with shorter values of T_a, which will not propagate. However, these waves are included for completeness of the parameter space. In addition, the relative wave period (T_r) which produces the same T_a value for following and opposing waves directions is different due to the Doppler effect (see section 2.4), further more, the depth decay of the wave orbitals differ for each direction, in both magnitude and frequency.

The predicted $\sigma_{C_{M_y}}$ for all flow combinations are shown in Figure 8.10. Here, the load amplitude is found to be proportional to T_a and, to a lesser extent, H_s. Waves following the tidal current ($\theta = 0$) lead to greater amplitude fluctuations at shorter wave periods, compared to waves opposing the current ($\theta = 180°$). The amplitude is significantly reduced for $\theta = 2\pi/5$ and $3\pi/5$. This is because the perpendicular velocity component becomes small for angles close to $\pi/2$. The isolines show that ratio between $\bar{C}_{M_y}$ and $\bar{C}_{M_y(q.s)}$ only exceeds unity for the most extreme waves which have very large heights combined with a long period.

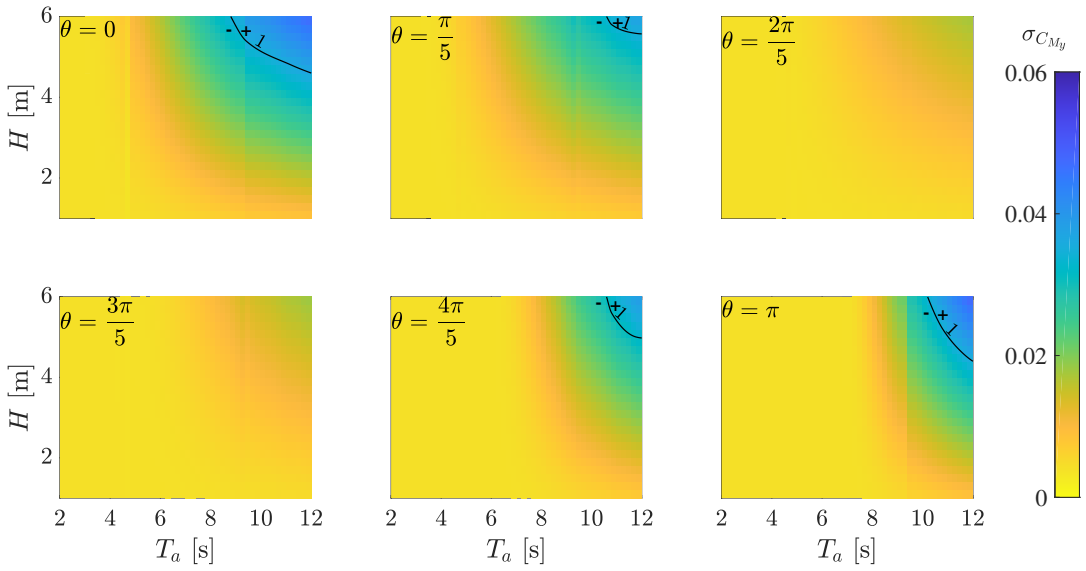

Figure 8.10: Filled contour map showing the standard deviation of the root bending moment due to varying wave period, wave height and wave direction. Solid contour lines show the ratio between the mean root bending moment and the quasi-steady counterpart.

These results confirm that T_a has more influence on blade loads than H_s and that the load amplitude is increased when waves follow the current.

8.3 Combined flow conditions on the blade root bending moment

In this section the individual flow components are combined as outlined in section 6.2. Combinations of shear, yaw, waves and turbulence are simulated to determine which combined flow condition produces the largest fluctuations. Informed by the results from

the individual forcing tests, the flow parameters considered are: isotropic turbulence with $I_x = 10\%$ and $L_x = 20$ m, a wave with $H = 5$ m, $T_a = 10$ s and $\theta = 0$ and a yaw misalignment of $\gamma = 30°$. The turbine operates at the optimum, $\lambda = 4.5$ and at the velocity for rated power, $U_0 = 2.7$ ms^{-1}. Shear is present for all cases, with $\nu = 1/7$.

Using the spectral method to generate turbulence ensures that the expected value and standard deviation both remain constant, albeit with a slight loss from the input standard deviation (see section 6.2). However, random phasing could potentially produce extraordinarily extreme values due to components combining or cancelling. To ensure extreme values are statistically significance (i.e. within a 95% confidence interval), a number of random samples are simulated and the minimum ($\min u_x$) and maximum ($\max u_x$) velocities for each sample recorded. The sample histograms from 10^4 simulations are shown in Figure 8.11, which have been fitted to the generalised extreme value distribution. Using this distribution the 95% confidence interval (CI) for

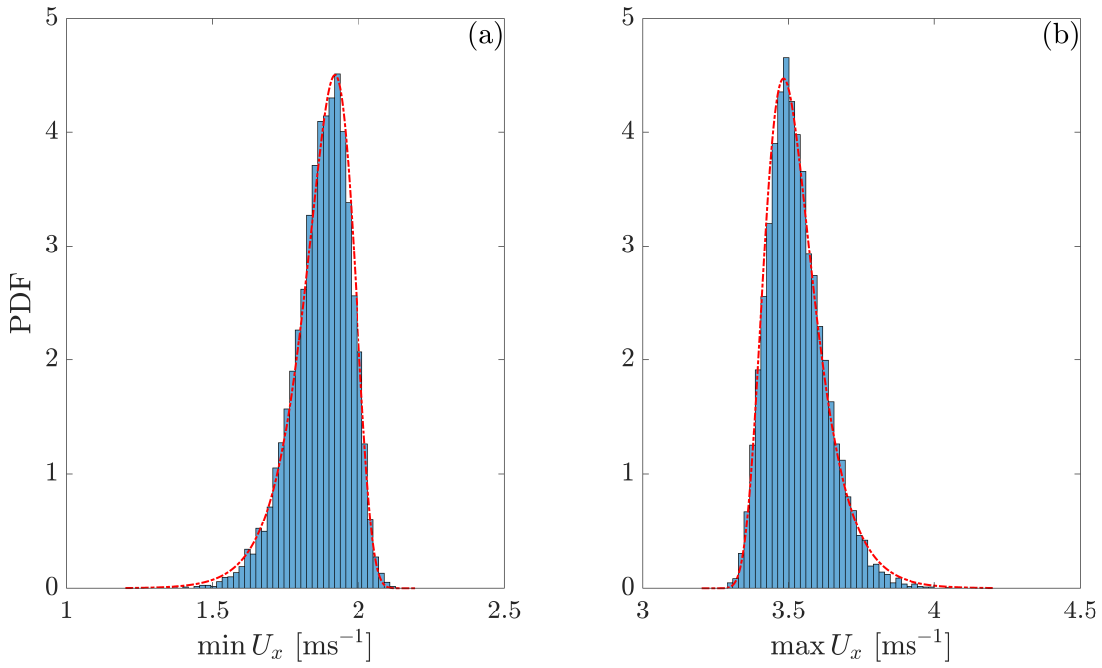

Figure 8.11: Histogram and generalised extreme value distribution fit for (a) the minimum turbulent velocity variation and (b) the maximum turbulent velocity variation.

the minimum and maximum values are [1.617 - 2.025] and [3.375 - 3.785], respectively. Ensuring that extreme values remain inside this 95% CI, ensures that a statistically significant case is used for comparison. In addition, identical turbulent time series are

used for all cases. The extreme values for the sample used in the following analysis are: $\min u_x = 1.864$ m^{-1} and $\max u_x = 3.488$ m^{-1}, which are comfortably inside the 95% CI. The histogram of the sample time series, shown in Figure 8.12, approximately fits a normal distribution.

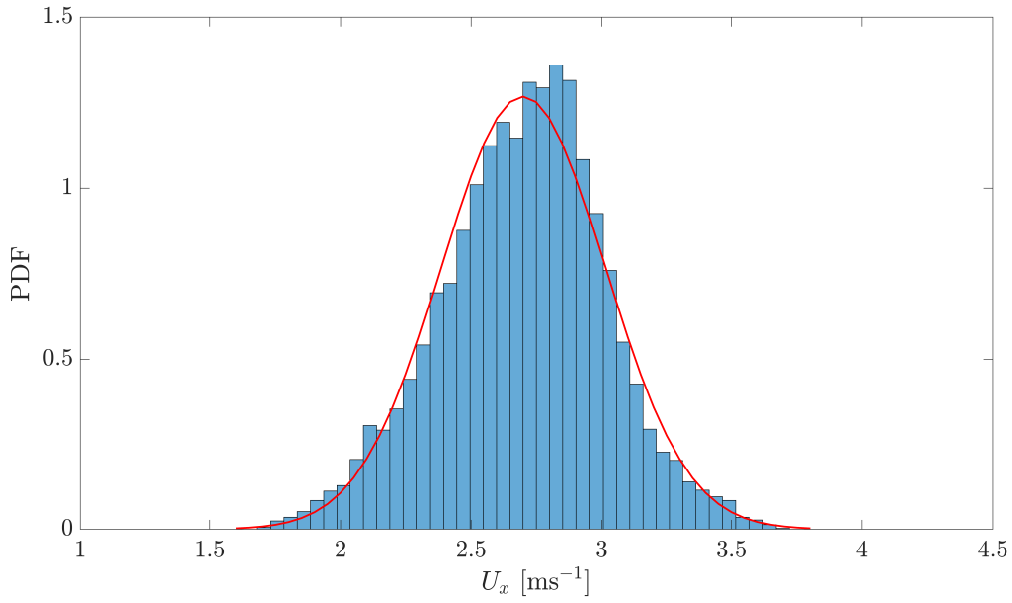

Figure 8.12: Histogram and normal distribution fit for the simulated turbulent velocity time series.

The distribution of C_{M_y} over 100 rotations are presented as a boxplot for each flow combination. A boxplot shows the distribution of the quartiles as illustrated in Figure 8.13. The boxplots for the eight possible flow combinations are shown in Figure 8.14. As expected, shear in isolation produces the narrowest C_{M_y} spread and the inclusion of a yaw misalignment reduces the median value and increases the spread. Turbulence significantly increases the spread and produces some very large outliers. The total spread of C_{M_y} due to waves is narrower than the turbulence case, however, the interquartile range (IQR), containing the 25th to 75th percentiles has the largest spread of the set. Combining waves with turbulence, produces the widest spread and maximum value in the set. The further inclusion of a yaw misalignment reduced both the median, the peak and the spread and produces the minimum values in the set.

Having identified that waves combined with turbulence produce the largest C_{M_y} amplitude, a range of waves combined with turbulence are simulated with and without

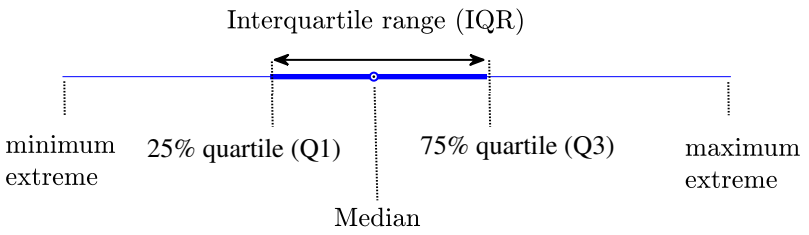

Figure 8.13: Box plot descriptor.

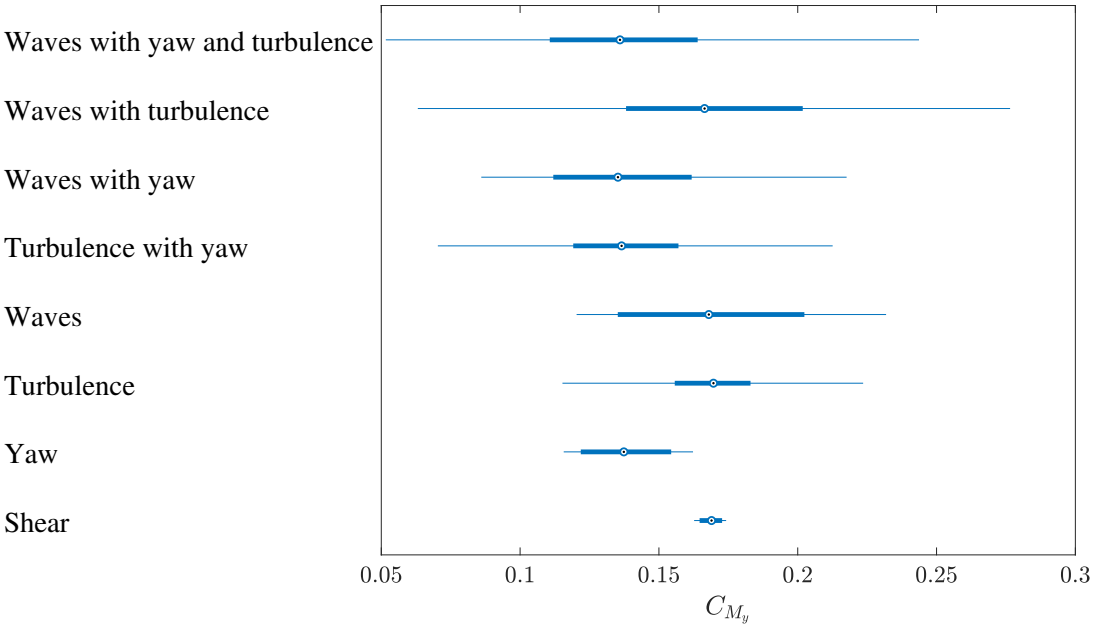

Figure 8.14: Box plot showing the summary statistics for the root bending moment time history over 50 blade rotations for several unsteady flow conditions.

a yaw misalignment to determine which cases lead to $\bar{C}_{M_{y(q.s)}}$ overshoots. The predicted $\sigma_{C_{M_y}}$ are shown in Figure 8.15 (a) for $\gamma = 0$ and (b) for $\gamma = 30°$. Comparing the two cases, there is a small reduction in $\sigma_{C_{M_y}}$ across the full range for $\gamma = 30°$, confirming that a yaw misalignment reduces $\sigma_{C_{M_y}}$ when combined with waves and turbulence. The range and severity of $\bar{C}_{M_{y(q.s)}}$ overshoots for $\gamma = 0$ compared to waves without turbulence (Figure 8.10) is unchanged, whereas for $\gamma = 30°$ both have increased, with more than a quarter of the test space affected.

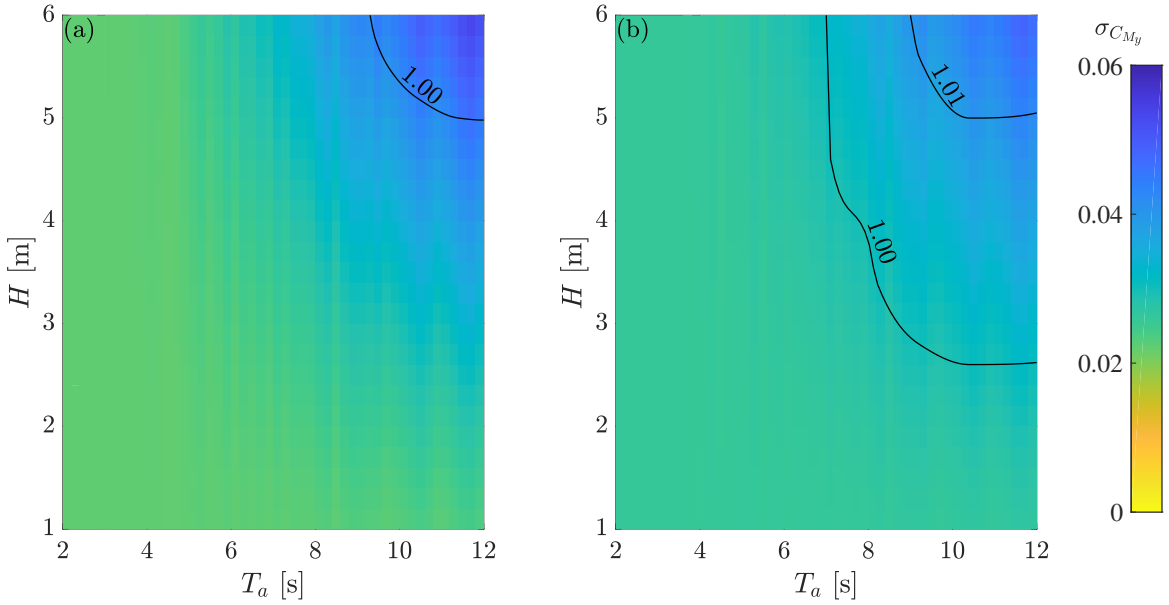

Figure 8.15: Filled contour map showing the standard deviation of the root bending moment due to varying wave period and wave height combined with turbulence for (a) zero yaw angle and (b) yaw angle of 30°. Solid contour lines show the ratio between the mean root bending moment and the quasi-steady counterpart.

8.4 Unsteadiness along the blade span due to combined flow conditions

In this section an investigation of how unsteadiness unfolds along the blade for different flow combinations is carried out revealing which unsteady phenomena are occurring.

8.4.1 Local unsteady load characteristics

The unsteady response at three span locations, tip ($r = 0.98R$), mid ($r = 0.56R$) and root ($r = 0.15R$), are analysed for each combined flow. Box plots shown in Figure 8.16 present the C_L summary statistics at each location. Notably, both the mean and the amplitude of C_L grow as one travels inboard from the tip, and become very large at the root. As with C_{M_y}, the mean value is reduced when the rotor is yawed. The case without a yaw misalignment (waves with turbulence), as expected, produces the largest median at each location. This case also yields the widest spread at the tip and mid locations, however, conversely the shortest at the root. At the root the inclusion of a yaw misalignment induces extremely large fluctuations, especially when combined with

turbulence. The case where all flow conditions are present leads to a maximum $C_L \approx 5$, which is extreme. The reason being the very large α fluctuations arising from the slow tangential velocity, coupled with the tangential component induced by the rotor misalignment. This case also produces the widest spread along with the maximum and minimum values for the set. Interestingly, at the root, when turbulence and yaw combine, a much wider C_L spread than waves with yaw occurs. Waves combined with turbulence produces the smallest spread in the set, whereas this forcing produced the widest C_{M_y} spread (see Figure 8.14).

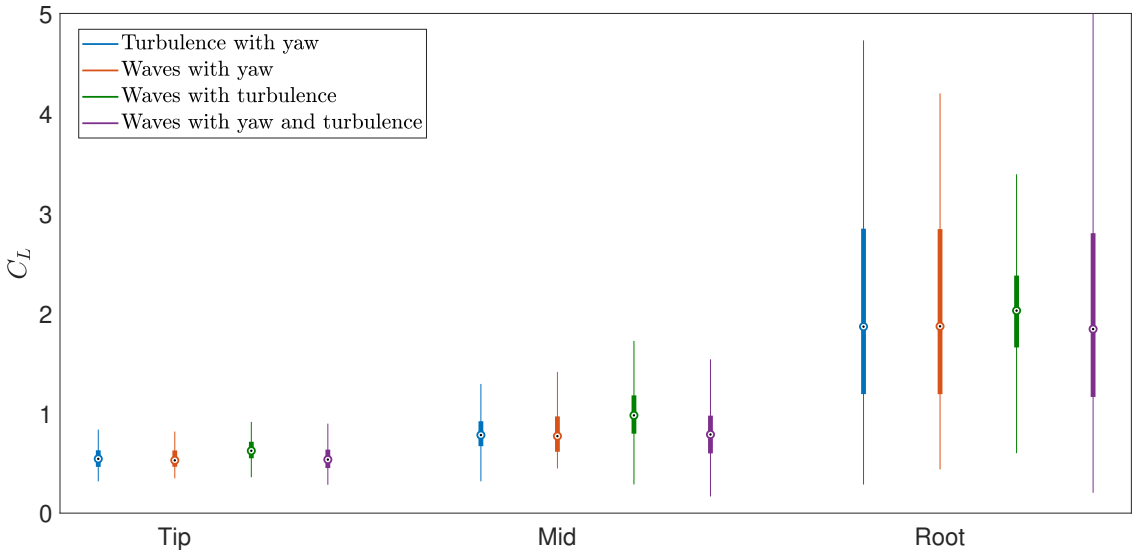

Figure 8.16: Box plot showing the summary statistics for the lift coefficient time history over 50 blade rotations for several unsteady flow conditions at the tip mid and root blade sections.

While the results in Figure 8.16 show the largest unsteady loadings in relative terms (relative to the local dynamic pressure), Figure 8.17 shows how these are relevant in absolute terms, by computing the distributed thrust force (F_T) at the three blade locations. This force component is responsible for M_y. The pattern is quite different from C_L. Notably, with dimensions considered, the median value decreases as one travels inboard from tip. The F_T spread is reduced at the root, which is most notable for yawed cases. There is little difference between the spread at the tip and mid sections, since the larger C_L at the mid section counteracts the smaller U_r compared to the tip. The combination of waves with turbulence produces the largest median, peak and widest spread of the set, which, occurs at the mid-section.

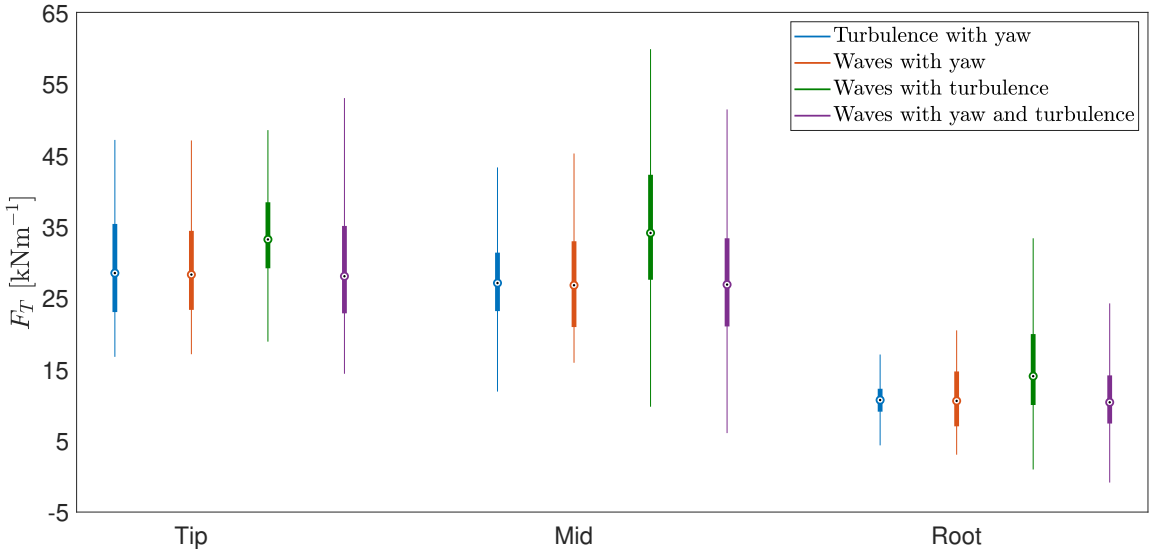

Figure 8.17: Box plot showing the summary statistics for the thrust force time history over 50 blade rotations for several unsteady flow conditions at the tip mid and root blade sections.

8.4.2 The unsteady lift spectrum

To understand which unsteady phenomena are occurring along the blade span the peak frequency constituents are determined by examining the C_L frequency spectrum. These constituents can then be used to compute the dominant reduced frequencies along the blade span.

Four flow cases are considered; turbulence combined with a yaw misalignment, a regular wave following the current combined with a yaw misalignment, a regular wave opposing the current combined with a yaw misalignment and a regular wave following the current combined with turbulence. For each of these cases $U_0 = 2.7$ ms^{-1} with $\eta = 1/7$ and $\lambda = 4.5$. Turbulence is isotropic with $I_x = 10\%$ and $L_x = 20$ m. The yaw misalignment, $\gamma = 30°$, and for the wave cases the relative wave period is 10s and $H = 5$ m. For each flow case the energy spectra are shown for three sections along the blade: tip, mid and root, and the four largest angular frequencies (ω) are identified.

The first flow case; turbulence with a yaw misalignment, is shown in Figure 8.18. For this case the rotor rotational frequency, Ω is by far the dominant constituent, which for the tip and mid-sections is followed by the frequency which corresponds to the turbulent time scale (ω_t). However the highest frequency components occur at the tip due to the rotor 2P and 3P terms, these higher frequencies combined with slower $\bar{U}_r$ at the root will produce higher values of k. The second flow case; a following regular

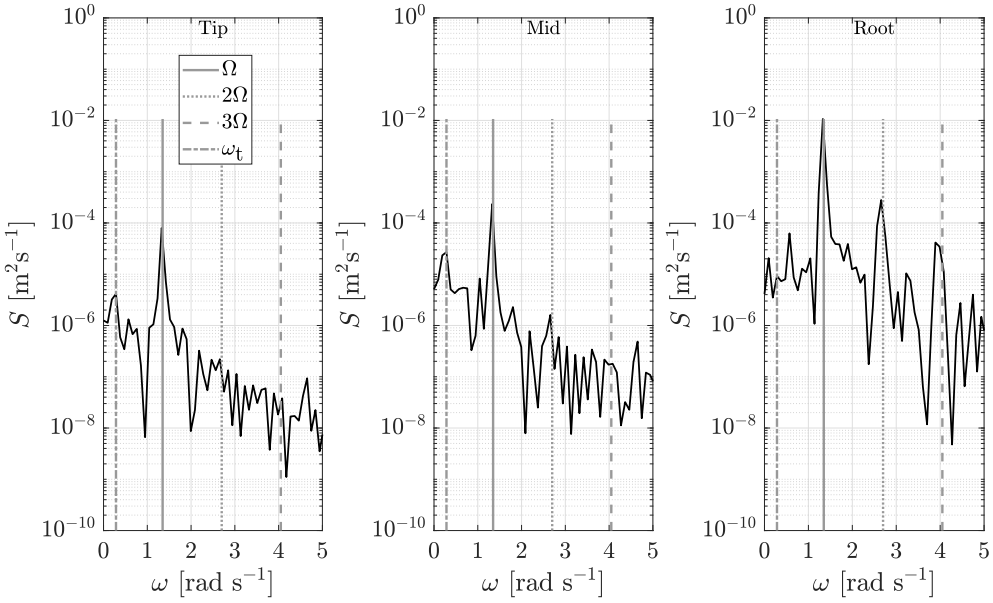

Figure 8.18: Energy spectra of the lift coefficient response to turbulence combined with a yaw misalignment. Showing the four peak frequency components at blade locations near the tip, mid-section and root.

wave combined with a yaw misalignment, is shown in Figure 8.19. Here Ω and ω_a have similar magnitudes at the tip and mid-section, however, at the root the rotation is more dominant with a 2P harmonic evident. At each location the third peak corresponds to the rotational sampling of the wave $(\Omega + \omega_a)$.

The next flow case; an opposing regular wave combined with a yaw misalignment, is shown in Figure 8.20. The is very similar to the following wave case, however, due to the opposing current the period is shorter thus ω_a is higher. Because of this the wave has less energy which is confirmed by comparing the magnitude of the wave peaks for both cases.

The final flow case; a following regular wave combined with turbulence, is shown in Figure 8.21. Now, with no yaw misalignment, the rotor frequency is barely visible at the tip and mid-section of the blade. It is slightly more prominent at the root section, however, the wave frequency is dominant throughout.

8.4.3 Local unsteady load and flow phenomena

Here a visualisation of the unsteady phenomena discussed in section 8.1 is given for each of the four flow combinations by displaying on the blade: the location and duration of

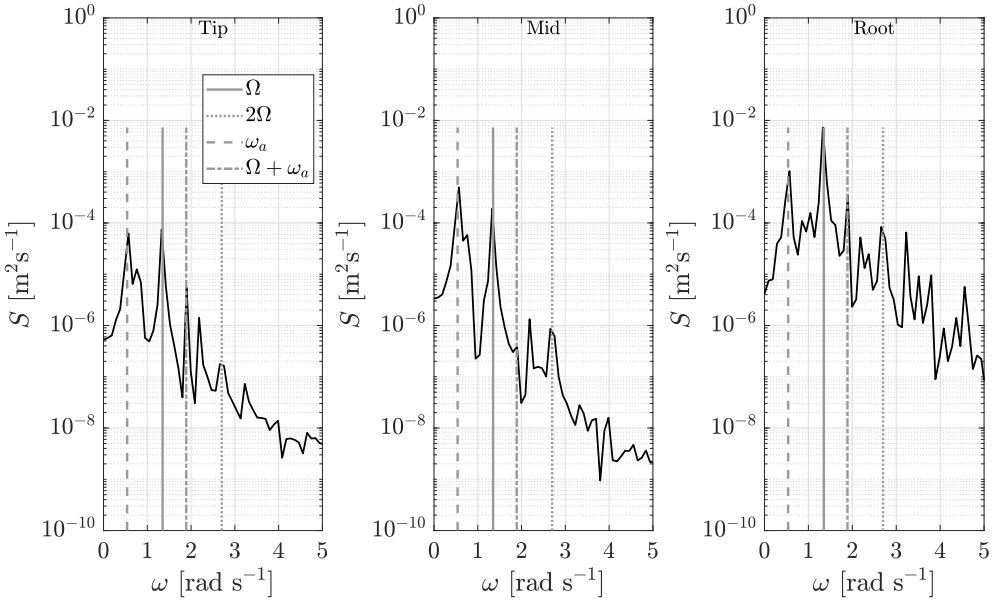

Figure 8.19: Energy spectra of the lift coefficient response to a following regular waves combined with a yaw misalignment. Showing the four peak frequency components at blade locations near the tip, mid-section and root.

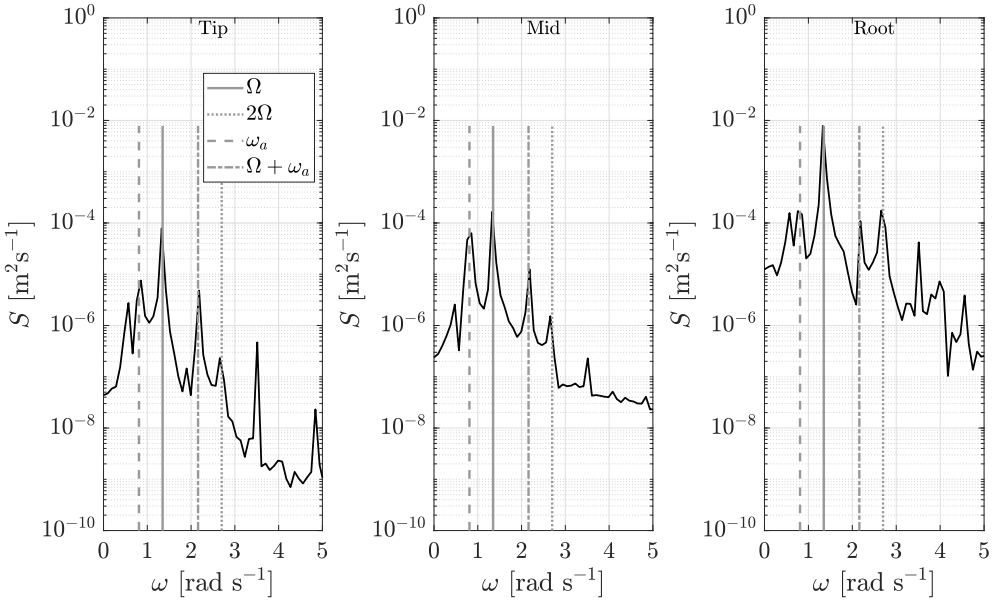

Figure 8.20: Energy spectra of the lift coefficient response to an opposing regular waves combined with a yaw misalignment. Showing the four peak frequency components at blade locations near the tip, mid-section and root.

flow separation, leading edge vortex shedding, highly unsteady regions, where returning wakes are discernible and where added mass is significant. The frequencies used to

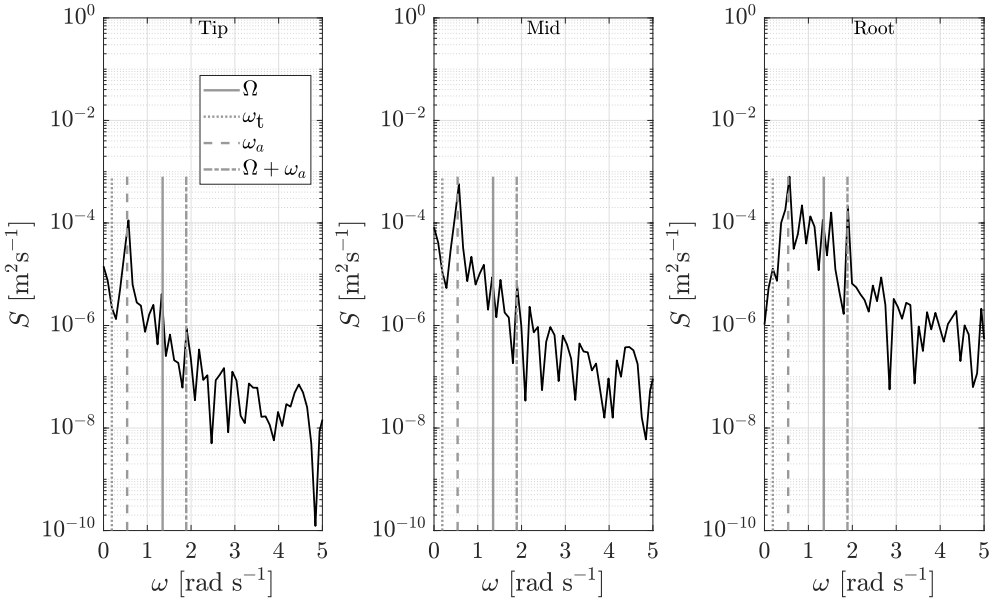

Figure 8.21: Energy spectra of the lift coefficient response to a following regular wave combined with turbulence. Showing the four peak frequency components at blade locations near the tip, mid-section and root.

compute k were determined by analysing the C_L frequency spectrum, as discussed in the previous section. The three highest peaks at the tip, mid-section and root of the blade are used to compute k. In reality there are multiple values of k present, however, looking at those due to the dominant frequencies gives an indication of the governing effects.

The representative blades in Figure 8.22 show (a) turbulence and yaw, (b) waves and yaw, (c) waves, turbulence and yaw and (d) waves and turbulence. The results reveal that variation in the unsteady phenomena is dependent on the flow forcing. The flow becomes highly unsteady ($k > 0.2$) for every case, however, the transition point on the blade depends on the forcing. For $\gamma = 0$ (d) this occurs at the root of the blade, whereas for turbulence combined with a yaw misalignment, transition occurs outboard of the mid-section. Interestingly, only two of the flow conditions have regions where added mass effects are significant ($k > 0.56$). These are when either turbulence (a) or waves (b) are combined with yaw misalignment. For blade (a) undergoing turbulence and yaw, the affected area is almost a quarter of the span. This case also contains the set maximum $k \approx 0.9$. Compared to blade (b), the affected region is only half the size and confined to the very bottom of the blade where the global effect is negligible due to the low relative velocity and short moment arm. In addition, the flow is separated inside

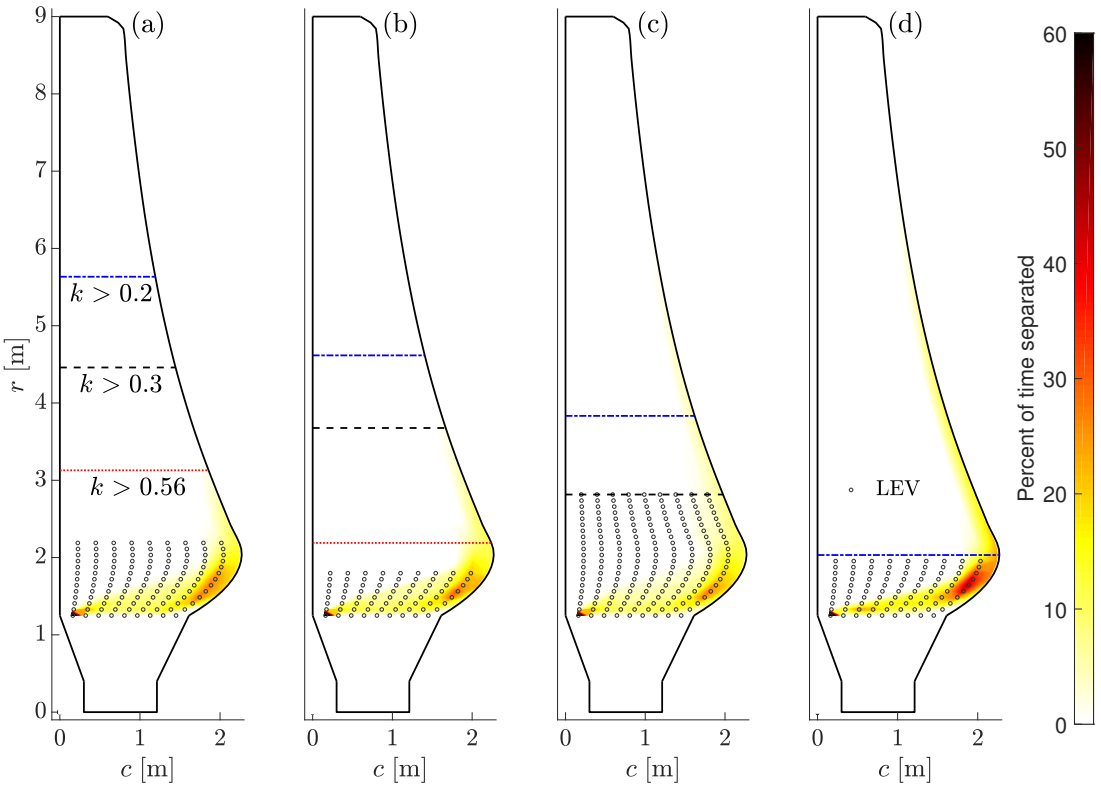

Figure 8.22: Parameterisation of unsteady effects along the blade span for, (a) turbulence and yaw, (b) waves and yaw, (c) waves, turbulence and yaw and (d) waves and turbulence.

these regions, thus, dynamic stall will govern the loading. At the outer sections of each blade the flow is fond to be attached and $k < 0.3$. Therefore, returning wakes will give rise to slightly larger amplitudes than predicted by the model. Observing separated flow phenomena, it is clear that both regimes of dynamic stall (light and deep) occur on each blade. The blade without a yaw misalignment (d) contains the largest region of flow separation, spanning from the hub to $r \approx 6$ m. Deep dynamic stall, identified by the presence of the LEV, is mostly confined to the blade root. However, for waves with both turbulence and yaw (c) the region covers almost a third of the span. As shown in Figure 8.15, this leads to an overshoot in $\bar{C}_{M_y}$.

8.5 Unsteady characteristics outside rated speed

So far it has been assumed that the turbine operates at rated power ($U_0 = 2.7$ ms^{-1}). But, how do the unsteady effects change below or above the rated velocity? An idealised

power curve for a variable speed tidal turbine is shown in Figure 8.23. Below U_0 for

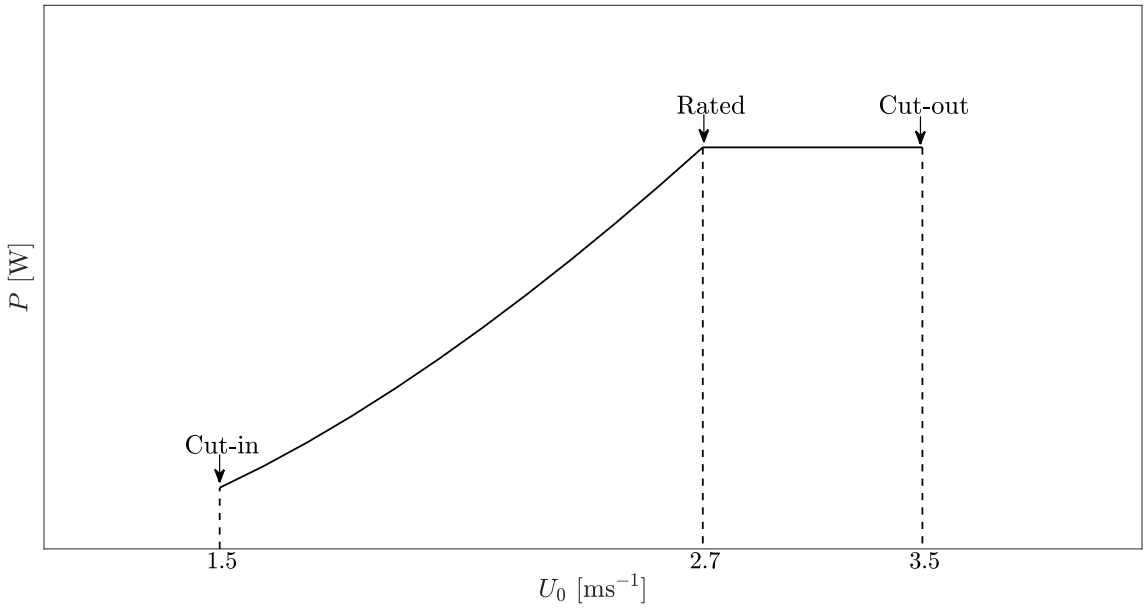

Figure 8.23: Power with change in velocity curve for a variable speed tidal turbine.

rated power the turbine operates at optimum λ to achieve max C_P. The relative velocity is reduced compared to rated power, and as shown in Figure 8.8, a change in U_0 at $\lambda = 4.5$ does not affect the load amplitude. Above rated velocity the power must be controlled to match the rated value. If the device has a pitch mechanism, the blades are pitched towards the inflow to reduce α and C_L, whilst the rotor speed is kept constant (Whitby and Ugalde-Loo, 2014). In Figure 8.24 (a) U_r is shown for three current velocities: $U_0 = [2.7, 3.0, 3.2]\,\mathrm{ms}^{-1}$, with Ω fixed there is only a small increase in U_r from the rated velocity, however, power scales with the cube of this there is a significant increase. To keep the power constant a pitch is applied to reduce α. In Figure 8.24 (b) the α distribution along the blade is shown with a change in the pitch angle ($\Delta\beta$) from the rated velocity ($U_0 = 2.7$ ms^{-1}) applied. The thrust and tangential forces are shown in Figure 8.24 (c) and (d), respectively. There is a significant reduction in F_T compared to that during rated velocity, this is because both C_L and C_D reduce with α. However, an increase in F_{Tan} occurs at the mid section. This is due to the decrease in C_D, which F_{Tan} is inversely proportional to, conversely from $0.75R$ there is a reduction in F_{Tan}. The decrease in C_D is less here as the flow remains attached, thus the decrease in C_L is more significant. If the turbine is without a pitch mechanism, the power can be actively controlled by reducing the rotor speed, referred to as "underspeed" (Arnold et al., 2016). The latter will reduce λ. Referring back to Figure 8.8, as shown by the solid

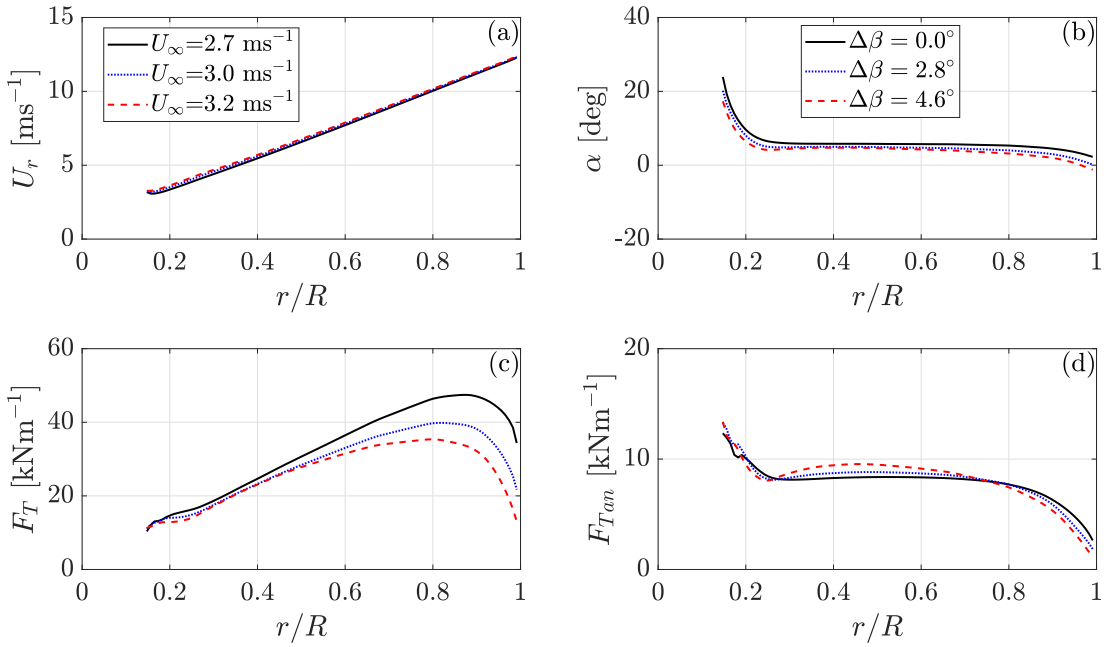

Figure 8.24: Effects of an increase in the current velocity with a constant pitch applied showing, (a) relative velocity, (b) angle of attack, (c) thrust force and (d) the tangential force.

isolines this will lead to increased separation and dynamic stall. For a pitch regulated turbine the consequences are unclear. To investigate the cases shown in Figure 8.22 are reproduced with $U_0 = 3.2$ ms^{-1} and pitched the blades by 4.6°. The results presented in Figure 8.25 show that separation still occurs at the same locations on the blade but the duration has reduced, which concurs with the observations from Figure 8.24 (c) and (d). The severity of the unsteadiness in terms of k has also reduced due to the increase in U_r. For waves with turbulence (d),there are no sections undergoing highly unsteady oscillations ($k > 0.2$). The range of LEV shedding increases for all cases undergoing a yaw misalignment, whereas for the case without (d) the range decreases. Hence, for a pitch controlled turbine operating above rated velocity, LEV shedding would increase if a yaw misalignment is present.

8.6 Discussion and summary of results

A summary of the key results and a brief discussion of how these can be generalised for different turbines and operating conditions are provided herein.

Analytical unsteady attached flow solutions were used to investigate the C_L response

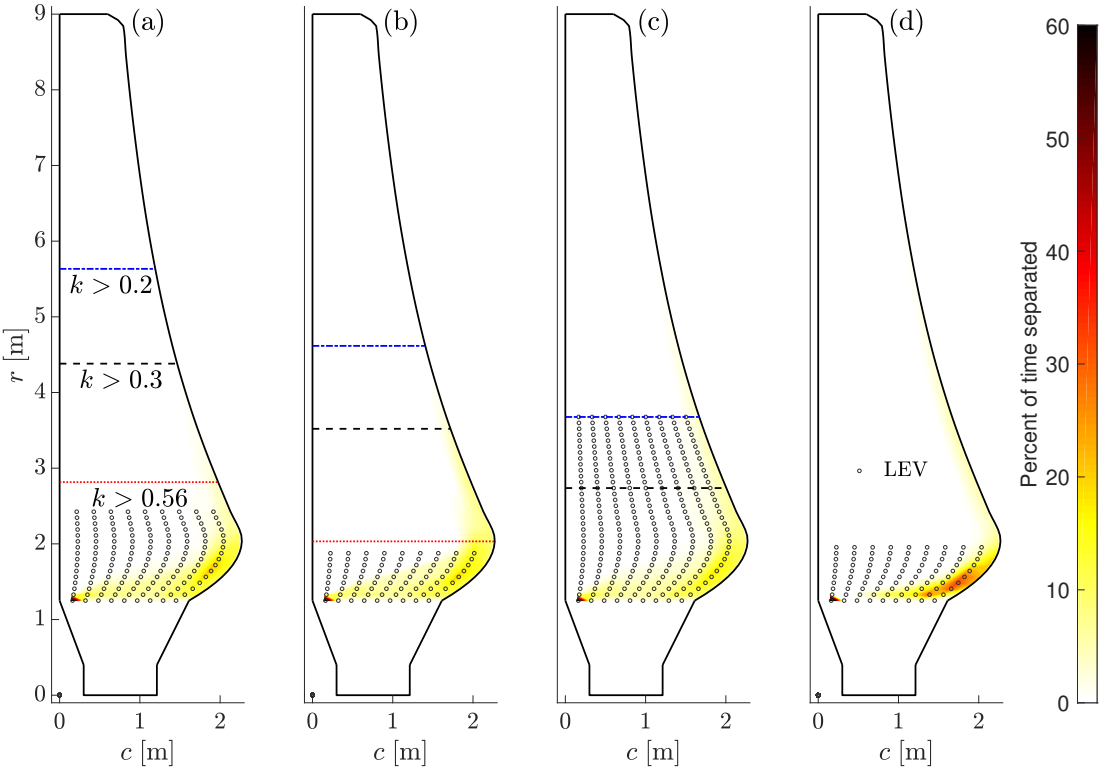

Figure 8.25: Parameterisation of unsteady effects along the blade span for, (a) turbulence and yaw, (b) waves and yaw, (c) waves, turbulence and yaw and (d) waves and turbulence.

for monochromatic α oscillations. For $k < 0.56$, added mass effects damp the total response, however, above this value significant load fluctuations can occur. This result is valid for different turbines and operating conditions. The reduced frequency can be computed along the blade span to determine whether added mass effects are significant or not. Returning wakes were found to slightly increase the lift amplitude for $k < 2$. This result is specific to the turbine and operating conditions considered in this study, because Loewy's theory relies on the spacing parameter which is a function of blade solidity and the operating conditions. However, it is possible to generalise this result for different conditions by considering the rate at which shed vorticity is both encountered by each blade and convected downstream. Increasing the rotational speed or decreasing the convection velocity will increase the amount of shed vorticity encountered by a blade because the convection rate has been reduced, conversely decreasing the rotational speed or increasing the convection velocity, will reduce the effect as the shed vorticity will have convected further down stream.

A parameter study of the unsteady flow conditions on the root bending moment was carried out. Large yaw angles ($\gamma > 30°$), low tip-speed ratios ($\lambda < 4$) and very large waves ($H > 5$ m) elicit overshoots in the time averaged blade root bending moment compared to the quasi-steady prediction. This indicates that dynamic stall is having a global affect. Turbines operating at higher λ will be less susceptible to dynamic stall, whereas, those operating at lower λ will incur significant increases in the global load response. This is important for turbines which curtail power when operating above the rated velocity by reducing the rotor speed.

In this study extreme waves ($H > 5$ m) were found to dominate over extreme turbulence ($I_x > 15\%$). However, this result is specific to a hub depth of 27 m, it is postulated that extreme turbulence may be more significant for turbines installed closer to the bed. Conversely, floating devices, which are located closer to the free surface will likely experience greater loadings due to waves. The most significant root bending moment amplitudes are produced by large ($H > 2$ m), long period waves ($T_a > 5$ s) which follow the current. The amplitude is further increased when combined with turbulence ($I_x > 10\%$). In comparison, loadings induced by the blade rotating through tower shadow and the shear layer are negligible.

Locally, a yaw misalignment induces extreme C_L values at the root of the blade, which can exceed the median value twofold. Conversely, when dimensions are considered, the distributed thrust force is larger at the tip than at the root. However, the peak occurs at the mid section during large waves and turbulence. Flow separation is most prevalent with waves, leading to light dynamic stall (i.e. periodic trailing edge separation) over a large region of the blade. However, deep dynamic stall occurs near the hub of the blade, for all flow combinations. If the power is regulated fixing the rotational speed and pitching the blades to feather, then the effect of yaw misalignment becomes even more critical. In these conditions, the region affected by dynamic stall extends to half of the blade span.

Chapter 9

Unsteady loads due to large wave conditions

In the previous chapter large waves and turbulence were identified as inducing to the greatest blade root bending moment fluctuations. To investigate further this chapter asks; How significant are the unsteady effects of very large, realistic waves on the loads of a tidal turbine blade? Does unsteadiness affect the mean power and thrust of the rotor? And how do the loads change if the rotor operates at tip-speed ratios outside that which produces the peak power coefficient? To answer these questions flow velocity measurements taken at the European Marine Energy Centre during a large wave train are used as an input to simulate the loads.

The remainder of this chapter is laid out as follows. Firstly, a five minute wave train flow sample is identified and the flow sample categorised. Then before examining the rotor performance some theoretical consideration are made with regard to the how the power coefficient varies with flow fluctuations. The study then moves on to evaluating the power, thrust and bending moments due to the measured flow field which are compared to the those expected in a steady flow. An investigation of the time averaged sectional coefficients are carried out before investigating the unsteady flow phenomena occurring at different blade sections, which includes tracing the dynamic stall hysteresis. The chapter concludes by examining how the unsteadiness and mean rotor loads are affected when operating below the optimum tip-speed ratio.

9.1 Flow sample from EMEC

Data used in this chapter was acquired during field measurement campaigns conducted by the University of Edinburgh at the EMEC tidal test site during the ReDAPT project

between 2011 and 2015 (Energy Technologies Institute, 2015). Environmental data acquired up to October 2014 is publicly available at the UKERC Energy Data Centre in an archival format (UKERC, 2018).

9.1.1 ReDAPT data acquisition

Time series of the free surface elevation were acquired using a remotely operable, single-beam acoustic Doppler profiler (SB-ADP) installed on a prototype turbine. The SB-ADP was orientated in the vertical direction measuring a fixed point in space directly above the hub of the turbine. Depth profiles of velocity measurements were provided by seabed mounted divergent beam acoustic Doppler profilers (D-ADP) deployed on the port and starboard sides of the turbine, approximately in line with the rotor plane. The location of the D-ADP is approximately $y = -40$ m, which is deemed far enough away from the rotor wake and tower to be measuring the freestream (McNaughton et al., 2015). The velocity components are measured from 2 m above the bed to the SWL in 1 m increments at a sampling frequency of 0.5 Hz. Using the vertically orientated SB-ADP, sea surface elevation was inferred from amplitude backscatter measurements at a sample rate of 4 Hz using image processing techniques. Results have been validated against an industry standard wave-measurement technique which is fully discussed in Sellar et al. (2018).

9.1.2 Flow characteristics

A 256 s flow sample measured during a flood tide at EMEC on the 22nd of November 2014 is considered. The measured D-ADP velocity data is interpolated in t and z to determine the U_x and U_z components incident on to each blade section for a given t. The channel depth $d = 45$ m, $z_0 = -27$ m and the rotor operates at $z \in [-18, -36]$ m. The, velocity readings incorporate the effects of waves, turbulence and the shear profile, but not velocities induced by the wake or the support structure of the turbine. Tower shadow effects due to the support structure are neglected in this study since the results from the previous chapter found that the load amplitude caused was an order of magnitude less than that due to moderate waves 2 m high with 5 s periods (see Figure 8.4).

The sample was selected on the basis of it containing an energetic wave train and to investigate the unsteady hydrodynamic response of the rotor. The waves, which

originate from the North Sea, are opposing the current. The free surface elevation (η) is measured at a fixed point in space directly above the turbine nacelle. The η time history is shown over 250 s in Figure 9.1(a). The significant wave height from the sample is 4.2 m and the maximum wave height observed is approximately 5 m with a wave period of 10 s. The wave steepness, defined as the product of wave amplitude and wave number is approximately 0.17, indicating that the wave is weakly non-linear. The power spectral density (S) of η, shown in Figure 9.1(b), confirms that the energy contained within this wave group is centred around an apparent wave period: $f_a = 0.095$ Hz. The time

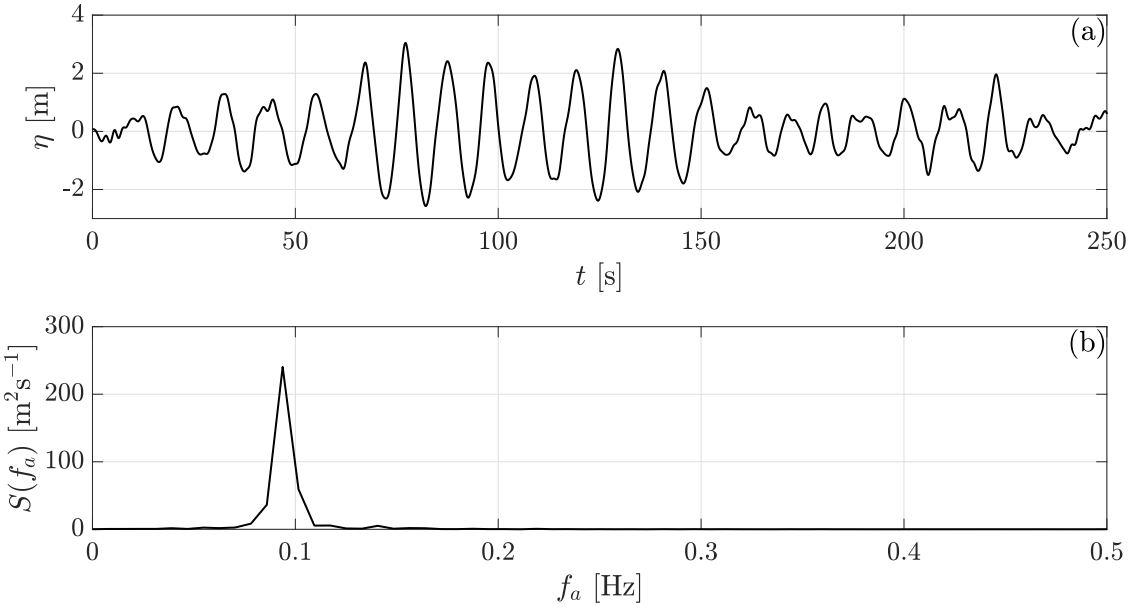

Figure 9.1: Free surface elevation (a) time history and (b) power spectrum density.

averaged U_x depth profile from 3 m above the bed ($z = -42$ m) to the SWL is shown in Figure 9.2, where each measurement in z are input at all values of y across the width of the rotor plane. The current velocity depth profile of U_x for $z \in [-18, -36]$ follows a power law with exponent 0.162, with a hub velocity of 2.70 ms^{-1}. The power spectral density of U_x is shown in Figure 9.3(a) for the blade tip at $z = -18$ m, $z_0 = -27$ m , and $z_0 = -36$ m. The peak frequency in the velocity spectrum at both $z = -18$ m and $z = -27$ m corresponds to the 0.095 Hz value found in the η spectrum. Towards the bed, from $z = -18$ m to $z = -27$ m, the energy peak associated with the wave decays by about 80%, and at $z = -36$ m the value has decreased by roughly 95%. The power spectral density of U_z is shown in Figure 9.3(b). As with U_x, the energy decreases with increasing depth and has a peak centred at the wave frequency. The fact that power spectral density of both U_x and U_z have peaks centred around the peak

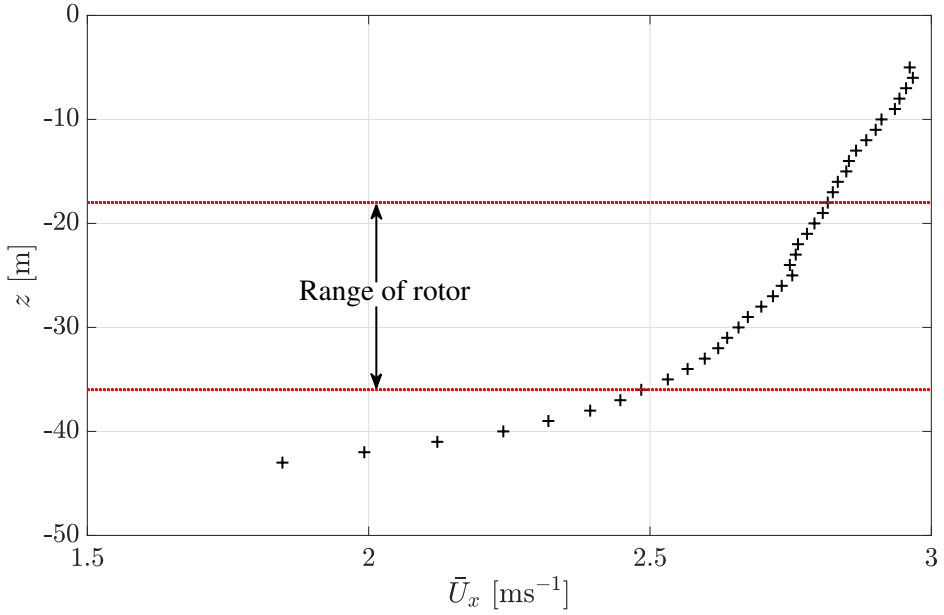

Figure 9.2: Time averaged depth profile of the streamwise velocity.

wave frequency confirms that the waves recorded above the turbine correlate well with the measurements taken $y = -40$ m away from the hub.

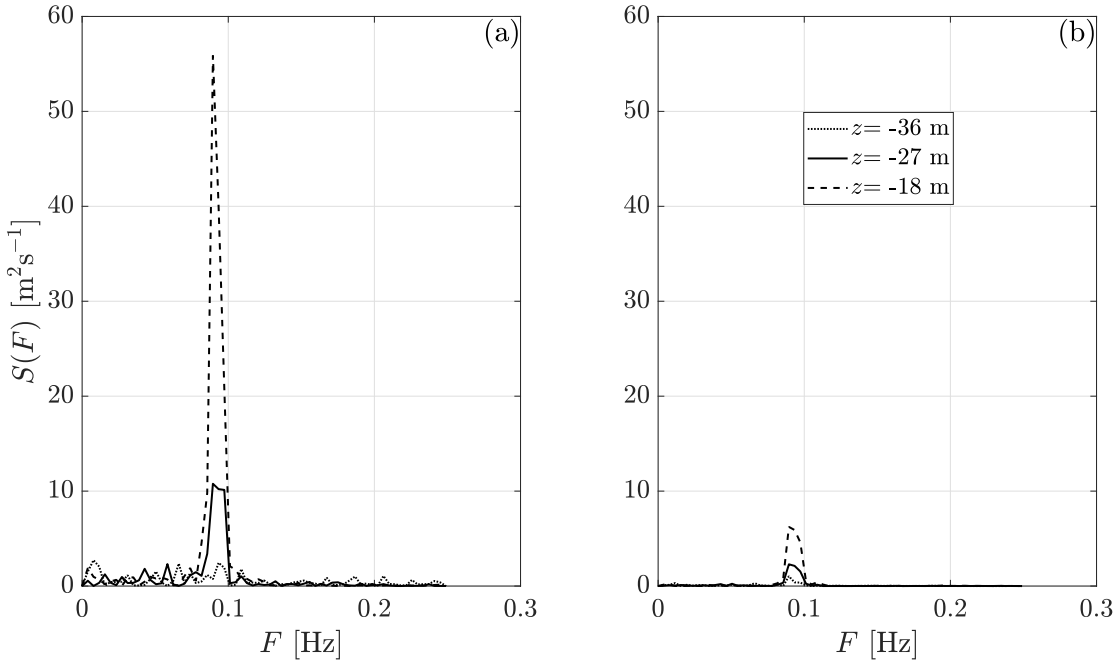

Figure 9.3: Power spectral density of (a) the streamwise velocity and (b) the vertical velocity encountered at the minimum ($z = -18$ m), hub ($z = -27$ m) and maximum ($z = -36$ m) depth ranges of the turbine blade.

The turbulent statistics cannot easily be computed from this time series because velocity fluctuations in the water column are so dominated by these large wave, which even at z_0 will be orders of magnitude greater than those caused by turbulence. However, referring to the turbulent spectra measured during negligible waves, shown in Figure 6.6, where $U_0 = 2.74\text{ms}^{-1}$, $I_x = 9\%$ and L_x =26.5 m, then it is reasonable to infer that the turbulent statistics are similar for the present data set, ignoring wave induced turbulence.

9.2 Rotor performance in a varying freestream

Here the difference in P and C_P of a rotor operating at variable and fixed speeds are reviewed and compared. A variable speed rotor adjusts its angular velocity Ω whilst keeping its tip-speed ratio λ constant, whereas a fixed speed rotor keeps Ω constant and λ varies. The considered parameters are: $U_x \in [1.5, 4.5]$ ms^{-1}, a variable speed with $\lambda = 4.5$ and a fixed speed with $\Omega = 1.25$ rads^{-1}. To enable a clear interpretation of the results, $C_D = 0$, $C_L = 2\pi\alpha$, a is assumed constant (0.3) and $a' = 0$, for all r. The results are shown in Figure 9.4. Observing the computed λ = constant values it is found that by varying Ω according to the onset velocity that $P \propto U_x^3$ and C_P remains constant. On the other hand, by keeping Ω fixed, as shown in Figure 9.4(a) $P \propto U_x^{2.71}$, which is a fit specific to these conditions. Even when such a large range of flow velocity is considered, the difference between the two curves is marginal. This important result suggests that if C_p is defined as in Equation 6.1 then the mean C_p is almost constant for any unsteady onset flow condition, even if the rotational speed is not adjusted to keep the optimal tip speed. One may have erroneously expected that, by fixing Ω, $P \propto U_x^2$.

For a constant Ω, from Equation 6.2 and Equation 6.3, $P \propto Q \propto F_{Tan}$. Then from Equation 3.2(b), with $C_D = 0$, F_{Tan} becomes:

$$F_{Tan} = \frac{1}{2} C_L \sin(\phi) \rho U_r^2 c, \tag{9.1}$$

therefore it would seem that $P \propto U_r^2 \propto U_x^2$. However, since $C_L \propto \alpha \propto U_x$, then $P \propto U_x^3$.

From Figure 9.4(b) by keeping Ω constant, the rotor does not operate constantly at the optimal λ, resulting in a marginal loss in performance, which is the reason why $P \propto U_x^{2.71}$. This is important for high frequency flow fluctuations where it would not be possible to match λ to $U_x(t)$ by constantly varying Ω.

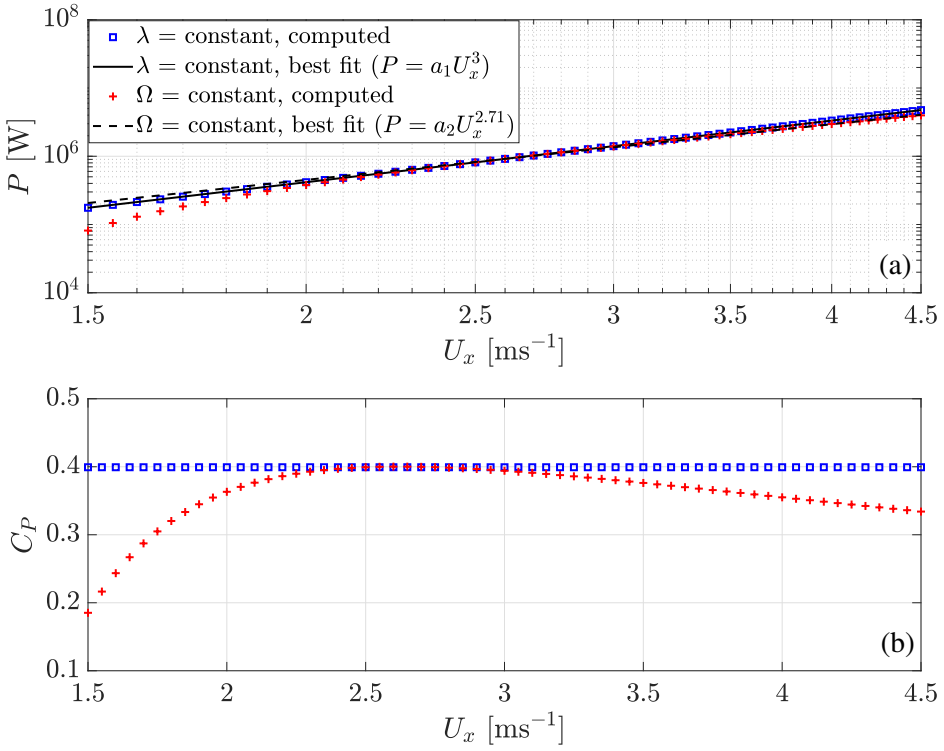

Figure 9.4: Comparison of variable and fixed speed rotor operation with freestream velocity: (a) power for varied rotational speed, (b) power generated for fixed speed rotation (c) power coefficient for varied rotational speed and (d) power coefficient for fixed speed rotation.

9.3 Power and thrust

The magnitude of U_x averaged over the swept area and the sample time period of 256 s is $\langle U_x \rangle = 2.72$ ms^{-1}, while the mean of the square $\sqrt{\langle U_x^2 \rangle} = 2.74$ ms^{-1} and the mean of the cube $\sqrt[3]{\langle U_x^3 \rangle} = 2.77$ ms^{-1}. The latter velocity is used for the steady simulation and to nondimensionalise forces, torque and power. The operating parameters λ and β_p, which yield a maximum C_P in a steady current with $U_0 = 2.77$ ms^{-1} are determined using the BEM model with static coefficients corrected for rotation. C_P is simulated for $\lambda \in [3, 6]$ in steps of 0.1, combined with $\beta_p \in [-10°, 10°]$ in steps of 0.1°. A peak $C_P = 0.47$ was found to occur for $\lambda = 4.5$ and $\beta_p = 0.1°$, with $C_T = 0.81$. All subsequent simulations are carried out using these operating parameters.

Values for C_P and C_T for both steady and unsteady conditions are shown in Figure 9.5 for ten rotational periods ($T_r = 4.5$ s). The unsteady fluctuations are dominated by an oscillation an oscillation slightly over $2T_r$, which, as shown in Figure 9.1, corre-

sponds to the peak wave period. There is no discernible contribution from turbulence or the rotational period. These fluctuations were found to exceed the steady value by up to 48% and 25% for C_P and C_T, respectively. Comparing the mean value of the unsteady time history (which is averaged over the full sample record) with the steady value reveals a power decrease of 3% and a thrust decrease of 3% from the steady-state. Here, the steady state result is computed with the same model used for the unsteady case but using a steady uniform onset flow.

To investigate what causes the mean power coefficient to decrease, additional simulations are performed where the model is gradually simplified. Firstly, a quasi-steady simulation is carried out without accounting for the load hysteresis, stall delay and dynamic stall, and using the static force coefficients from wind tunnel tests. Then, linear force coefficients are used, i.e. $C_L = 2\pi(\alpha - \alpha_0)$ and $C_D = 0$. Finally, a steady simulation in an ideal, steady, uniform flow with $U_0 = \sqrt[3]{\langle U_x^3 \rangle} = 2.77$ ms^{-1}, is performed. In total a 7% reduction is found from this latter steady ideal case to the fully unsteady mean value shown in Figure 9.5(a). This 7% loss can be broken down as follows. Firstly, the effect of an unsteady onset flow leads to a loss of 0.5%. As discussed in section 9.2, this can be avoided by operating the turbine at a constant tip-speed ratio rather than a constant rotational speed. Next, the presence of the drag and the non-linearity of the lift force due to the large excursion in the angles of attack which lead to flow separation, accounts for a further 6% reduction in the power coefficient. Finally, the unsteady effects (load hysteresis, stall delay and dynamic stall) lead to an additional 0.5% reduction. In conclusion, the unsteady phenomena have a small effect on the mean values, whose reduction in unsteady flow conditions is largely due to flow separation.

9.4 Root and edgewise bending moments

Time histories for C_{My} and the edgewise bending moment coefficient (C_{Mx}) are shown in Figures 9.6(a) and 9.6(b), respectively for the unsteady, steady and quasi-steady predictions. The mean unsteady predictions for C_{My} and C_{Mx} are reduced by 4.5% and 3%, respectively from the steady value and the fluctuations were found to exceed these by 45% and 65%, respectively. The unsteady and quasi-steady time histories have similar periodicity, however, a phase lag and on the most part, an amplitude reduction from the quasi-steady prediction is found. The mean values predicted by the

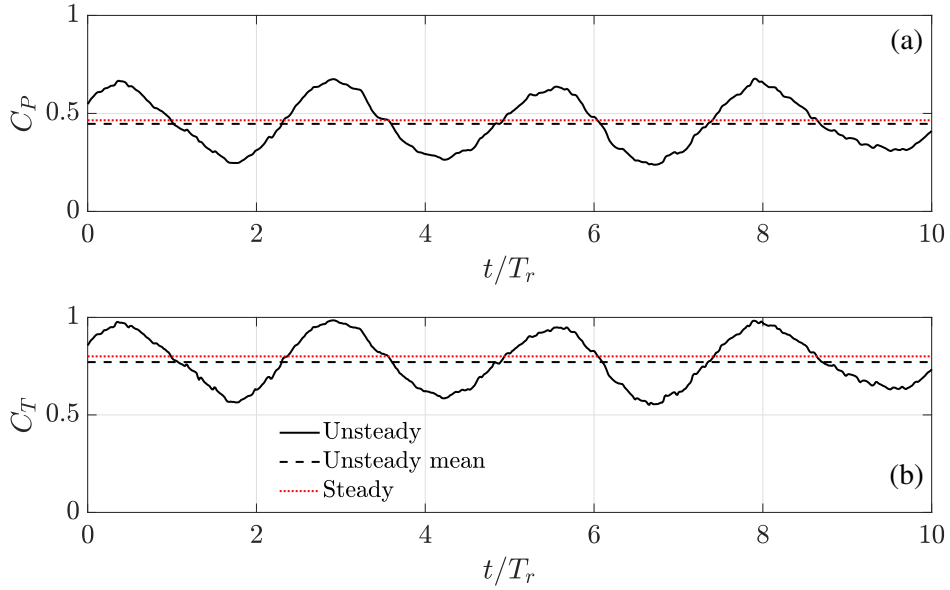

Figure 9.5: Comparison of (a) power coefficient and (b) thrust coefficient over 10 blade rotations, showing the predicted unsteady time history, and corresponding mean value alongside steady state response.

quasi-steady model for both coefficients are within 1% of the unsteady mean, which suggests that a quasi-steady assumption would be reasonable. However, it is important to note that the difference between the standard deviations is 15% higher for C_{My} and 5% for C_{Mx}. Thus the fatigue loads are moderately overpredicted using a quasi-steady approximation.

It is evident that large waves such as those considered here lead to large unsteady variations in the power, thrust and bending moment coefficients. However, there is little effect on the time averaged performance.

9.5 Time averaged sectional parameters

The difference between the unsteady and steady rotor performance is investigated by plotting the time averaged axial ($\bar{a}$) and tangential ($\bar{a}'$) induction factors along the blade span in Figures 9.7(a) and 9.7(b), respectively for the steady, quasi-steady and unsteady prediction. Firstly, there is no discernible difference between the unsteady and quasi-steady values anywhere along the blade, for either induction factor. Comparing the unsteady and steady predictions, a visible difference is evident inward from approximately $0.4R$ towards the root of the blade, where the steady value is larger for

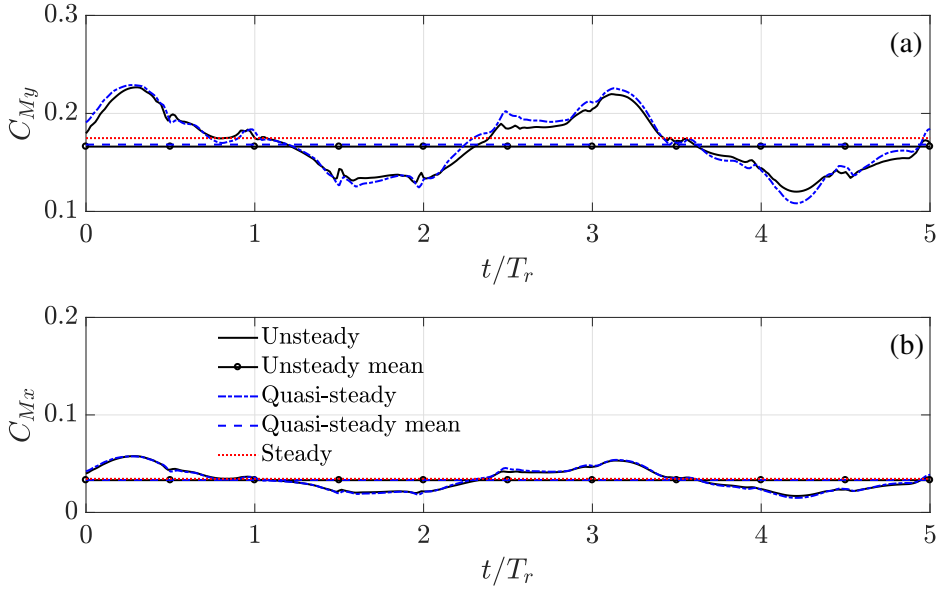

Figure 9.6: Blade bending moment time histories for (a) root bending and (b) edgewise bending shown over 5 blade rotations for steady, quasi-steady and unsteady predictions.

both factors. There is very little difference in the factors at the outer blade sections towards the tip, steady $\bar{a}$ is slightly larger and steady $\bar{a}'$ slightly smaller. Since the majority of the power is generated near the tip, the observed differences in C_P, C_T, C_{Mx}, and C_{My} from the steady state are not fully accounted for by the differences in $\bar{a}$ and $\bar{a}'$.

To investigate further the mean angle of attack $\bar{\alpha}$ along the blade is shown in Figure 9.8 for steady and unsteady conditions. A noticeable difference is evident between both values along the entire blade span. The difference is most prominent from $0.4R$ towards the root of the blade. This is due to the smaller $\bar{a}$ under unsteady conditions which is more favourable.

Time averaged, sectional values for lift ($\bar{C_L}$), drag ($\bar{C_D}$), thrust ($\bar{C_T}$) and torque ($\bar{C_Q}$) coefficients are shown in Figures 9.9(a-d), respectively, for the steady, quasi-steady and unsteady predictions. The quasi-steady values are determined using static wind tunnel data Janiszewska et al. (1996).

Inspecting Figure 9.9(a) the steady value of $\bar{C_L}$ is greater at the outer sections, where the flow is attached and lower at the inner sections where separation occurs, compared with the unsteady prediction. An increase in both the unsteady and quasi-steady value of $\bar{C_D}$ occurs near the blade root where the flow is highly separated, which will be discussed in the following section. However, from about $0.3R$, $\bar{C_D}$ follows the steady

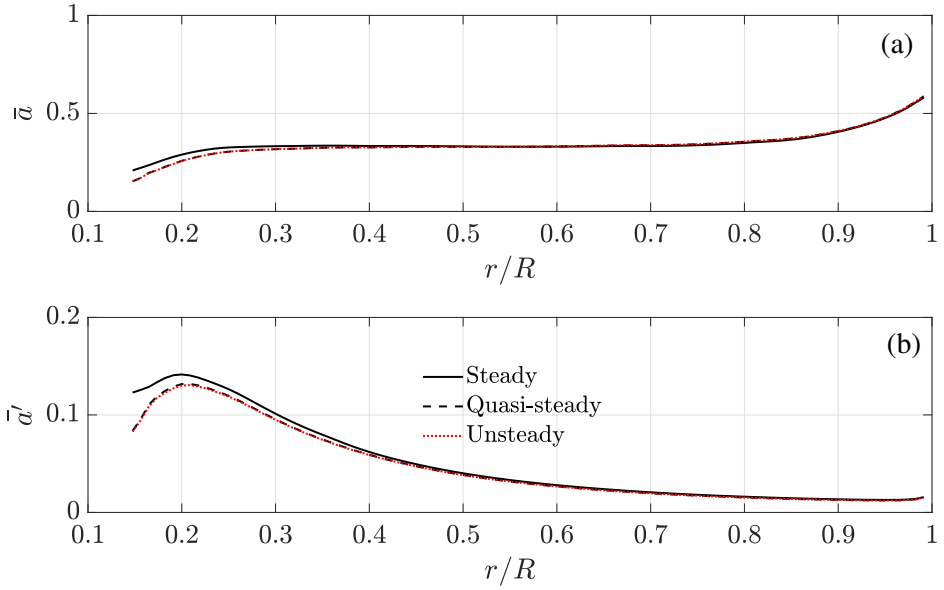

Figure 9.7: Time averaged (a) axial and (b) tangential induction factors along the blade span for steady, quasi-steady and unsteady predictions.

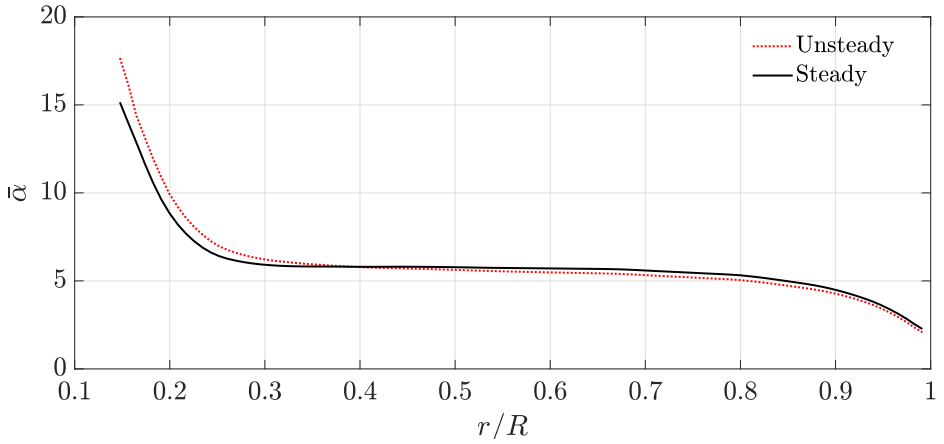

Figure 9.8: Time averaged angle of attack along the blade span for both steady and unsteady predictions.

value. As a consequence of the difference in $\bar{C_L}$, the unsteady value of $\bar{C_T}$ is reduced at the outer blade sections, which compounded with the higher dynamic pressure and longer moment arm at the tip, reduces the mean rotor thrust load. Likewise, unsteady $\bar{C_Q}$ is less from about $0.3R$ to R than in steady conditions, reducing the mean C_P value.

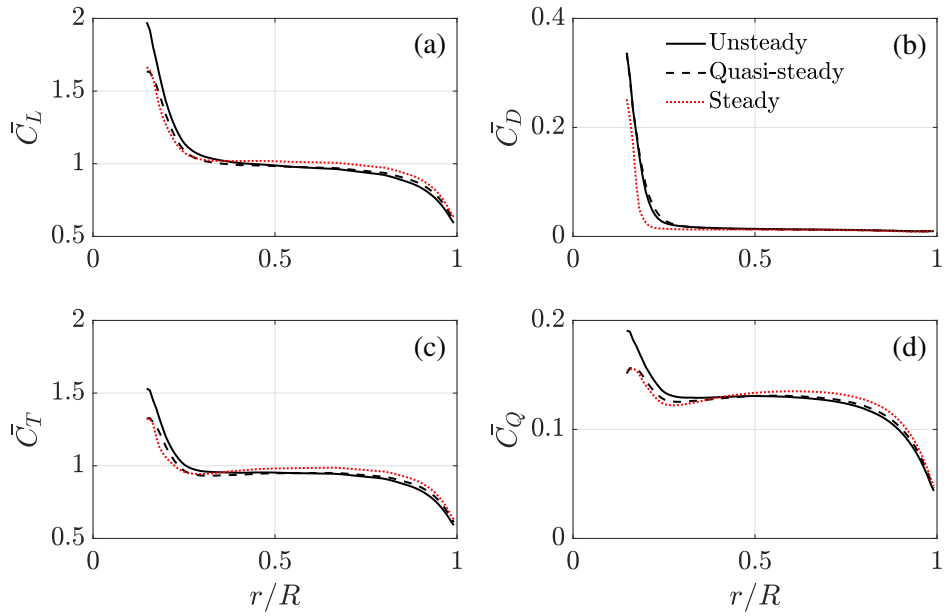

Figure 9.9: Comparison of mean (a) lift coefficient, (b) drag coefficient, (c) thrust coefficient and (d) torque coefficient along the blade span for steady, quasi-steady and unsteady conditions.

9.6 Unsteady flow along the blade span

Time histories for, U_r, f, α and C_L are shown in Figure 9.10 at locations $0.15R$, $0.4R$ and $0.96R$ on the blade. The first five periods of revolution are shown, which correspond to $t \in [0, 23]$s from Figure 9.1.

Near the tip ($0.96R$), the separation point is a constant and equal to unity, indicating that no separation occurs, which is confirmed by the moderate α fluctuations, which remain inside the attached flow region (-8° to 8°). The associated unsteady C_L is slightly below the quasi-steady value due to the shedding of vorticity from the trailing-edge, which causes a phase lag and amplitude reduction. At the mid-section ($0.4R$) the flow remains attached under steady and unsteady conditions. Moderate separation is evident for the quasi-steady case. The unsteady value of α is in excess of 8°. However, unsteady phenomena reduces the adverse pressure gradient in the boundary layer, causing a delay in separation from the quasi-steady value Ericsson and Reding (1988). The separation point near the blade root ($0.15R$) is a constant 0.7 under steady conditions. The unsteady mean value and amplitude for f is less than the quasi-steady value, indicating that highly non-linear phenomena are occurring. The α history shows that the oscillations are almost completely outside of the linear region. The instantaneous

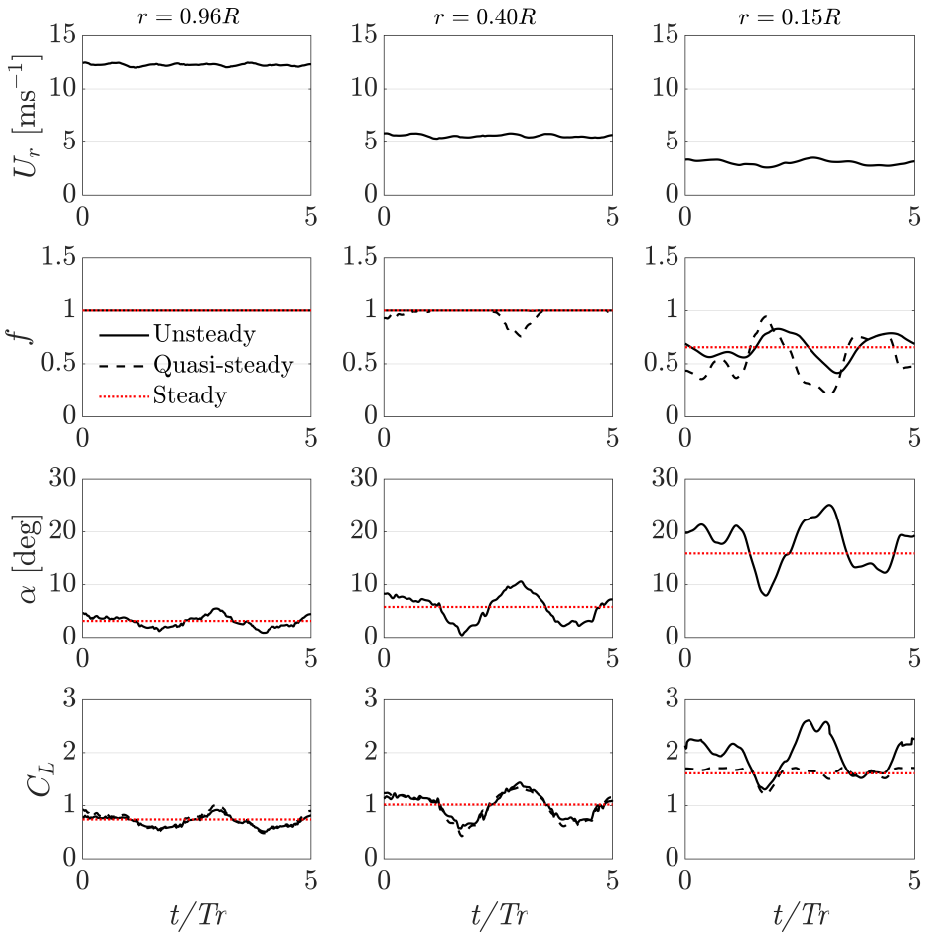

Figure 9.10: Time histories of the relative flow velocity, separation point, angle of attack and lift coefficient at blade sections near the tip ($r = 0.96R$), mid-section ($r = 0.40R$) and root ($r = 0.15R$).

C_L computed with the unsteady approach was up to 98% and 71% greater than that computed with a quasi-steady and a steady approach, respectively. The large unsteady C_L value is due to the formation and shedding of the leading-edge vortex.

Relationships between α, C_L and C_D are shown at the tip, mid-section and root in Figure 9.11 for $t \in [0, 12]$ s and Figure 9.12 for $t \in [120, 132]$ s, both of which encapsulate a full peak wave period. These plots show the nature of the hysteresis, which is mild at the tip where $k \approx 0.02$ where the flow is attached, the amplitude grows towards the middle of the blade where $k \approx 0.1$, hysteresis is not visible in C_L. However,

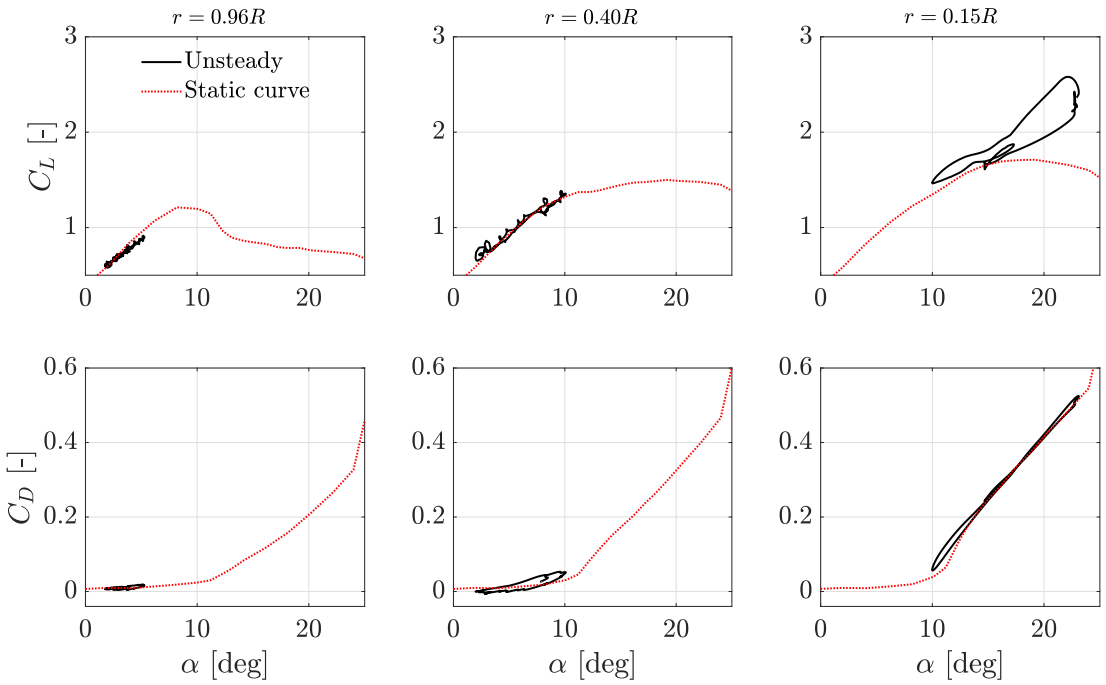

Figure 9.11: Unsteady lift and drag coefficients with angle of attack for locations near the tip ($r = 0.96R$), mid-section ($r = 0.40R$) and root ($r = 0.15R$) of the blade for $t \in [0, 12]$ s

it is evident in C_D. Moving toward the root, the flow is highly unsteady, $k \approx 0.3$ and the hysteresis is distinct. This large increase in the C_L above the quasi-steady value is caused by a vortex shedding from the leading-edge.

The build-up and transit of the leading-edge vortex as predicted by the model is illustrated in Figure 9.13 for the blade root section ($r = 0.15R$). The following description is given in terms of the time constants used to model the growth and transit of the LEV, which are fully described in section 5.3. At stage 1, $\alpha' > \alpha_{cr}$ inducing leading-edge separation, and initialising the vortex time parameter τ. At stage 2, α has increased causing a build-up in circulation at the leading-edge. At stage 3, the circulation has built up into a concentrated vortex which sheds and convects downstream resulting in a maximum vale of C_L when the vortex is directly above the centre of the foil, in addition a counter circulation has forming at the trailing-edge. At stage 4, $\tau = T_v$, and the leading edge vortex passes the trailing edge and breaks down; concurrently the trailing edge vortex sheds inducing full stall.

The location and duration of separation occurring on the blade is highly dependent on unsteady and rotational effects. In Figure 9.14 the locations along the blade

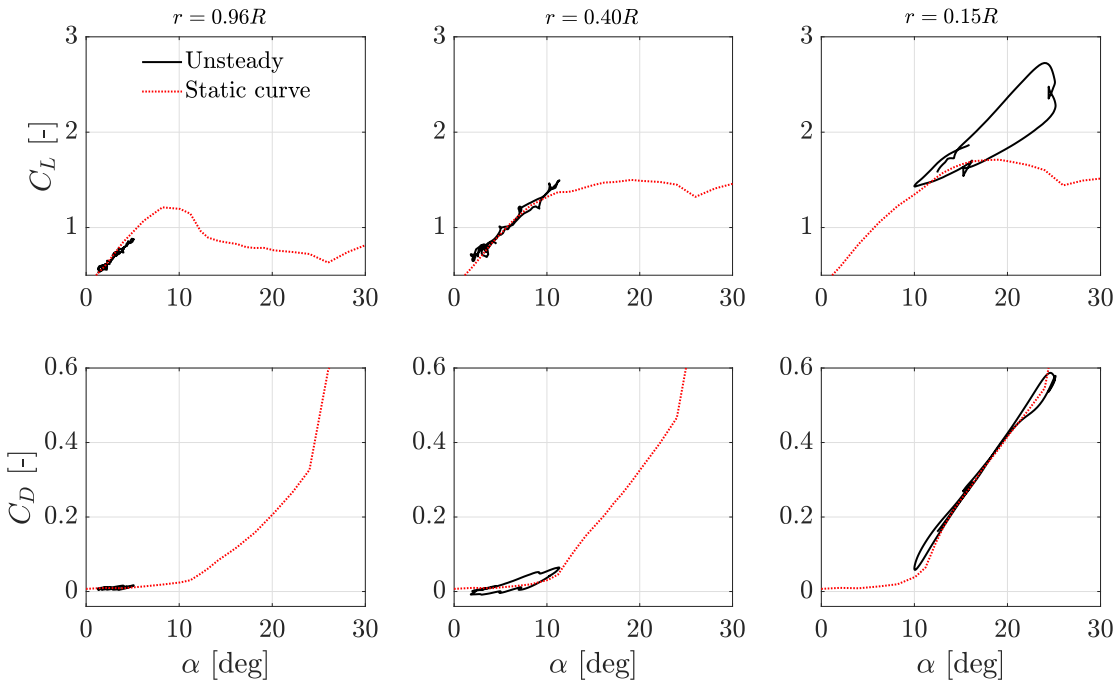

Figure 9.12: Unsteady lift and drag coefficients with angle of attack for locations near the tip ($r = 0.96R$), mid-section ($r = 0.40R$) and root ($r = 0.15R$) of the blade for $t \in [120, 132]$ s

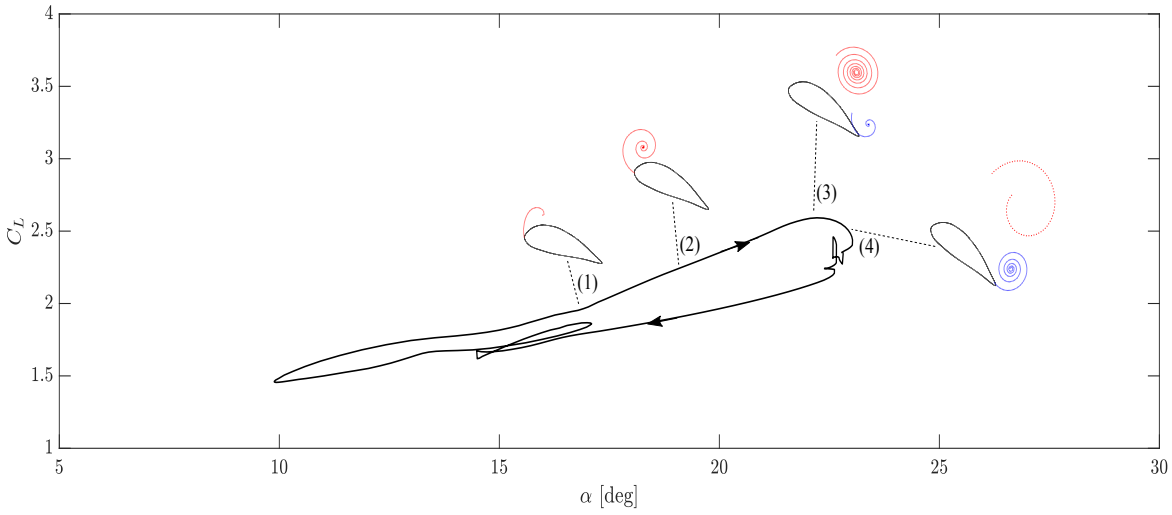

Figure 9.13: Lift coefficient hysteresis near the blade root for $t \in [0, 12]$ s. Showing the stages of leading-edge vortex formation and convection; (1) leading-edge separation occurs, (2) build up of circulation at the leading-edge, (3) leading-edge vortex sheds, (4) leading edge vortex passes trailing edge and trailing edge vortex sheds.

where separation occurs for (a) the rotational unsteady case, (b) the non-rotating unsteady case and (c) the rotational quasi-steady prediction. The contours represent the percentage of time that separation occurred. For the unsteady rotational case separation is mostly restricted to the very root of the blade where a minimum $f \approx 0.5$ occurs roughly 10% of the time. Significantly, full separation does not occur. For the unsteady non-rotating case separation is also confined to root sections. However, the point of separation moves closer to the leading edge with full separation almost occurring up to 30% of the time. For the quasi-steady prediction separation is observed over a greater portion of the blade, albeit near the trailing edge. Since the flow is mostly attached

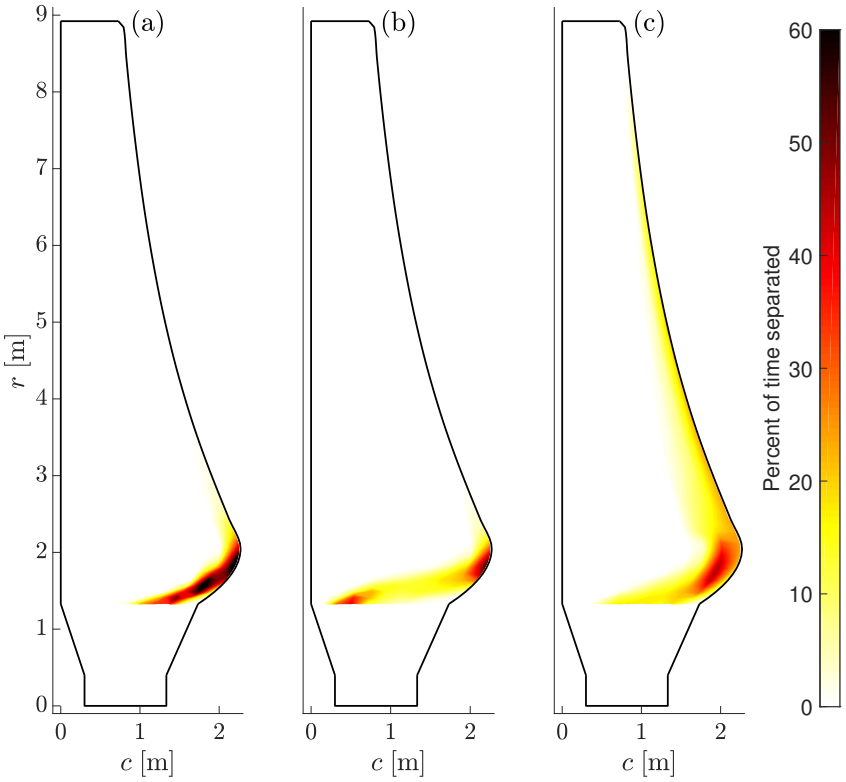

Figure 9.14: Location and duration in percentage of separation occurring along the blade span for (a) including unsteady and rotational, (b) only unsteady and (c) quasi-steady with rotation.

over the blade, there is an overall amplitude reduction from the quasi-steady lift value (Theodorsen's theory). Which explains the reduced standard deviations for the root and edgewise bending moment coefficients compared to the quasi-steady prediction (see Root and edgewise bending moments, Section 8.2). The large overshoots occurring near the root, where the flow is heavily separated has a negligible effect due to the short

moment arm, and lower relative velocity.

9.7 Sub-optimal operating conditions

The analysis so far has assumed that the optimal $\lambda = 4.5$ is always met. However, in reality, it will be difficult for the rotor to always rotate at the optimum speed to match the time dependent inflow. In this section an investigation into how the flow along the blade span and the root bending moment coefficient are effected by a reduced rotor speed causing $\lambda = 4$ and $\lambda = 3.5$, where the pitch angle which yields maximum C_P for each is $\beta_p = 0.2°$ and $\beta_p = 1.2°$, respectively. As discussed in section 8.5 a rotor without a pitch control actuator may use underspeed (reduce the rotor speed) to shed power, which, in turn, will reduce λ. In Figures 9.15(a) and 9.15(b) the cases of $\lambda = 4$ and $\lambda = 3.5$ are shown, respectively, over 10 periods of revolution. For $\lambda = 4$ a clear

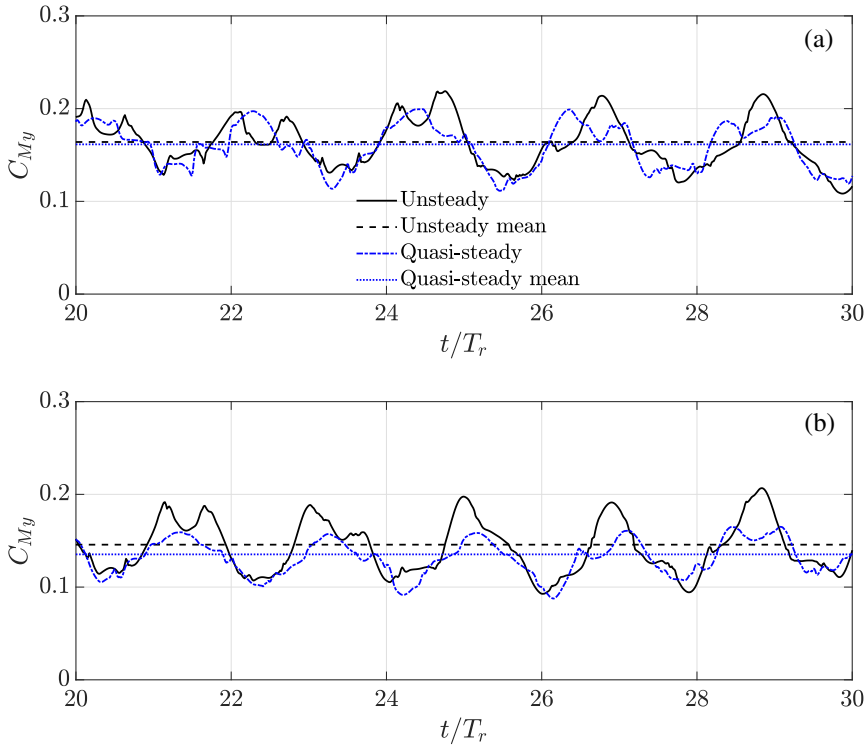

Figure 9.15: Root bending moment coefficient for (a) tip-speed ratio $\lambda = 4$ and (b) $\lambda = 3.5$.

differences are observed in the phase and peak values where the quasi-steady prediction was found to be as much as 30% below the unsteady fluctuating value throughout the

full time series. There is also a small 2% reduction in the quasi-steady mean value. For the $\lambda = 3.5$ case, the quasi-steady prediction is very poor. A maximum difference of 80% from the unsteady value occurs and the mean value is underpredicted by 8% which is significant.

The quasi-steady prediction is poor at lower values of λ because the flow around the blade undergoes large periods of separation. Shown in Figure 9.16 is the unsteady prediction (a) and the quasi-prediction (b). Clearly the flow is largely separated over most of the blade span for the unsteady case, thus dynamic stall is also occurring at most span locations, and moreover, the model predicts vortex shedding all the way up from the root to $0.5R$ of the span. Because a large proportion of the blade is undergoing dynamic stall, unlike the optimum $\lambda = 4.5$ case, there is a global effect which causes the peaks in C_{M_y} shown in Figure 9.15(b). For the quasi-steady prediction separation occurs over almost the entire span, and at some mid-span locations the flow is observed to be approximately two thirds separated ($f \approx 0.33$) for 10% of the time.

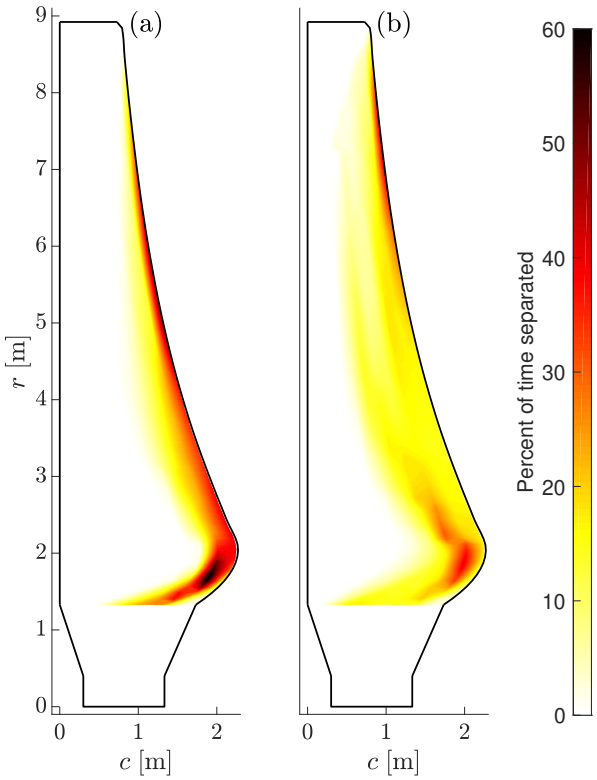

Figure 9.16: Location and duration in percentage of separation occurring along the blade span for (a) unsteady and (b) quasi-steady predictions.

9.8 Discussion and summary of results

A summary of the key results from this chapter are herein given along with a brief discussion.

A study of large realistic wave conditions was carried out using velocity measurements made at the EMEC test site, where the mean current was 2.72 ms^{-1}. The waves have a maximum height of approximately 5 m, steepness of 0.17 and a dominant frequency of 0.095 Hz.

The unsteady loads are governed by the frequency of the waves. Even at a hub depth of 27 m, the free stream velocity fluctuations are dominated by the wave frequency.

The mean unsteady forces and bending moments computed with the unsteady model are within ca. 1% of those predicted using a quasi-steady approximation. However, the standard deviation of the root and edgewise bending moments are overpredicted by 15% and 5%, respectively. This is due to lift amplitude reduction (Theodorsen's theory), which occurs under unsteady attached flow conditions. Under these optimal operating conditions, a reasonable quasi-steady approximation of the unsteady loadings can be achieved. These findings agree with Galloway et al. (2014) who determined that dynamic stall may be neglected. However, reducing the rotor speed, such that the turbine operates at sub-optimum tip-speed ratios, increases flow separation and dynamic stall occurs over most of the blade. This concurs with the findings of Milne et al. (2013a) who showed that dynamic stall can dominate the blade loading at lower tip-speed ratios. At a tip-speed ratio of 3.5, the maximum root bending moment coefficient was almost twice that predicted using a quasi-steady approximation. Clearly, load fluctuations are significantly under-predicted by the quasi-steady approach in this region.

For turbines which control power through stall regulation. It is recommended that an unsteady model is used to predict the loads a blade may encounter during power control. However, if the turbine employs a pitch mechanism and yaw drive, or the turbine operates at higher λ, then it is likely that a quasi-steady model will predict the loads to a reasonable accuracy.

Chapter 10

Conclusions

10.1 Conclusions and research accomplishments

A better understanding of the unsteady loads encountered by a full-scale tidal turbine blade will aid the future development of tidal power. In response a model has been developed to quantify the unsteady loads on an axial-flow tidal turbine. The model accounts for load hysteresis, dynamic stall, leading-edge vortex shedding and rotational augmentation. A novel method of coupling dynamic stall with rotational augmentation has been presented. The induction factors are computed with blade-element momentum theory, based on a running average of the loads from the previous period of revolution. The model has been validated using tank-scale measurements of the root bending moment during waves, turbulence, tower shadow and sheared current. The difference between the mean and standard deviation values were within 1% and 3%, respectively, demonstrating that the model is capable of predicting the root bending moment for a model scale turbine to a reasonable accuracy. The code is freely available for use and can be downloaded from the authors GitHub repository (Scarlett and Viola, 2017). Using the model a parameter study of the unsteady loads, for a range of unsteady flow conditions, encountered by an 18 m diameter, 1 MW, commercial-scale tidal turbine blade has been carried out. Then the performance of the turbine during large waves is assessed using measured onset flow velocities as an input to the model. It is envisaged that the results will inform designers of the governing loads which are important for fatigue analysis. This will enhance the durability of tidal turbine blades without over-engineering them. In addition, the results reveal under which conditions simple, low-cost modelling approaches can be applied. These will, in turn, reduce the

levelised cost of tidal energy, making the sector more commercially viable.

The research questions raised in section 1.6 have been addressed as follows:

(a) The most significant load fluctuations, parametrised by the blade root bending moment, are caused by large waves which follow the current, and that the peak blade root bending moment is further increased when combined with turbulence.

(b) Near the blade root large waves or a yaw misalignment can elicit lift coefficients twice the median value due to deep dynamic stall, where vortex shedding occurs. Added mass effects mostly attenuate the lift amplitude for the range of reduced frequencies in which tidal turbines operate. Shed vorticity from returning and neighbouring wakes of other blades cause a slight increase in the lift amplitude for lower reduced frequency values.

(c) In terms of the importance of modelling the unsteady loads on a tidal turbine. This is specific to the operating conditions and power control mechanism. For turbines which control power through stall regulation. It is recommended that an unsteady model is used to predict the loads a blade may encounter during power control. However, if the turbine employs a pitch mechanism and yaw drive, or the turbine operates at higher tip-speed ratios, then it is likely that a quasi-steady model will predict the loads to a reasonable accuracy.

The following conclusions are valid for any tidal turbine geometry operating up to the rated velocity for maximum power:

- Turbulence, waves or yaw misalignment can lead to load peaks which are twice the median value.
- At the outer blade sections, the flow is attached and unsteady phenomena results in a reduction of the mean sectional lift. Towards the mid-section, a delay in flow separation occurs. Near the blade root, dynamic stall and leading-edge vortex shedding cause a twofold increase of the sectional lift compared to the static value.
- The most significant root bending moment amplitudes, for a fixed blade pitch angle, are produced by large ($H > 2$ m), long period waves ($T_a > 5$ s) which follow the current, and that the amplitude is further increased when combined with turbulence ($I_x > 10\%$). In comparison, loadings induced by the blade rotating through tower shadow and the shear layer are negligible.

- A yaw misalignment leads to larger fluctuations and a lower median value which in turn reduces the peak load. Locally, yaw induces extreme lift coefficients at the root of the blade. However, when dimensions are considered, the thrust force, which is normal to the blade, is larger at the tip than at the root.

- Below a critical reduced frequency of 0.56, the added mass effects damp the total response, but above this value significant load fluctuations can occur. Such events are confined to blade sections near the root during high frequency oscillations in angle of attack. Turbines operating at high tip-speed ratios are unlikely to encounter added mass effects due to the greater onset velocity.

- Flow separation is most prevalent with waves, leading to light dynamic stall (i.e. periodic trailing edge separation) over a large region of the blade. However, deep dynamic stall occurs for all flow combinations near the hub of the blade.

The findings which are specific to the turbine geometry studied here are:

- Extreme waves ($H > 5$ m) dominate over extreme turbulence ($I_x > 15\%$).

- The largest thrust force occurs at the mid-section of the blade during large waves and turbulence.

- Large yaw angles ($\gamma > 30°$), low tip-speed ratios ($\lambda < 4$) and very large waves ($H > 5$ m) elicit overshoots in the time averaged blade root bending moment compared to the quasi-steady prediction. This indicates that dynamic stall is having a global affect.

- If the power is regulated by fixing the rotational speed and pitching the blades to feather, then the effect of a yaw misalignment becomes even more critical. In these conditions, the region affected by dynamic stall extends to half of the blade span.

The findings which have implications for future design practice are:

- The mean power and thrust, as well as the mean root and edgewise bending moments, show a moderate reduction of less than 5% compared to the steady state. This is largely due to flow separation. However, both the fact that the rotor is operating at fixed rotational speed, and unsteady phenomena, occurring near the tip, make a minor contribution. The extreme loads predicted near the

blade root caused by dynamic stall have little effect on the global thrust and torque acting on the blade due to the short lever arm and lower relative flow velocity compared to the outer sections. These results show that large waves induce significant load fluctuations. However, there is little effect on the mean loads and performance of the turbine which confirm the observations of Galloway et al. (2014).

- Overall, fluctuations in the root bending moment and power were found to exceed the steady values by almost 50%.

- The mean unsteady forces and bending moments computed with the unsteady model are within ca. 1% of those predicted using a quasi-steady approximation. However, the standard deviation of the root and edgewise bending moments are overpredicted by 15% and 5%, respectively. This is due to lift amplitude reduction (Theodorsen's theory), which occurs under unsteady attached flow conditions. Under these optimal operating conditions, a reasonable quasi-steady approximation of the unsteady loadings can be achieved. These findings agree with Galloway et al. (2014) who determined that dynamic stall may be neglected. However, reducing the rotor speed, such that the turbine operates at sub-optimum tip-speed ratios, increases flow separation and dynamic stall occurs over most of the blade. This concurs with the findings of Milne et al. (2013a) who showed that dynamic stall can dominate the blade loading at lower tip-speed ratios.

- When operating at a sub-optimum tip-speed ratio of 3.5 during large ($H = 5$ m), long period waves ($T_a = 10$ s), the maximum root bending moment coefficient was almost twice that predicted using a quasi-steady approximation. Clearly, load fluctuations are significantly under-predicted by the quasi-steady approach in this region.

These results have shown that turbulence, waves or yaw misalignment can lead to extreme load peaks. Moreover, low tip-speed ratios, as well as large yaw misalignment can cause the mean root bending moment to overshoot the mean value predicted by a quasi-steady approximation. For these reasons it is advisable that unsteady phenomena are always considered in the assessment of both the instantaneous and time-averaged loads on a turbine.

10.2 Recommendations for future work

10.2.1 Model improvements

There are a number of limitations to the model. Perhaps the most significant is the lack of spatial coherence in the turbulent fluctuations, such that the same fluctuation is experienced on all blade sections in time. There is a lack of spatial correlations for tidal channel turbulence, however, these do exist for atmospheric turbulence. Spatial coherence can be implemented into the present model by computing the cross spectra in three dimensions. The implementation of such a method could be optimised by considering only the rotationally sampled turbulence (see Veers, 1988).

Wake effects are only considered through trailing edge vortex shedding, which results in an amplitude reduction in the attached flow regime (Theodorsen's theory), however, sampling of returning and neighbouring wakes is not accounted for in the general model, although it was quantified using Loewy's theory, and found to be small for the turbine considered here. However, for turbines which rotate faster, or operate in lower current velocities, wake sampling is likely to be more prevalent. The effect can be modelled using potential flow vortex methods, however, combining such a model with the present dynamic stall implementation would be challenging. Doing so would also enable the wake distortion affect to be accounted for on the turbulent fluctuations which is also not presently captured.

The model is limited to creating directional regular waves. Implementation of irregular waves could be carried out using a similar method as that used to make a turbulent time series. A number of regular waves could be generated from a spectrum with random phases applied. Lastly, the model has assumed that waves and turbulence can be combined linearly. It would be interesting to study from field data how the depth decay of the wave orbitals are affected by turbulence and then to implement a physical model to investigate the significance of this for the unsteady loadings.

10.2.2 Application of the model

The author hopes that the proposed model will now be used for fatigue analysis. Considering that a tidal turbine is always operating in unsteady flow. It would be very interesting to discover whether the fatigue life is shortened by the inclusion of the unsteady phenomena discussed in this thesis.

Comparison of the proposed model with load data from a full-scale device would

further validate the model and aid improvements. To date it has not been possible to obtain the turbine data acquired during the ReDAPT project. This is unfortunate since the combination of load data with corresponding flow measurement could enhance modelling techniques.

The unsteady load model could be expanded in a number of ways. Floating tidal turbines are now a very attractive proposition due to the ease of installation and accessibility. However, the unsteady hydrodynamics become a function of how much the structure moves with the fluid. It would be useful to couple this fluid structure interaction so that floating tidal turbines could be considered. An additional reason is that turbines employing flexible/deformable blades could also be analysed.

Dynamic stall modelling is off-putting to designers due the requirement of a number of empirical parameters which describe the time lags under unsteady conditions. Something which would make dynamic stall modelling more accessible would be a way of predicting these parameters if the user does not have them. The present model could be made more universal by giving the user the option of extrapolating or learning the empirical time constants. A number of databases of dynamic stall measurements exists for a range of aerofoil profiles operating across a range of flow conditions. A valuable PhD project would be to collect such data and implement a neural network algorithm to learn the time constants and develop a tool to predict them for different geometries and perhaps even extending to Reynolds number and reduced frequency variability.

Investigate more tide and site specific turbulence conditions, for instance the turbulence statistics can depend on the tidal cycle and local geometrical features may give rise to gust which may reach the hub of the turbine. One way to model such flow conditions would be to couple the model with a flow field computed using a Navier-Stokes solver.

The results could be expanded by investigating active pitch control. The present work focused on pitching the blade due to a change in the mean flow so as to maintain a constant power, however, a pitch mechanism which follows the flow fluctuations could be investigated to optimise both load alleviation and power output.

A wider range of turbine geometries should be investigated. This work was constrained by there being only one source in the literature which provides the geometry of a full-scale blade (Gretton, 2010). In addition this analysis assumed that the blades have smooth leading edges, whereas in reality they are likely to undergo bio-fouling which will alter the lift and drag coefficients. It would be interesting to evaluate how bio-fouling alters the unsteady loads.

Appendices

A Numerical solution to the indicial load response

Assuming the indicial response takes the exponential form given in Equation 4.10 then C_L^c given by Equation 6.8 can be solved using a recurrence relation and a simple finite difference scheme for the temporal derivative inside the Duhamel integral as described in this section.

Inserting Equation 4.10 inside Equation 6.8 gives the following expression

$$\begin{aligned}\alpha_E(s) &= 2\pi\Big(\alpha(0)(1 - A_1e^{-b_1 s} - A_2e^{-b_2 s}) + \int_0^s \frac{\mathrm{d}\alpha(\sigma)}{\mathrm{d}s}\Big(1 - A_1e^{-b_1(s-\sigma)} - A_2e^{-b_2(s-\sigma)}\Big)\mathrm{d}\sigma\Big) \\ &= \alpha(0) - A_1\alpha(0)e^{-b_1 s} - A_2\alpha(0)e^{-b_2 s} + \int_0^s \mathrm{d}\alpha(s) - A_1\int_0^s \frac{\mathrm{d}\alpha}{\mathrm{d}s}(\sigma)e^{-b_1(s-\sigma)}\mathrm{d}\sigma \\ &\quad - A_2\int_0^s \frac{\mathrm{d}\alpha}{\mathrm{d}s}(\sigma)e^{-b_2(s-\sigma)}\mathrm{d}\sigma.\end{aligned} \tag{1}$$

Neglecting $A_1\alpha(0)e^{-b_1 s}$ and $A_2\alpha(0)e^{-b_2 s}$ since they are short term transients, Equation 1 can be rewritten as

$$\alpha_e(s) = \alpha(s) - X(s) - Y(s), \tag{2}$$

where

$$X(s) = A_1\int_0^s \frac{\mathrm{d}\alpha}{\mathrm{d}s}(\sigma)e^{-b_1(s-\sigma)}\mathrm{d}\sigma, \tag{3}$$

and

$$Y(s) = A_2\int_0^s \frac{\mathrm{d}\alpha}{\mathrm{d}s}(\sigma)e^{-b_2(s-\sigma)}\mathrm{d}\sigma. \tag{4}$$

Evaluating Equation 3 at the next time step $s + \Delta s$ gives

$$\begin{aligned} X(s+\Delta s) &= A_1 \int_0^{s+\Delta s} \frac{\mathrm{d}\alpha}{\mathrm{d}s}(\sigma) e^{-b_1(s+\Delta s-\sigma)} \mathrm{d}\sigma \\ &= A_1 e^{-b_1 \Delta s} \int_0^{s} \frac{\mathrm{d}\alpha}{\mathrm{d}s}(\sigma) e^{-b_1(s-\sigma)} \mathrm{d}\sigma + A_1 \int_s^{s+\Delta s} \frac{\mathrm{d}\alpha}{\mathrm{d}s}(\sigma) e^{-b_1(s+\Delta s-\sigma)} \mathrm{d}\sigma \\ &= X(s) e^{-b_1 \Delta s} + A_1 \int_s^{s+\Delta s} \frac{\mathrm{d}\alpha}{\mathrm{d}s}(\sigma) e^{-b_1(s+\Delta s-\sigma)} \mathrm{d}\sigma \\ &= X(s) e^{-b_1 \Delta s} + I. \end{aligned} \tag{5}$$

Equation 5 is recursive since the previous value $X(s)$ is evaluated alongside the new increment I, at the new time period. Bringing constant values outside of the integral the expression for I becomes

$$\begin{aligned} I &= A_1 \int_s^{s+\Delta s} \frac{\mathrm{d}\alpha}{\mathrm{d}s}(\sigma) e^{-b_1(s+\Delta s-\sigma)} \mathrm{d}\sigma, \\ &= A_1 e^{-b_1(s+\Delta s)} \int_s^{s+\Delta s} \frac{\mathrm{d}\alpha}{\mathrm{d}s}(\sigma) e^{b_1 \sigma} \mathrm{d}\sigma. \end{aligned} \tag{6}$$

The next step is the introduction of a differencing scheme. Making the following backwards approximation

$$\frac{\mathrm{d}\alpha}{\mathrm{d}s} = \frac{\alpha(s+\Delta s) - \alpha(s)}{\Delta s}, \tag{7}$$

then the remainder of the integral can be evaluated analytically

$$\int_s^{s+\Delta s} e^{b_1 \sigma} \mathrm{d}\sigma = \frac{\left(e^{b_1 \Delta s} - 1\right) e^{b_1 s}}{b_1}. \tag{8}$$

Putting everything together the expression for the new increment becomes

$$\begin{aligned} I &= A_1 e^{-b_1(s+\Delta s)} \Big(\frac{\alpha(s+\Delta s) - \alpha(s)}{\Delta s} \frac{\left(e^{b_1 \Delta s} - 1\right) e^{b_1 s}}{b_1} \Big), \\ &= A_1 \Big(\frac{\alpha(s+\Delta s) - \alpha(s)}{\Delta s} \Big) \Big(\frac{1 - e^{-b_1 \Delta s}}{b_1} \Big), \end{aligned} \tag{9}$$

and Equation 5 becomes

$$X(s+\Delta s) = X(s) e^{-b_1 \Delta s} + A_1 \Big(\frac{\alpha(s+\Delta s) - \alpha(s)}{\Delta s} \Big) \Big(\frac{1 - e^{-b_1 \Delta s}}{b_1} \Big), \tag{10}$$

then the previous time step is

$$X(s) = X(s - \Delta s)e^{-b_1 \Delta s} + A_1\Big(\frac{\alpha(s) - \alpha(s - \Delta s)}{\Delta s}\Big)\Big(\frac{1 - e^{-b_1 \Delta s}}{b_1}\Big), \tag{11}$$

and similarly

$$Y(s) = Y(s - \Delta s)e^{-b_2 \Delta s} + A_2\Big(\frac{\alpha(s) - \alpha(s - \Delta s)}{\Delta s}\Big)\Big(\frac{1 - e^{-b_2 \Delta s}}{b_2}\Big). \tag{12}$$

Equation 11 and Equation 12 are one-step recursive formulae that give the new value $\alpha_E(s)$.

Bibliography

Abbott, I. H. and Albert Edward Von Doenhoff (1959). *Theory of wing sections, including a summary of airfoil data*.

Adcock, T. A. A., Draper, S., Houlsby, G. T., Borthwick, A. G. L., and Serhadlioglu, S. (2013). The available power from tidal stream turbines in the Pentland Firth. *Proceedings of the Royal Society A: Mathematical, Physical and Engineering Sciences*, 469(2157):20130072–20130072.

Afgan, I., McNaughton, J., Rolfo, S., Apsley, D. D., Stallard, T., and Stansby, P. (2013). Turbulent flow and loading on a tidal stream turbine by LES and RANS. *International Journal of Heat and Fluid Flow*, 43:96–108.

Ahmed, U., Apsley, D. D., Afgan, I., Stallard, T., and Stansby, P. K. (2017). Fluctuating loads on a tidal turbine due to velocity shear and turbulence: Comparison of CFD with field data. *Renewable Energy*, 112:235–246.

Airy, G. (1841). *Tides and waves*. London.

Arnold, M., Biskup, F., and Cheng, P. W. (2016). Load reduction potential of variable speed control approaches for fixed pitch tidal current turbines. *International Journal of Marine Energy*, 15:175–190.

Atlantis Resources Ltd (2016). SeaGen brochure. Technical report.

Babinsky, H. (2003). How do wings work? *Physics Education*, 38(6):497.

Barltrop, N., Varyani, K., Grant, A., Clelland, D., and Pham, X. (2007). Wave-current interactions in marine current turbines. *Proc. IMechE Part A: J. Power and Energy*, 221:233–242.

Batcherlor, G. K. and Proudman, I. (1954). The effect of rapid distortion of a fluid in turbulent motion. *The Quarterly Journal of Mechanics and Applied Mathematics*, 7(1):83–103.

Beddoes, T. S. (1978). Onset of leading edge separation effects under dynamic conditions and low Mach number. In *Proceedings of the 34th annual forum of the American helicopter society*.

Beddoes, T. S. (1993). A third generation model for unsteady aerodynamics and dynamic stall. Technical report, Westland Helicopters Limited.

Bergami, L., Gaunaa, M., and Heinz, J. (2013). Indicial lift response function: an empirical relation for finite-thickness airfoils, and effects on aeroelastic simulations. *Wind Energy*, 16(5):681–693.

Bisplinghoff, R. L., Holt, A., and Halfman, R. L. (1996). *Aeroelasticity*. Dover Publications Inc.

Black and Veatch (2005a). Phase I. UK tidal stream energy resource assessment. *Carbon Trust Marine Energy Challenge*.

Black and Veatch (2005b). Phase II. UK tidal stream energy resource assessment. *Carbon Trust Marine Energy Challenge*.

Blackmore, T., Myers, L. E., and Bahaj, A. S. (2016). Effects of turbulence on tidal turbines: Implications to performance, blade loads, and condition monitoring. *International Journal of Marine Energy*, 14:1–26.

Bossanyi, E. (2012). GL Garrad Hassan Tidal Bladed Theory Manual. Technical report.

Brent, R. and Burkardt, J. (2002). Algorithms for minimization without derivatives.

Breton, S.-P., Coton, F. N., and Moe, G. (2008). A study on rotational effects and different stall delay models using a prescribed wake vortex scheme and NREL phase VI experiment data. *Wind Energy*, 11(5):459–482.

Buhl, M. L. (2005). A new empirical relationship between thrust coefficient and induction factor for the turbulent windmill state. Technical Report August.

Burton, T., Jenkins, N., Sharpe, D., and Bossanyi, E. (2011). *Wind Energy Handbook*. John Wiley & Sons, Ltd, Chichester, UK.

Butterfield, C. P., Hansen, A. C., Simms, D., and Scott, G. (1991). Dynamic stall on wind turbine blades. Technical report, National Renewable Energy Lab., Golden, CO (United States).

Carlier, C., Pinon, G., Gaurier, B., Germain, G., and Rivoalen, E. (2015). A Synthetic-Eddy-Method to represent the ambient turbulence in numerical simulation of marine current turbine. In *11th European Wave and Tidal Energy Conference (EWTEC)*.

Carr, L. W. (1988). Progress in analysis and prediction of dynamic stall. *Journal of Aircraft*, 25(1):6–17.

Chamorro, L. P., Hill, C., Neary, V. S., Gunawan, B., Arndt, R. E., and Sotiropoulos, F. (2015). Effects of energetic coherent motions on the power and wake of an axial-flow turbine. *Physics of Fluids*, 27(5):055104.

Chen, L. and Lam, W.-H. (2015). A review of survivability and remedial actions of tidal current turbines. *Renewable and Sustainable Energy Reviews*, 43:891–900.

Corke, T. C. and Thomas, F. O. (2015). Dynamic stall in pitching airfoils: aerodynamic damping and compressibility effects. *Annual Review of Fluid Mechanics*, 47(1):479–505.

Coton, F. N., Wang, T., and Galbraith, R. A. M. (2002). An examination of key aerodynamic modelling issues raised by the NREL blind comparison. *Wind Energy*, 5(2-3):199–212.

Dalzell, J. (1999). A note on finite depth second-order wave–wave interactions. *Applied Ocean Research*, 21(3):105–111.

Dean, R. G. and Dalrymple, R. A. (1991). *Water Wave Mechanics for Engineers and Scientists*, volume 2 of *Advanced Series on Ocean Engineering*. World Scientific Publishing Co. Pte. Ltd.

Delorm, T. M., Zappala, D., and Tavner, P. J. (2012). Tidal stream device reliability comparison models. *Proceedings of the Institution of Mechanical Engineers, Part O: Journal of Risk and Reliability*, 226(1):6–17.

Diederich, W., Franklin, B., and Field, L. (1957). Effect of spanwise variations in gust intensity on the lift due to atmospheric turbulence. Technical report, NACA., Langley.

DNV-GL (2015). SE-0163 Certification of tidal turbines and arrays. Technical report.

Draper, S., Houlsby, G., Oldfield, M., and Borthwick, A. (2010). Modelling tidal energy extraction in a depth-averaged coastal domain. *IET Renewable Power Generation*, 4(6):545.

Draycott, S., Sellar, B., Davey, T., Noble, D., Venugopal, V., and Ingram, D. (2019). Capture and simulation of the ocean environment for offshore renewable energy. *Renewable and Sustainable Energy Reviews*, 104(December 2018):15–29.

Drayott, S., Steynor, J., Nambiar, A., Sellar, B., and Venugopal, V. (2019). Rotational Sampling of Waves by Tidal Turbine Blade. *Unpublished work*.

Drela, M. (1989). XFOIL: An Analysis and Design System for Low Reynolds Number Airfoils. pages 1–12.

Du, Z. and Selig, M. (2000). The effect of rotation on the boundary layer of a wind turbine blade. *Renewable Energy*, 20(2):167–181.

Eggers, A. J. and Digumathi, R. (1992). Approximate scaling of rotational effects on mean aerodynamic moments and power generated by CER blades operating in deep-stalled flow. In *11th ASME Wind Energy Symposium*, pages 33–44.

Energy Technologies Institute (2015). ReDAPT MC7.3 public domain report. Technical report.

Ericsson, L. and Reding, J. (1988). Fluid mechanics of dynamic stall part I. Unsteady flow concepts. *Journal of Fluids and Structures*, 2(1):1–33.

Evans, R., McAdam, R., Royle, M., and Mcewen, L. (2013). Optimum geometry for axial flow free stream tidal turbine blades. In *10th European Wave and Tidal Energy Conference (EWTEC 2013), Aalborg, DK, 02. - 05. Sep 2013*, number November.

Galbraith, R. A. M., Niven, A. J., and Coton, N. F. (1990). "Aspects of unsteady aerodynamics of wind turbines", Recent developments in the aerodynamics of wind turbines. In *BWEA workshop*, University of Nottingham.

Galloway, P. (2013). *Performance quantification of tidal turbines subjected to dynamic loading*. PhD thesis, University of Southampton.

Galloway, P. W., Myers, L. E., and Bahaj, A. S. (2014). Quantifying wave and yaw effects on a scale tidal stream turbine. *Renewable Energy*, 63:297–307.

Garcia, D. (2013). Simpson's rule for numerical integration.

Garrick, I. E. (1938). On some reciprocal relations in the theory of nonstationary flows. *NACA Technical Report 629*, pages 347–350.

Glauert, H. (1926). *A general theory of the autogyro*. HM Stationery Office, 1111 edition.

Graham, J. M. R. (2017). Rapid distortion of turbulence into an open turbine rotor. *Journal of Fluid Mechanics*, 825:764–794.

Gretton, G. I. (2010). Development of a computational fluid dynamics model for a horizontal axis tidal current turbine. Technical Report WG3 WP5 D1.

Guillou, N., Chapalain, G., and Neill, S. P. (2016). The influence of waves on the tidal kinetic energy resource at a tidal stream energy site. *Applied Energy*, 180:402–415.

Guntur, S., Sørensen, N. N., Schreck, S., and Bergami, L. (2016). Modeling dynamic stall on wind turbine blades under rotationally augmented flow fields. *Wind Energy*, 19(3):383–397.

Gupta, S. and Leishman, J. G. (2006). Dynamic stall modelling of the S809 aerofoil and comparison with experiments. *Wind Energy*, 9(6):521–547.

Hand, M. M., Simms, D. a., Fingersh, L. J., Jager, D. W., Cotrell, J. R., Schreck, S., and Larwood, S. M. (2001). Unsteady aerodynamics experiment phase VI: wind tunnel test configurations and available data campaigns. Technical Report December, National Renewable Energy Laboratory (NREL), Golden, CO.

Hansen, M., Sørensen, J., Voutsinas, S., Sørensen, N., and Madsen, H. (2006). State of the art in wind turbine aerodynamics and aeroelasticity. *Progress in Aerospace Sciences*, 42(4):285–330.

Hansen, M. H., Gaunaa, M., and Madsen, H. A. (2004). A Beddoes-Leishman type dynamic stall model in state-space and indicial formulations. Technical report.

Harris, F. D. (1966). Preliminary Study of Radial Flow Effects on Rotor Blades. *Journal of the American Helicopter Society*, 11(3):1–21.

Hashemi, M. R., Neill, S. P., Robins, P. E., Davies, A. G., and Lewis, M. J. (2015). Effect of waves on the tidal energy resource at a planned tidal stream array. *Renewable Energy*, 75:626–639.

Holierhoek, J., de Vaal, J., van Zuijlen, A., and Bijl, H. (2013). Comparing different dynamic stall models. *Wind Energy*, 16(1):139–158.

Holthuijsen, L. H. (2007). *Waves in Oceanic and Coastal Waters*. Cambridge University Press, Cambridge.

Ingram, D., Wallace, R., Robinson, A., and Bryden, I. (2014). The design and commissioning of the first, circular, combined current and wave test basin. In *Oceans 2014 MTS/IEEE*, Taipei. IEEE.

Janiszewska, J. M., Reuss Ramsay, R., Hoffmann, M. J., and Gregorek, G. M. (1996). Effects of grit roughness and pitch oscillations on the S814 airfoil. Technical report.

Jarrin, N., Benhamadouche, S., Laurence, D., and Prosser, R. (2006). A synthetic-eddy-method for generating inflow conditions for large-eddy simulations. *International Journal of Heat and Fluid Flow*, 27(4):585–593.

Johnson, P. B., Wojcik, A., Drake, K. R., and Eames, I. (2013). Impulsively started planar actuator surfaces in high-Reynolds-number steady flow. *Journal of Fluid Mechanics*, 733:302–324.

Jones, R. T. (1940). The unsteady lift of a wing of finite aspect ratio. *NACA Report 681*.

Jonkman, B. and Kilcher, L. (2012). TurbSim User's Guide: Version 1.06.00. Technical Report September, National Renewable Energy Laboratory.

Klimas, P. C. (1986). Three-dimensional stall effects. In *1-st IEA Symposium on the Aerodynamics of Wind Turbines*, pages 80–101, London.

Larsen, J. W., Nielsen, S. R. K., and Krenk, S. (2007). Dynamic stall model for wind turbine airfoils. *Journal of Fluids and Structures*, 23(7):959–982.

Leishman, J. G. (2002). Challenges in modeling the unsteady aerodynamics of wind turbines. *21st ASME Wind Energy Symposium and the 40th AIAA Aerospace Sciences Meeting*, pages 1–28.

Leishman, J. G. (2006). *Principles of Helicopter Aerodynamics*. Cambridge University Press.

Leishman, J. G. and Beddoes, T. S. (1986). A Generalised Model for Airfoil Unsteady Aerodynamic Behaviour and Dynamic Stall Using Indicial Method. In *42nd Annual Forum of the American Helicopter Society*, pages 243–266, Washington D.C.

Leishman, J. G. and Beddoes, T. S. (1989). A Semi-Empirical Model for Dynamic Stall. *Journal of the American Helicopter Society*, 34(3):3–17.

Lindenburg, C. (2004). Modelling of rotational augmentation based on engineering considerations and measurements. In *European Wind Energy Conference*, pages 22–25.

Loewy, R. G. (1957). A two-dimensional approximation to the unsteady aerodynamics of rotary wings. *Journal of the Aeronautical Sciences*, 24(2):81–92.

Maganga, F., Germain, G., and King, J. (2009). Experimental study to determine flow characteristic effects on marine current turbine behaviour. In *Ewtec 2009*, pages 661–667, Uppsala.

Maniaci, D. (2011). An Investigation of WT_Perf Convergence Issues. In *49th AIAA Aerospace Sciences Meeting including the New Horizons Forum and Aerospace Exposition*, Reston, Virigina. American Institute of Aeronautics and Astronautics.

Maniaci, D. C. and Li, Y. (2012). Investigating the Influence of the Added Mass Effect to Marine Hydrokinetic Horizontal-Axis Turbines Using a General Dynamic Wake Wind Turbine Code. *Marine Technology Society Journal*, 46(4):71–78.

Masters, I., Chapman, J. C., Willis, M. R., and Orme, J. A. C. (2011). A robust Blade Element Momentum Theory model for tidal stream turbines including tip and hub loss corrections. *Proceedings of the Institute of Marine Engineering, Science and Technology Part A: Journal of Marine Engineering and Technology*, 10(1):25–35.

McCann, G. N., Hitchcock, S., and Lane, S. (2008). Implications of site-specific conditions on the prediction of loading and power performance of a tidal stream device. In *2nd International Conference of Ocean Energy (ICOE 2008), 15 -17 October 2008, Brest, France*, number October, pages 1–9.

McCombes, T., Johnstone, C., and Grant, A. (2011). Unsteady wake modelling for tidal current turbines. *IET Renewable Power Generation*, 5(4):299.

McCroskey, W. (1995). Vortex wakes of rotorcraft. In *33rd Aerospace Sciences Meeting and Exhibit*, Reston, Virigina. American Institute of Aeronautics and Astronautics.

McCroskey, W. J. (1977). Some current research in unsteady fluid dynamics. The 1976 Freeman Scholar Lecture. *Journal of Fluids Engineering, Transactions of the ASME*, 99(1 , Mar. 1977):8–39.

McCroskey, W. J. (1981). The phenomenon of dynamic stall. No. NASA-A-8464. Technical report, NASA Ames Research Center, Moffett Field.

McNae, D. M. (2013). *Unsteady Hydrodynamics of Tidal Stream Turbines*. PhD thesis, Imperial College London.

McNaughton, J., Harper, S., Sinclair, R., and Sellar, B. (2015). Measuring and modelling the power curve of a commercial-scale tidal turbine. In *The 11th European Wave and Tidal Energy Conference*, pages 1–9.

Meygen LTD (2012). MeyGen Tidal Energy Project Phase 1 Environmental Statement. Technical report, MeyGen.

Milne, I. A. (2014). *An experimental investigation of turbulence and unsteady loading on tidal turbines*. PhD thesis, The University of Auckland.

Milne, I. A., Day, A. H., Sharma, R. N., and Flay, R. G. J. (2013a). Blade loads on tidal turbines in planar oscillatory flow. *Ocean Engineering*, 60:163–174.

Milne, I. A., Day, A. H., Sharma, R. N., and Flay, R. G. J. (2015). Blade loading on tidal turbines for uniform unsteady flow. *Renewable Energy*, 77:338–350.

Milne, I. A., Day, A. H., Sharma, R. N., and Flay, R. G. J. (2016). The characterisation of the hydrodynamic loads on tidal turbines due to turbulence. *Renewable and Sustainable Energy Reviews*, 56:851–864.

Milne, I. A. and Graham, J. M. R. (2019). Turbulence velocity spectra and intensities in the inflow of a turbine rotor. *Journal of Fluid Mechanics*, 870:R3.

Milne, I. A., Sharma, R. N., and Flay, R. G. J. (2017). The structure of turbulence in a rapid tidal flow. *Proceedings of the Royal Society A: Mathematical, Physical and Engineering Science*, 473(2204):20170295.

Milne, I. A., Sharma, R. N., Flay, R. G. J., and Bickerton, S. (2013b). Characteristics of the turbulence in the flow at a tidal stream power site. *Philosophical Transactions of the Royal Society A: Mathematical, Physical and Engineering Sciences*, 371(1985):20120196.

Moriarty, P. J. and Hansen, A. C. (2005). AeroDyn Theory Manual. Technical report.

Morison, J., Johnson, J., and Schaaf, S. (1950). The Force Exerted by Surface Waves on Piles. *Journal of Petroleum Technology*, 2(05):149–154.

Mullings, H. and Stallard, T. (2018). Unsteady loading in a tidal array due to simulated turbulent onset flow. In *Advances in Renewable Energies Offshore*, pages 227–235, Lisbon.

Neill, S. P., Vögler, A., Goward-Brown, A. J., Baston, S., Lewis, M. J., Gillibrand, P. A., Waldman, S., and Woolf, D. K. (2017). The wave and tidal resource of Scotland. *Renewable Energy*, 114:3–17.

Ning, A., Hayman, G., Damiani, R., and Jonkman, J. M. (2015). Development and validation of a new blade element momentum skewed-wake model within AeroDyn. In *33rd Wind Energy Symposium*, number December 2014, Reston, Virginia. American Institute of Aeronautics and Astronautics.

Ning, A. S. (2014). A simple solution method for the blade element momentum equations with guaranteed convergence. *Wind Energy*, 17:1327–1345.

Norris, J. V. and Droniou, E. (2007). Update on EMEC activities, resource description, and characterisation of wave-induced velocities in a tidal flow. In *Proceedings of the 7th European Wave and Tidal Energy Conference*, number December, Porto.

Ocean Energy Forum (2016). Ocean Energy Strategic Roadmap. Technical report.

Øye, S. (1991). Dynamic stall simulated as time lag of separation. Technical report, Department of Fluid Mechanics, Technical University of Denmark.

Payne, G. S., Stallard, T., and Martinez, R. (2017). Design and manufacture of a bed supported tidal turbine model for blade and shaft load measurement in turbulent flow and waves. *Renewable Energy*, 107:312–326.

Pierce, K. and Hansen, A. C. (1995). Prediction of wind turbine rotor loads using the Beddoes-Leishman model for dynamic stall. 117(August):200–204.

Pitt, D. M. and Peters, D. A. (1981). Theoretical prediction of dynamic-inflow derivatives. *Vertica*, 5(1):21–34.

Pope, S. B. (2001). *Turbulent flows*. IOP Publishing.

Reuss Ramsay, R., Hoffmann, M. J., and Gregorek, G. M. (1995). Effects of grit roughness and pitch oscillations on the S809 airfoil. Technical report.

Reuss Ramsay, R., Hoffmann, M. J., and Gregorek, G. M. (1996a). Effects of grit roughness and pitch oscillations on the S801 airfoil. Technical report.

Reuss Ramsay, R., Hoffmann, M. J., and Gregorek, G. M. (1996b). Effects of grit roughness and pitch oscillations on the S810 airfoil. Technical report.

Reuss Ramsay, R., Hoffmann, M. J., and Gregorek, G. M. (1996c). Effects of grit roughness and pitch oscillations on the S813 airfoil. Technical report.

Reuss Ramsay, R., Hoffmann, M. J., and Gregorek, G. M. (1996d). Effects of grit roughness and pitch oscillations on the S815 airfoil. Technical report.

Reuss Ramsay, R., Hoffmann, M. J., and Gregorek, G. M. (1998a). Effects of grit roughness and pitch oscillations on the S812 airfoil. Technical report.

Reuss Ramsay, R., Hoffmann, M. J., and Gregorek, G. M. (1998b). Effects of grit roughness and pitch oscillations on the S825 airfoil. Technical report.

Sanchex, A. (2013). Wave dispersion relation (wavenumber-m).

Saruwatari, A., Ingram, D. M., and Cradden, L. (2013). Wave–current interaction effects on marine energy converters. *Ocean Engineering*, 73:106–118.

Scarlett, G. T. and Viola, I. M. (2017). Tidal turbine hydrodynamic model.

Sellar, B., Wakelam, G., Sutherland, D. R. J., Ingram, D. M., and Venugopal, V. (2018). Characterisation of tidal flows at the European marine energy centre in the absence of ocean waves. *Energies*, 11(1):176.

Sequeira, C. L. and Miller, R. J. (2015). Unsteady gust response of tidal stream turbines. In *2014 Oceans - St. John's. IEEE*, pages 1–10, St. Johns.

Sheng, W., Galbraith, R. A. M., and Coton, F. N. (2008). A modified dynamic stall model for low Mach numbers. *Journal of Solar Energy Engineering*, 130(3):031013.

Sheng, W., Galbraith, R. A. M., and Coton, F. N. (2010). Applications of low-speed dynamic-stall model to the NREL airfoils. *Journal of Solar Energy Engineering*, 132(1):011006.

Sheng, W., McD. Galbraith, R. A., and Coton, F. N. (2007). Return from Aerofoil Stall During Ramp-Down Pitching Motions. *Journal of Aircraft*, 44(6):1856–1864.

Shinozuka, M. (1972). Monte Carlo solution of structural dynamics. *Computers and Structures*, 2(5-6):855–874.

Simms, D., Schreck, S., Hand, M., and Fingersh, L. J. (2001). NREL Unsteady Aerodynamics Experiment in the NASA-Ames Wind Tunnel: A Comparison of Predictions to Measurements. Technical Report June, National Renewable Energy Laboratory (NREL), Golden, CO (United States).

Soulsby, R. (1983). Chapter 5 The Bottom Boundary Layer of Shelf Seas. In *Physical Oceanography of Coastal and Shelf Seas*, volume 35, pages 189–266.

Stokes, G. (1847). On the Theory of Oscillatory Waves. *Transactions of the Cambridge Philosophical Society*, 8:441–455.

Tangler, J. L. (2002). The nebulous art of using wind tunnel aerofoil data for predicting rotor performance. *Wind Energy*, 5(2-3):245–257.

Tangler, J. L. and Somers, D. M. (1995). NREL airfoil families for HAWTs. Technical Report January.

Tarzanin, F. J. (1972). Prediction of Control Loads Due to Blade Stall. *Journal of the American Helicopter Society*, 17(2):33–46.

Theodorsen, T. (1935). General theory of aerodynamic instability and the mechanism of flutter. *NACA Technical Report 496*, pages 413 – 433.

Thomson, J., Polagye, B., Durgesh, V., and Richmond, M. C. (2012). Measurements of turbulence at two tidal energy sites in Puget Sound, WA. *IEEE Journal of Oceanic Engineering*, 37(3):363–374.

Thwaites, B. (1960). *Incompressible Aerodynamics: An account of the theory and observations of the steady flow of incompressible fluid past aerofoils, wings and other bodies*. University Oxford Press.

Togneri, M., Edmunds, M., Masters, I. A. N., Ement, C. L., Bex, C. C., and Pinon, G. R. E. (2018). Comparisons of synthetic turbulence models used in a BEMT tidal turbine model. In *7th European Conference on Computational Fluid Dynamics (ECFD 7)*, number June, Glasgow.

Tran, C. and Petot, D. (1981). Semi-empirical model for the dynamic stall of airfoils in view of the application to the calculation of responses of a helicopter blade in forward flight. *Vertica*, 5(1):35–53.

Tully, S. and Viola, I. M. (2016). Reducing the wave induced loading of tidal turbine blades through the use of a flexible blade. *International Symposium on Transport Phenomena and Dynamics of Rotating Machinery (ISROMAC 2016)*, page 9.

UKERC (2018). Energy Data Centre.

VEERS, P. (1984). Modeling stochastic wind loads on vertical axis wind turbines. In *25th Structures, Structural Dynamics and Materials Conference*, volume 1524, pages 1–17, Reston, Virigina. American Institute of Aeronautics and Astronautics.

Veers, P. S. (1988). Three-dimensional wind simulation. SAND88-0152. Technical report, Sandia National Laboratories, Albuquerque.

Visbal, M. (2011). Three-dimensional flow structure on a heaving low-aspect-ratio wing. In *49th AIAA Aerospace Sciences Meeting including the New Horizons Forum and Aerospace Exposition*, Reston, Virigina.

Viterna, L. and Corrigan, R. (1981). Fixed pitch rotor performance of large horizontal axis wind turbines. Technical report, NASA Lewis Research Center.

Von Karman, T. and Biot, M. (1940). *Mathematical methods in engineering*. London: New York.

Wagner, H. (1925). Über die entstehung des dynamischen auftriebes von tragflügeln. *Journal of Applied Mathematics and Mechanics/Zeitschrift für Angewandte Mathematik und Mechanik*, 5(1):17–35.

Whelan, J., Graham, J., and Pierø, J. (2009). Inertia Effects on Horizontal Axis Tidal-Stream Turbines. *Proceedings of the 8th European Wave and Tidal Energy Conference, Uppsala, Sweden*, pages 586–591.

Whitby, B. and Ugalde-Loo, C. E. (2014). Performance of Pitch and Stall Regulated Tidal Stream Turbines. *IEEE Transactions on Sustainable Energy*, 5(1):64–72.

Wilcox, B. J. and White, E. B. (2017). Roughness sensitivity comparisons of wind turbine blade sections. Technical Report SAND2017-11288, Sandia National Laboratories, Albuquerque.

Young, A. M., Farman, J. R., and Miller, R. J. (2016). Load alleviation technology for extending life in tidal turbines. In *Progress in Renewable Energies Offshore-Proceedings of 2nd International Conference on Renewable Energies Offshore, RENEW 2016*, pages 521–530.